## UNIVERSIDAD POLITÉCNICA DE MADRID

# ESCUELA TÉCNICA SUPERIOR DE INGENIEROS AERONÁUTICOS

### DEPARTAMENTO DE AERONAVES Y VEHÍCULOS AEROESPACIALES



**DOCTORAL THESIS** 

# PANEL METHOD FOR THE AERODYNAMIC CALCULATION OF MIXED CONFIGURATIONS WITH FINITE THICKNESS AND ZERO THICKNESS

Author:
Jose Miguel EZQUERRO NAVARRO
Ingeniero Aeronáutico

Supervised by: Dra. Ma Victoria Lapuerta González Dra. Ana Laverón Simavilla



Tribunal nombrado por el Sr. Rector Magfco. de la Universidad Madrid, el díadede 20	Politécnica de
Presidente:	-
Vocal:	-
Vocal:	-
Vocal:	-
Secretario:	-
Suplente:	-
Suplente:	-
Realizado el acto de defensa y lectura de la Tesis el díadeen la E.T.S.I. /Facultad	de 20
Calificación	
EL PRESIDENTE LOS VO	OCALES

EL SECRETARIO

A mis padres,

# PANEL METHOD FOR THE AERODYNAMIC CALCULATION OF MIXED CONFIGURATIONS WITH FINITE THICKNESS AND ZERO THICKNESS

### *Abstract*

by Jose Miguel EZQUERRO NAVARRO

Panel Methods are well-known methods for solving potential fluid flow problems, mainly for preliminary design phases. These methods, also known as boundary element methods (BEM), have been applied to solve the Laplace equation for aerodynamics calculations since the 60's. However, mixed configurations of obstacles with finite thickness and zero thickness have not been solved with these methods. Such configurations arise naturally in delta wings, sailing boats, and even in complete aircraft aerodynamics. In this work, a new numerical approach is proposed for solving two-dimensional (2D) mixed configurations of obstacles with finite thickness and zero thickness components. The method is based on the Dirichlet and Neumann formulations and is checked by comparison with analytical results.

On the other hand, despite the widespread use of panel methods and although many works found in the literature study the error associated to their use, generally, there is a lack of consensus concerning the order of magnitude of the error for panel methods. This applies even in the simplest case, which consists of flat panels and a constant distribution of doublets along them. Most of these previous studies focused on the analysis of local error, considering only the influence of the nearest panels and excluding the rest. The difference is shown to be appreciable in many configurations when considering every single panel. A rigorous analytical study of the global error of panel methods when applying Dirichlet and Neumann boundary conditions is presented in this work. The analysis is performed for a wide variety of body shapes and different panel geometries to fully understand their effect on the convergence of the method. In particular, we study the global error associated with panel methods applied to thin or thick bodies with purely convex parts or with both convex and concave parts, and with smooth or non-smooth boundaries. This work clarifies apparently different or inconsistent results obtained by other authors.

# MÉTODO DE PANELES PARA EL CÁLCULO AERODINÁMICO DE CONFIGURACIONES MIXTAS DE OBSTÁCULOS CON Y SIN ESPESOR

### Resumen

por Jose Miguel EZQUERRO NAVARRO

Los métodos de paneles son métodos bien conocidos para resolver problemas de movimientos potenciales de fluidos, principalmente durante las fases preliminares de diseño. Estos métodos, también conocidos como métodos de condiciones de contorno (boundary element methods), se han usado para resolver la ecuación de Laplace en cálculos aerodinámicos desde los años 60. Sin embargo, con estos métodos no se han resuelto configuraciones mixtas de obstáculos con espesor y sin espesor. Tales configuraciones surgen naturalmente en las alas delta, en los barcos de vela, e incluso en la geometría completa de las aeronaves. En este trabajo se propone un nuevo enfoque numérico para resolver configuraciones mixtas en dos dimensiones (2D) de obstáculos con espesor y sin espesor. El método se basa en las formulaciones de Dirichlet y Neumann y se verifica mediante comparación con soluciones analíticas.

Por otra parte, a pesar del uso generalizado de los métodos de paneles y aunque se pueden encontrar muchos trabajos en la literatura que estudian el error asociado a su uso, en general, hay una falta de consenso sobre el orden de magnitud del error que se comete al emplear los métodos de paneles. Esto último aplica incluso al caso más sencillo, que consiste en el uso de paneles planos y de una distribución constante de dobletes a lo largo de ellos. La mayoría de estos estudios se centraron en el análisis local del error, considerando sólo la influencia de los paneles más cercanos y excluyendo el resto. En muchas configuraciones se puede apreciar una diferencia sustancial al considerar todos y cada uno de los paneles. En este trabajo se presenta un estudio analítico y riguroso del error global de los métodos de paneles cuando se usan las condiciones de contorno de Dirichlet y de Neumann. El análisis se realiza para una amplia variedad de cuerpos y geometrías de paneles para comprender en profundidad su efecto sobre la convergencia del método. En particular, se estudia el error global asociado a los métodos de paneles aplicados a cuerpos delgados o gruesos con partes puramente convexas o con partes convexas y cóncavas y con bordes suaves o no. Este trabajo trata de aclarar resultados aparentemente diferentes o inconsistentes obtenidos por otros autores.

# Acknowledgements

First of all, I want to thank my thesis director Ana Laverón Simavilla for the opportunity of doing my Ph.D in this subject and for all the advise and support I got from her, not only for this thesis development but also for my professional skills evolution. In the same line, I want to thank my thesis director Victoria Lapuerta González for all the effort invested in remembering what those panels where about, that I know was hard sometimes but nice some others. Everything started for me with some optional lessons at the university about numerical aerodynamics that Ana and Vicky used to teach and that I loved to teach, although the work on this panel method subject started a lot of time before me.

Jose Javier Fernández is one of the main drivers of my decision to do this Ph.D thesis. We have walked this road together from the begging till this end, but hopefully this will be just a new road start.

I am grateful to the people I work with in the Spanish User Support and Operations Centre (E-USOC) and in particular to Jacobo Rodriguez, who taught me a lot of things i.e. how to write and rewrite documents.

I want to thank Miguel Angel Gonzalez for getting me involved in very interesting projects that helped me to keep pushing in order to finish my degree studies.

Some words of thank must go to my family. My parents have been always there, pushing me to study harder, to jump higher, to finish the degree, to fill the tupperware at home when the day work lasts until night, to complete this work... Marta holds me when I have been tired or disgusted without expecting anything back and giving me a smile or making me laugh. My brother has tried to maintain my fitness status, with relative success. I don't remember every single detail because I was a child, but my grandfather showed me the love for the airplanes, the airports, the aerodynamics, the space... and I still and will remember forever some of his flights histories. I think he would be very proud of what I have become.

# **Contents**

A	bstrac	ct		vii
Re	esum	en		ix
A	cknov	wledgei	nents	хi
1	Intr	oductio	o <b>n</b>	1
	1.1	Histor	ical background	1
	1.2	Thesis	objectives	4
	1.3	Thesis	structure overview	4
2	Rev	iew of	the Panel Methods	7
	2.1	Brief c	lescription of the panel method	7
	2.2	Review	w of Dirichlet and Neumann Formulations	12
		2.2.1	Dirichlet Formulation for Finite-Thickness Bodies	12
		2.2.2	Neumann Formulation for Zero-Thickness Bodies	14
3	Pan	el Meth	od for Mixed Configurations with Finite Thickness and Zero Thick	-
	ness	3		19
	3.1	Mixed	Dirichlet-Neumann Formulation for Zero-Thickness Bodies	19
	3.2	Formu	alation for Mixed Finite-Thickness and Zero-Thickness Bodies	22
	3.3	Analy	tical solution	26
	3.4	Nume	rical Results and Discussion	29
		3.4.1	Circle with a Flat Plate	30
		3.4.2	Slender Body with a Tilted Flat Plate	34
		3.4.3	Karman-Trefftz Body with a Cosine-shaped Camber Line	39
		3.4.4	Thin Symmetric Body with a Flat Plate	42
		3.4.5	Cusped Trailing Edge Thick Body with a Tilted Flat Plate	44
	3.5	Discus	ssions	49
4	Glo	bal Erro	or Analysis of Two-Dimensional Panel Methods for Dirichlet Formu	-
	latio	on		51
	4.1	Globa	l error estimate for Dirichlet formulation	52
	4.2	Detail	s of error estimate	59
		421	Details of error estimate for sharp trailing edge	65

	4.3	Result	ts and Discussions	66
		4.3.1	Numerical error results for thick bodies without sharp corners	67
		4.3.2	Numerical error results for thin bodies without sharp corners	71
		4.3.3	Numerical error results for bodies with sharp corners	75
			4.3.3.1 Symmetric bodies with sharp corners	76
			4.3.3.2 Asymmetric bodies with sharp corners	79
		4.3.4	Numerical error results for curved panels	84
	4.4	Discus	ssions	85
5	Glo	bal Err	or Analysis of Two-Dimensional Panel Methods for Neumann Fo	r-
	mul	ation		87
	5.1	Globa	l error estimate for Neumann formulation	88
	5.2	Detail	s of the Neumann error estimate	95
	5.3	Result	ts and Discussions	100
		5.3.1	Numerical error results for thick bodies without sharp corners	102
		5.3.2	Numerical error results for thin bodies without sharp corners	105
		5.3.3	Numerical error results for bodies with sharp corners	106
			5.3.3.1 Symmetric bodies with sharp corners	106
			5.3.3.2 Asymmetric bodies with sharp corners	112
	5.4	Discus	ssions	116
6	Con	clusior	ns and Future Works	119
	6.1	Future	e Works	121
A	Diri	chlet n	nethod integrals definition	123
В	Neu	ımann	method polar angle derivative definition	125
C	Loca	al geon	netric considerations for panels	127
Bi	bliog	raphy		129

# **List of Figures**

2.1	Fluid domain in Green's integral equation. Sketch of the body and associ-	
	ated surfaces: body surface $S_B$ , wake surface $S_W$ , point ${m p}$ surface $S_\epsilon$ and a	
	surface at infinity $S_{\infty}$ . $V_{\infty}$ and angle of attack representation	9
2.2	Discretization of geometry for a finite-thickness obstacle	11
2.3	Body surface and panel j representation. Definition of limiting nodes $oldsymbol{x}_I^j$	
	and $x_F^j$ , collocation points $x_{cp}^j$ and normal vector to panel $n_j$	12
2.4	Definition of $\theta_{kF}^j$ , $\theta_{kI}^j$ and $\theta_k^{\infty}$	13
2.5	Representation of panel $j$ with its associated normal vector $n$ pointing to	
	the outer fluid flow. Point $o$ is placed inside the outer flow and point $i$ is	
	placed in the inner flow (inside the body for thick airfoils)	14
2.6	Discretization of geometry for a zero thickness obstacle	15
3.1	Mixed configuration (thick and non-thick) panel discretization	23
3.2	Complete conformal map transformation	27
3.3	Circle with a flat plate body representation. The parameters of the config-	
	uration are: $l/R = 7$ , $k = 1$ , $\lambda = 0$ , $\delta = 0$	30
3.4	Comparison of the pressure coefficient obtained with the analytical solu-	
	tion of Section 3.3, the mixed Dirichlet-Neumann numerical approach pro-	
	posed in Section 3.2 (D-N) and the discrete vortex method for different	
	panel numbers for different panel numbers. The parameters of the config-	
	uration are: $\alpha=12^{\circ}$ , $l/R=7$ , $k=1$ , $\lambda=0$ , $\delta=0$ . The body is represented	
	again in these figures to ease the pressure coefficient evolution visualization.	32
3.5	Error in the pressure coefficient calculated with the mixed Dirichlet-Neumann	
	numerical approach proposed in Section 3.2 (D-N) and the discrete vortex	
	method for different number of panels. The parameters of the configura-	
	tion are: $\alpha=12^{\circ}$ , $l/R=7$ , $k=1$ , $\lambda=0$ , $\delta=0$	33
3.6	Slender body with a tilted flat plate body representation. The parameters	
	of the configuration are: $l/R=3$ , $k=1.8$ , $\lambda=0.05$ , $\delta=0.3$	34

3.7	Pressure coefficient obtained with the analytical solution of Section 3.3, the	
	mixed Dirichlet-Neumann numerical approach proposed in Section 3.2 (D-	
	N) and the discrete vortex method for different panel numbers. The data	
	of the configuration are: $\alpha - \beta = 2^{\circ}$ , $l/R = 3$ , $k = 1.8$ , $\lambda = 0.05$ , $\delta = 0.3$ . The	
	body is represented again in these figures to ease the pressure coefficient	
	evolution visualization	36
3.8	Error in the pressure coefficient calculated with the mixed Dirichlet-Neumann	
	numerical approach proposed in Section 3.2 (D-N) and the discrete vortex	
	method for different panel numbers. The data of the configuration are:	
	$\alpha - \beta = 2^{\circ}$ , $l/R = 3$ , $k = 1.8$ , $\lambda = 0.05$ , $\delta = 0.3$	39
3.9	Karman-Trefftz body with a cosine-shaped camber line body representa-	
	tion. The data of the configuration are: $k = 1.8$ , $\lambda = 0.19$ , $\delta = 0.2$	40
3.10	Comparison of the pressure coefficient obtained with the mixed Dirichlet-	
	Neumann numerical approach proposed in Section 3.2 (D-N) and the dis-	
	crete vortex method for for different panel numbers. The data of the con-	
	figuration are: $\alpha - \beta = 2^{\circ}$ , $k = 1.8$ , $\lambda = 0.19$ , $\delta = 0.2$ . The body is rep-	
	resented again in these figures to ease the pressure coefficient evolution	
	visualization.	42
3.11	Thin symmetric body with a flat plate representation. The data of the con-	
	figuration are: $l/R = 5$ , $k = 1.95$ , $\lambda = 0.04$ , $\delta = 0$	42
3.12	Comparison of the pressure coefficient obtained with the analytical solu-	
	tion of Section 3.3, the mixed Dirichlet-Neumann numerical approach pro-	
	posed in Section 3.2 (D-N) and the discrete vortex method for different	
	panel numbers for $N=61, M=34$ . The parameters of the configuration	
	are: $\alpha = 5^{\circ}$ , $l/R = 5$ , $k = 1.95$ , $\lambda = 0.04$ , $\delta = 0$ . The body is represented	
	again in this figure to ease the pressure coefficient evolution visualization.	43
3.13	Error in the pressure coefficient calculated with the mixed Dirichlet-Neumann	
	numerical approach proposed in Section 3.2 (D-N) and the discrete vortex	
	method for $N=61, M=34$ . The parameters of the configuration are:	
	$\alpha = 5^{\circ}, l/R = 5, k = 1.95, \lambda = 0.04, \delta = 0. \dots \dots \dots \dots \dots$	44
3.14	Cusped trailing edge thick body with a tilted flat plate representation. The	
	data of the configuration are: $l/R=3$ , $k=2$ , $\lambda=0.2$ , $\delta=0.3$	44
3.15	Pressure coefficient calculated with the analytical solution of Section 3.3,	
	the mixed Dirichlet-Neumann numerical approach proposed in Section 3.2	
	(D-N) and the discrete vortex method for different panel numbers. The	
	data of the configuration are: $\alpha - \beta = 2^{\circ}$ , $l/R = 3$ , $k = 2$ , $\lambda = 0.2$ , $\delta =$	
	0.3. The body is represented again in these figures to ease the pressure	
	coefficient evolution visualization	47
3.16	Error in the pressure coefficient obtained with the mixed Dirichlet-Neumann	
	numerical approach proposed in Section 3.2 (D-N) and the discrete vortex	
	method for different panel numbers. The data of the configuration are:	
	$\alpha - \beta \equiv 2^{\circ}$ , $1/R \equiv 3$ , $k \equiv 2$ , $\lambda \equiv 0.2$ , $\delta \equiv 0.3$ ,	49

4.1	Discretization of the body surface	53
4.2	Relationship between $p_i$ , $x_i$ , and $s_i$ in the concave (panel $i$ ) and convex	
	(panel <i>j</i> ) cases	54
4.3	Definition of $\theta_{p_i s_j}$ and $\delta_{ij}$	57
4.4	Definitions used in evaluating the integral in Eq. (4.26) in the convex case.	
	For simplicity, we drop the subscripts on the angles here	61
4.5	Definitions used in evaluating the integral in Eq. (4.26) in the concave case.	64
4.6	Sketch of trailing edge in a sharp body	65
4.7	Ellipse with axis length 5 and 3	68
4.8	Comparison of the numerical error using the Dirichlet formulation for a	
	thick ellipse with the collocation points placed at the center of the panels	
	(lower curve) and at the position $l_i/3$ (upper curve) for $\alpha=2^{\circ}$	69
4.9	Nonsymmetric body with concave and convex parts	70
4.10	Numerical error using the Dirichlet formulation for a nonsymmetric body	
	with concave and convex parts for $\alpha = 2^{\circ}$	71
4.11	Thin ellipse	72
4.12	Detail of the panels near the trailing edge of a thin ellipse with $h \ll l \ \ . \ \ .$	73
4.13	Numerical error using the Dirichlet formulation for a thin ellipse for $\alpha=2^{\rm o}$ .	74
4.14	Symmetric bodies with a sharp corner obtained from a Karman-Trefft trans-	
	formation with $k_T = 1.1, 1.3$ and 1.6	76
4.15	Numerical error using the Dirichlet formulation for symmetric bodies with	
	sharp corners for $\alpha=2^{\rm o}$	77
4.16	Numerical error using the Dirichlet formulation for symmetric bodies with	
	sharp corners for $\alpha = 0^{\circ}$	78
4.17	Numerical error using the Dirichlet formulation for symmetric bodies with	
	sharp corners for $\alpha=10^{\rm o}$	79
4.18	Asymmetric bodies with sharp corners obtained from a Karman-Trefft trans-	
	formation with $k_T = 1.3, 1.5$ and 1.8	80
4.19	Numerical error using the Dirichlet formulation for asymmetric bodies	
	with sharp corners for $\alpha=0^{\rm o}.$	81
4.20	Numerical error using the Dirichlet formulation for asymmetric bodies	
	with sharp corners for $\alpha = 2^{\circ}$	81
4.21	Numerical error using the Dirichlet formulation for asymmetric bodies	
	with sharp corners for $\alpha=10^{\rm o}$	82
4.22	Evolution of $p$ with the angle of the trailing edge $\gamma$ (in degrees) for different	
	α	83
4.23	Evolution of $p$ with $k_T$ for different $\alpha$	83
4.24	Comparison of numerical error for flat panels and curved panels. The re-	
	sults are so close that it is hard to distinguish them on the scale of the plot.	85
5.1	Definition of $\theta^I_{x_ix_j}$ and $\theta^F_{x_ix_j}$	88
5.2		00 101
J • Z	$i_{1}$	-01

5.3	Comparison of the numerical error using the Neumann formulation for a	
	thick ellipse with the collocation points placed at the center of the panels	102
E 1	(lower curve) and at the position $l_i/3$ (upper curve) for $\alpha = 2^{\circ}$	103
5.4	Numerical error using the Neumann formulation for a nonsymmetric body	104
	with concave and convex parts for $\alpha = 2^{\circ}$	104
5.5	Thin ellipse obtained from a Youkovsky transformation with $a=1.7.$	105
5.6	Numerical error using the Neumann formulation for a thin ellipse in two	100
	points, one of them very close to the trailing edge for $\alpha=2^{\rm o}$	106
5.7	Numerical error using the Neumann formulation for symmetric bodies	
	with sharp corners for $\alpha = 2^{\circ}$	107
5.8	Numerical error using the Neumann formulation for symmetric body with	
	sharp corners for $\alpha=2^{\circ}$ and a high number of panels	108
5.9	Numerical error using the Neumann formulation for symmetric bodies	
	with sharp corners for $\alpha = 0^{\circ}$	109
5.10	Numerical error using the Neumann formulation for symmetric bodies	
	with sharp corners for $\alpha = 10^{\circ}$	110
5.11	Symmetric body with a sharp corner obtained from a Karman-Trefft trans-	
	formation with $k_T = 1.9$	111
5.12	Numerical error using the Neumann formulation for symmetric bodies	
	with very sharp corners for $\alpha=2^{\rm o}$	111
5.13	Asymmetric bodies with sharp corners obtained from a Karman-Trefft trans-	
	formation with $k_T = 1.3, 1.5$ and 1.9	112
5.14	Numerical error using the Neumann formulation for asymmetric bodies	
	with sharp corners for $\alpha=2^{\rm o}$	113
5.15	Numerical error using the Neumann formulation for asymmetric bodies	
	with sharp corners for $\alpha = 0^{\circ}$	114
5.16	Numerical error using the Neumann formulation for asymmetric bodies	
	with sharp corners for $\alpha = 10^{\circ}$	115
5.17	Numerical error using the Neumann formulation for an asymmetric bod-	
	ies with a very sharp corner ( $k_T = 1.9$ ) and with a high angle of attack	
	$\alpha = 30^{\circ}$	116
A.1	Discretization of geometry for the Laplace's equation integrals simplification	.124
B.1	Polar angle of the difference vector for two points $x$ and $y$	125
C.1	Definition of local coordinate system	127
C.2	Illustration of intermediate value theorem	128
C.3	Angle $\delta_{ii}$ subtended at $p_i$ by panel $i$ itself, in the convex case	128

# Chapter 1

# Introduction

Methods for solving potential fluid flows are frequently used in engineering practices, mainly for preliminary design. Although non-potential models, like CFDs (Computational Fluid Dynamics) are widespread, they require long calculation times and the results are not always reliable so inputs from potential methods are often needed.

The potential method is valid only if the viscous effects are negligible or if they are reduced to small areas of the fluid field. In case of incompressible flows the velocity potential must satisfy the Laplace's equation. In case of linearised compressible subsonic flows, the velocity potential must satisfy the Prandtl-Glauert equation. In this last case and applying an easy transformation, the Prandtl-Glauert equation can be converted in the Laplace's equation, so that solving this last equation is enough to solve both kind of movements. The panel methods allow one to calculate numerically the solution of any given problem as long as the velocity potential satisfies the Laplace's equation.

### 1.1 Historical background

The importance of the Laplace's equation in the aerodynamics (and many other scientific fields) had made the researchers to dedicate a great effort in developing analytical and numerical methods to solve this equation. One of the most

developed potential methods is the panel method or boundary element method (BEM) (Brebbia and Dominguez, 1977; Brebbia, Telles, and Wrobel, 1984), which reduce the problem of finding the velocity potential for the entire fluid to the calculation of this potential on the surface of the body itself. Thus, the dimension of the problem is reduced from three to two (or, in the case of two-dimensional flows, from two to one) making BEMs very attractive for their low computational cost compared with non-potential methods. Since the pioneering work of Hess and Smith there have been numerous publications and many numerical codes based on panel methods (Hess and Smith, 1962; Morino and Kuo, 1974; Rubbert and Saaris, 1968; Hess, 1972; Morino, Chen, and Suciu, 1975; Ehlers and Rubbert, 1979; Hess, 1990; Erickson, 1990; Hwang, 2000; Katz and Plotkin, 2001; Ye and Fei, 2009; Yu, Wang, and Hong, 2004); among these we emphasize the reviews of Hess (Hess, 1990), Erickson (Erickson, 1990) and the book of Katz and Plotkin (Katz and Plotkin, 2001). Boundary element methods are an active field of study, especially within the engineering community, with new applications being developed rapidly.

Initially, panel methods were developed using flat panels and a constant (Hess and Smith, 1962; Rubbert and Saaris, 1968) or linear (Hess, 1972) distribution of singularities on each panel. Beginning in the 1970's however, singularity distributions were modeled (on each panel) using quadratic (Morino and Kuo, 1974; Johnson and Rubbert, 1975; Ehlers et al., 1979) or cubic (Mercer, Weber, and Ledferd, 1974) functions. In a similar fashion, the panels themselves, which were initially taken to be flat, were generalized to include non-planar geometries (Morino and Kuo, 1974; Johnson and Rubbert, 1975). However, in the last several decades many numerical codes returned to the original low-order approach, as indicated in (Katz and Plotkin, 2001). The main reason for this is the more complicated implementation of higher-order methods compared to lower-order ones (Hwang, 2000).

The panel method based on Green's formula was first introduced in the work of Morino and Kuo (Morino and Kuo, 1974), in which the primary unknown was

the velocity potential. There are two main formulations both based on Green's formula: Neumann and Dirichlet (Katz and Plotkin, 2001). The Dirichlet formulation solves the Laplace's equation numerically and provides the velocity potential. However, with the Neumann formulation, only differences of potential are obtained. The Dirichlet formulation is more stable and more suitable to numerical computation than the Neumann formulation and leads to numerical errors of a smaller order of magnitude.

However, these formulations cannot be directly applied to mixed configurations of both finite and zero thickness, such as the mast and the sail of a sailing boat, traffic signs (Sanz-Andrés et al., 2004), delta wings or configurations like Gurney flaps (Morishita, 2004). In the work by Wilkinson (Wilkinson, 1988) a distribution of vortices is used to model the surface of a mast and sail and sources and sinks are used to represent the flow separation, which is just an empirical fit to data from wind tunnel and is not related to the subject of this paper. Nevertheless, in this work we show that methods based on discrete vortex do not recover correctly the flow around mixed two-dimensional configurations.

It is common sense to question about the error or the magnitude of the error that one assumes when using these type of methods for the resolution of a problem given, so a lot of studies can be found in the literature that address the question of the error associated to the panel methods. Some authors carry out a numerical analysis of the error by comparing a numerical solution with a known analytical solution (Oskam, 1986; Bellamy-Knights et al., 1989; Kinnas and Hsin, 1994). Others perform a local analysis of the error by using small curvature expansions to obtain local approximations to the velocity and potential integrals (Hess, 1973; Hess, 1975; Romate, 1988; Vaz, Eça, and Campos, 2003). However, in spite of the great expansion of the panel methods in several scientific fields, a rigorous analytical study of the global error of these methods that applies to thin or thick bodies, with purely convex parts or with both convex and concave parts, and with smooth or non-smooth boundaries, has not yet been performed. Depending on the airfoil geometry, the panel geometry and the discretization,

apparently different or inconsistent results are obtained by other authors, and differences between theoretical and numerical results exist as well (Oskam, 1986; Bellamy-Knights et al., 1989; Kinnas and Hsin, 1994; Vaz, Eça, and Campos, 2003; Falcão de Campos, Ferreira de Sousa, and Bosschers, 2006).

### 1.2 Thesis objectives

This thesis has two main objectives. The first objective is to develop a numerical method for mixed two-dimensional (2D) configurations of finite and zero-thickness bodies. This method does not introduce spurious singularities in the numerical resolution and gives very good precision results, even for very thin airfoils or airfoils with cusped trailing edge.

The second objective of this thesis is to study the error associated with the resolution of the fluid flow using either Dirichlet or Neumann boundary conditions applied to the Laplace's equation. A formal analytical and numerical analysis of the asymptotic global error in panel methods for a wide variety of body shapes is presented, to try to understand the effect of the body and panel geometry on the convergence of the methods. This allows us to clarify several important questions about the convergence rate for the velocity potential since, even for the simplest case of flat panels with a constant distribution of doublets along them, there is a lack of general consensus. In addition, an analysis of the influence of the panel geometry on the global error is performed.

### 1.3 Thesis structure overview

This section provides an overview of the thesis structure, giving a brief description of the content of each chapter.

Chapter 1 provides an introduction to the panel methods and their historical background over the several decades of their developments. Then the thesis objectives are introduced.

Chapter 2 presents a brief description of the panel method as the start point for a more detailed Dirichlet and Neumann formulations revision.

Chapter 3 focuses on a new numerical method for mixed two-dimensional (2D) configurations of finite thickness and zero-thickness bodies. This formulation is also applicable to bodies without thickness, providing more precise results than the discrete vortex solution. Afterwards an analytical solution is calculated in order to check the results and the precision of the numerical method. The analysis of the results for different bodies shapes and the main conclusions are discussed in detail to end this chapter.

Chapter 4 is dedicated to the global error analysis of two-dimensional (2D) panel methods for the resolution of the fluid flow using the Dirichlet formulation. First, the problem is formulated in a proper manner, so that the error analysis can be performed analytically. The details of the error estimation are presented and some special geometries are discussed. After that, numerical and analytical solutions for different body geometries are reviewed in order to compare the actual and predicted errors in each case. Some particular conclusions are given as a result of the outcomes of the work.

Chapter 5 is dedicated to the global error analysis of two-dimensional (2D) panel methods for the resolution of the fluid flow using the Neumann formulation. First, the problem is formulated in a proper manner, so that the error analysis can be performed analytically. The details of the error estimation are presented, and afterwards, numerical and analytical experiments for different body geometries are reviewed in order to compare the actual and predicted errors in each case. Some particular conclusions are given as a result of the outcomes of the work.

Chapter 6 focus on the final conclusions of the thesis and gives suggestions for future developments.

# **Chapter 2**

# **Review of the Panel Methods**

This chapter provides a short introduction to panel method to serve as a start point for the next chapters. Several publications cited in Section 1.1 introduce these method more in depth. The fluid domain for the Green equation and the simplifications adopted are depicted below and will be used hereafter along the thesis developments. The Dirichlet and Neumann boundary conditions formulations are also written down in this chapter providing the basic nomenclature definition.

### 2.1 Brief description of the panel method

The velocity potential  $\Phi$  around a body of known shape submerged in a potential flow satisfies the irrotational, incompressible continuity equation in the body's frame of reference (Katz and Plotkin, 2001), also known as Laplace's equation:

$$\nabla^2 \Phi = 0 \quad or \quad \Delta \Phi = 0. \tag{2.1}$$

The following boundary conditions are required to solve the problem:

i A vanishing normal velocity component on the body surface,

$$\nabla \Phi \cdot \boldsymbol{n} = 0, \tag{2.2}$$

where n is the normal vector to the body surface defined such that it always points into the fluid region, as shown in Figure 2.1.

ii A constant velocity in the far field limit,

$$\lim_{r \to \infty} \nabla \Phi = \boldsymbol{V}_{\infty},\tag{2.3}$$

where  $V_{\infty}$  denotes the imposed velocity far from the body.

Using Green's identity, the general solution to Eq. (2.1) can be written as:

$$\Phi(\boldsymbol{p}) = \int_{S_B} \left( \frac{\partial \Phi}{\partial n} - \frac{\partial \Phi_{\text{int}}}{\partial n} \right) \Phi_m \, ds - \int_{S_B} \left( \Phi - \Phi_{\text{int}} \right) \nabla \Phi_m \cdot \boldsymbol{n} \, ds - \int_{S_W} \left( \Phi^+ - \Phi^- \right) \nabla \Phi_m \cdot \boldsymbol{n} \, ds + \Phi_{\infty}, \tag{2.4}$$

which gives the velocity potential  $\Phi$  at any point p outside the body. This potential is considered to be caused by a distribution, on the surface of the body  $S_B$ , of point sources of intensity  $\partial \Phi/\partial n - \partial \Phi_{\rm int}/\partial n$  and doublets of intensity  $\Phi - \Phi_{\rm int}$  oriented along axes n, and by a distribution, along the wake  $S_W$ , of doublets of intensity  $\Phi^+ - \Phi^-$  with axis of orientation n. Figure 2.1 shows the body and the relevant surfaces;  $S_B$  is the body surface,  $S_W$  is a surface discontinuity of the velocity potential with two wet faces, also known as wake, and that connects  $S_\infty$  with  $S_B$ ,  $S_\infty$  is the surface of the far field flow and  $S_\epsilon$  is the surface of a sphere in 3D or a circle in 2D that excludes the surroundings of the point p from the domain, where  $\Phi_m$  and  $\nabla \Phi_m$  take an infinite value. Note that Eq. (2.4) has been obtained taking the limit  $\epsilon \to 0$ , which reduces the integral terms in  $S_\epsilon$  to  $\Phi(p)$ . The normal vector n on the body is oriented outward while it points upward

along the wake, inward along the surface at infinity and points into the fluid region on the surface  $S_{\epsilon}$ .  $\Phi_m$  is the velocity potential produced at a point p by a point source of unit strength located on ds,  $\nabla \Phi_m \cdot n$  is the velocity potential at a point p produced by a doublet of unit strength located on ds (at the body or at the discontinuity surface) and with its axis oriented along -n,  $\Phi_{\rm int}$  is the so-called interior potential, which is required to satisfy the Laplace equation in the interior of the body,  $\Phi^+$  is the velocity potential on the upper side of the discontinuity surface  $S_W$ , and  $\Phi^-$  on the lower one, and the final term in Eq. (2.4) is the potential of the stationary flow far from the body, evaluated at p:  $\Phi_\infty = U_\infty(x\cos\alpha + y\sin\alpha)$ , where  $U_\infty = |V_\infty|$ ,  $\alpha$  is the angle between the incident flow and a reference line (angle of attack), and x and y are the coordinates of the point p in a fixed reference frame.

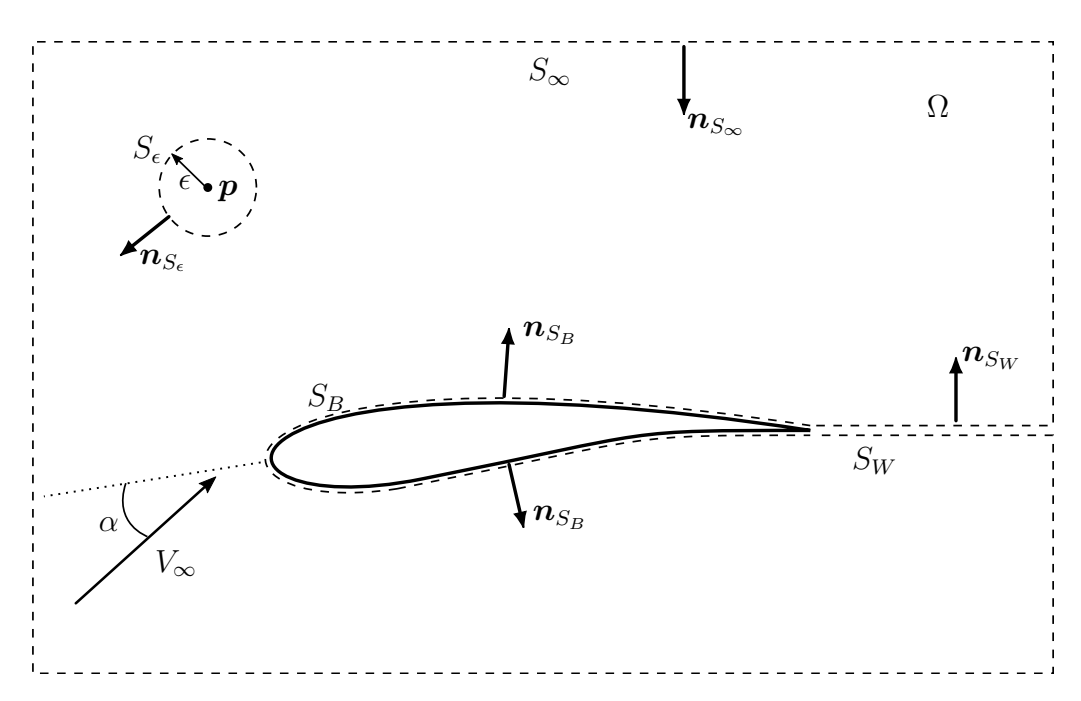


FIGURE 2.1: Fluid domain in Green's integral equation. Sketch of the body and associated surfaces: body surface  $S_B$ , wake surface  $S_W$ , point p surface  $S_\epsilon$  and a surface at infinity  $S_\infty$ .  $V_\infty$  and angle of attack representation.

Imposing Eq. (2.2) on the boundary of the body ( $\partial \Phi/\partial n = 0$ ), the velocity potential at the point  $\boldsymbol{p}$  can be written as

$$\Phi(\boldsymbol{p}) = \int_{S_B} -\frac{\partial \Phi_{\text{int}}}{\partial n} \Phi_m \, ds - \int_{S_B} (\Phi - \Phi_{\text{int}}) \nabla \Phi_m \cdot \boldsymbol{n} \, ds - \\
- \int_{S_W} (\Phi^+ - \Phi^-) \nabla \Phi_m \cdot \boldsymbol{n} \, ds + \Phi_{\infty}. \tag{2.5}$$

To simplify calculations, in what follows we take  $\Phi_{\text{int}} = 0$ . In this case the point source distribution on the body surface  $S_B$ , vanishes, and Eq. (2.5) reduces to

$$\Phi(\boldsymbol{p}) = -\int_{S_B} \Phi \nabla \Phi_m \cdot \boldsymbol{n} \, ds - \int_{S_W} (\Phi^+ - \Phi^-) \nabla \Phi_m \cdot \boldsymbol{n} \, ds + \Phi_{\infty}.$$
 (2.6)

Eq. (2.6) represents the velocity potential  $\Phi$  at a point p of a distribution of doublets on both the surface of the body and the discontinuity surface, with intensities  $\Phi$  and  $\Phi^+ - \Phi^-$  respectively and axis n.

For a 2-dimensional case, the velocity potential  $\Phi_m$  produced at a point p by a point source of unit strength located on  $x_S$  can be calculated as follows

$$\Phi_m(\boldsymbol{p}) = \frac{1}{2\pi} \log(|\boldsymbol{x}_S - \boldsymbol{p}|), \tag{2.7}$$

and using this result, the velocity potential at a point p produced by a doublet of unit strength located on  $x_S$  can be written as

$$\nabla \Phi_m(\mathbf{p}) \cdot \mathbf{n} = \frac{1}{2\pi} \frac{\mathbf{x}_S - \mathbf{p}}{|\mathbf{x}_S - \mathbf{p}|^2} \cdot \mathbf{n}.$$
 (2.8)

The potential velocity defined in Eq. (2.6) can be written for the 2-dimensional case, by introducing Eq. (2.8), as:

$$\Phi(\boldsymbol{p}) = \Phi_{\infty}(\boldsymbol{p}) - \frac{1}{2\pi} \int_{S_B} \frac{\Phi(\boldsymbol{x}_S)(\boldsymbol{x}_S - \boldsymbol{p}) \cdot \boldsymbol{n}}{|\boldsymbol{x}_S - \boldsymbol{p}|^2} ds$$
$$- \frac{1}{2\pi} \int_{S_W} (\Phi^+ - \Phi^-) \frac{(\boldsymbol{x}_S - \boldsymbol{p}) \cdot \boldsymbol{n}}{|\boldsymbol{x}_S - \boldsymbol{p}|^2} ds, \tag{2.9}$$

where  $x_S$  is the variable of integration for both surface integrals.

The basic idea of this method consists in solving the Green's integral equation by discretization of the body: the body is replaced by N straight panels, see Fig. 2.2, and it is assumed that the velocity potential  $\Phi$  is constant on each panel,  $\Phi_j$ , which correspond to a constant distribution of doublets along the panel. Each panel is defined by two limiting nodes placed on the body surface,  $\boldsymbol{x}_I^j$  and  $\boldsymbol{x}_F^j$ . In the middle point of each panel a collocation point,  $\boldsymbol{x}_{cp}^j$ , is placed (see Fig. 2.3). The numbering of the panels is in a clockwise sense, being panel 1 the first panel of the lower surface starting from the trailing edge of the obstacle and panel N the last panel of the upper surface finishing in the trailing edge. The discontinuity surface is modelled as a single panel of infinite length (numbered as panel N+1).

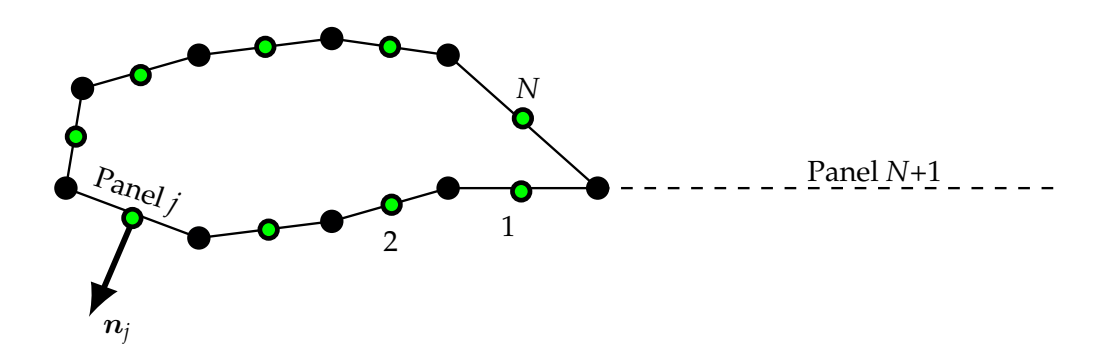


FIGURE 2.2: Discretization of geometry for a finite-thickness obstacle.

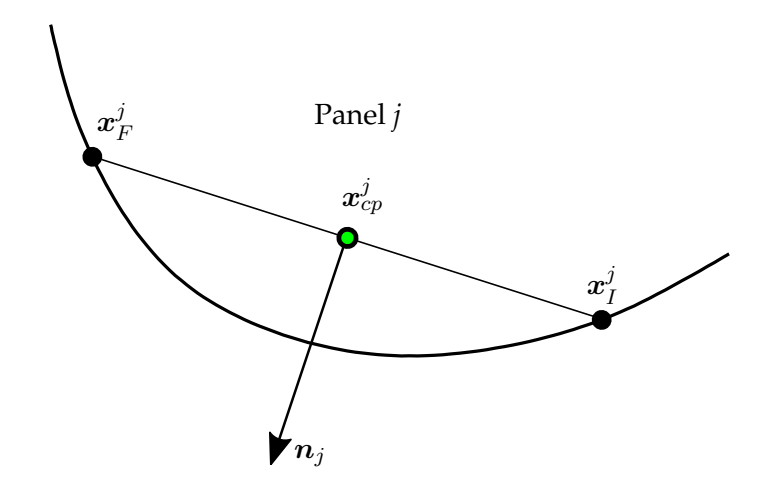


FIGURE 2.3: Body surface and panel j representation. Definition of limiting nodes  $x_I^j$  and  $x_F^j$ , collocation points  $x_{cp}^j$  and normal vector to panel  $n_j$ .

### 2.2 Review of Dirichlet and Neumann Formulations

The problem posed this way can be solved using two different kinds of boundary condition, so called in the bibliography Dirichlet boundary conditions and Neumann boundary conditions. In this section Dirichlet and Neumann formulations are reviewed and reformulated for the particular cases of interest in this thesis.

### 2.2.1 Dirichlet Formulation for Finite-Thickness Bodies

Taking the point p to be on the surface of the body reduces the problem to an integral equation for the unknown velocity potential on the surface.

In this formulation the unknown variables of the problem are the velocity potential values on each panel,  $\Phi_j$ . With the geometry discretization presented in Figure 2.2, the equations which have to be solved, in a 2-D case, are obtained by particularizing Eq. (2.9) on the N collocation points, where the first integral can be written as the sum of the integrals on each panel. The problem is reduced to

an algebraic system of equations:

$$\Phi_{k} = \Phi_{\infty_{k}} - \sum_{j=1}^{N} \frac{\Phi_{j}}{2\pi} \int_{panel} \frac{\boldsymbol{x}_{S} - \boldsymbol{x}_{cp}^{k}}{|\boldsymbol{x}_{S} - \boldsymbol{x}_{cp}^{k}|^{2}} \cdot \boldsymbol{n}_{j} ds$$

$$- \frac{\Phi_{N} - \Phi_{1}}{2\pi} \int_{panel} \frac{\boldsymbol{x}_{S} - \boldsymbol{x}_{cp}^{k}}{|\boldsymbol{x}_{S} - \boldsymbol{x}_{cp}^{k}|^{2}} \cdot \boldsymbol{n}_{N+1} ds, \qquad (2.10)$$

where  $\Phi_{\infty_k}$  is the potential of the stationary fluid far enough from the body calculated in the collocation points. Note here that the  $\Phi_j$  are constant along their panels so that they can be extracted from the integrals. Using an angular reference parallel to the discontinuity surface panel, a local frame attached to each panel (see Fig. 2.4) and the results obtained in Appendix A, Eq. (2.10) can be reformulated as:

$$\Phi_{k} = \Phi_{\infty_{k}} + \sum_{j=1}^{N} \frac{\Phi_{j}}{2\pi} \left( \theta_{kF}^{j} - \theta_{kI}^{j} \right) + \frac{\Phi_{N} - \Phi_{1}}{2\pi} \theta_{k}^{\infty}, \tag{2.11}$$

where the polar angles  $\theta_{kF}^j$ ,  $\theta_{kI}^j$  and  $\theta_k^\infty$  are defined in Fig. 2.4. Eq. (2.11) provides a system of equations where the  $\Phi_j$ , with  $j=1,\ldots,N$ , are the unknowns.

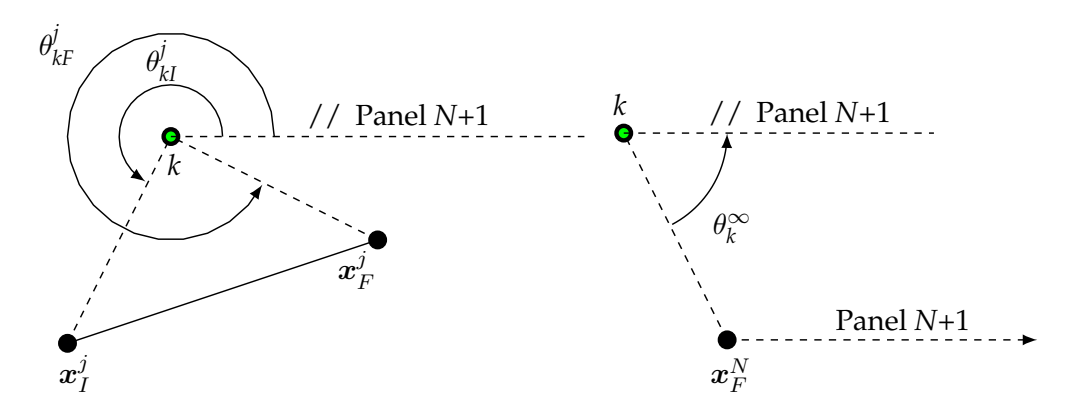


FIGURE 2.4: Definition of  $\theta_{kF}^j$ ,  $\theta_{kI}^j$  and  $\theta_k^{\infty}$ .

Note that the velocity potential of each panel, given by the term  $\frac{\Phi_j}{2\pi}\left(\theta_{kF}^j-\theta_{kI}^j\right)$  in Eq. (2.11), does not introduce any discontinuity in the fluid flow. It introduces a discontinuity segment, the straight line between the two nodes j and j+1, which models the surface of the body. The velocity potential value changes from  $\Phi_j/2$  in the upper surface to  $-\Phi_j/2$  in the lower surface of the panel since  $\theta_{kF}^j-\theta_{kI}^j$  jumps

from  $\pi$  to  $-\pi$ . To justify this last sentence, Fig. 2.5 shows a panel j, and its associated normal vector  $\boldsymbol{n}$  which is pointing to the outer flow around the body. If we let the point o tend to the panel itself,  $\theta_{kF}^j \to 2\pi$  while  $\theta_{kI}^j \to \pi$ , so  $\theta_{kF}^j - \theta_{kI}^j \to \pi$ . If we let the point i tend to the panel itself,  $\theta_{kF}^j \to 0$  while  $\theta_{kI}^j \to \pi$ , so  $\theta_{kF}^j - \theta_{kI}^j \to -\pi$ . As mentioned above, in order to solve Eq. (2.6), the point  $\boldsymbol{p}$ , in the flow outside the body, tends to the collocaction points over the body, therefore the potential on the upper surface of the panel,  $\Phi_j/2$ , which is the potential of the outer flow around the discretized body, is selected hereafter. The only discontinuity line in the fluid domain is the discontinuity surface which starts in the trailing edge of the profile and ends at infinity.

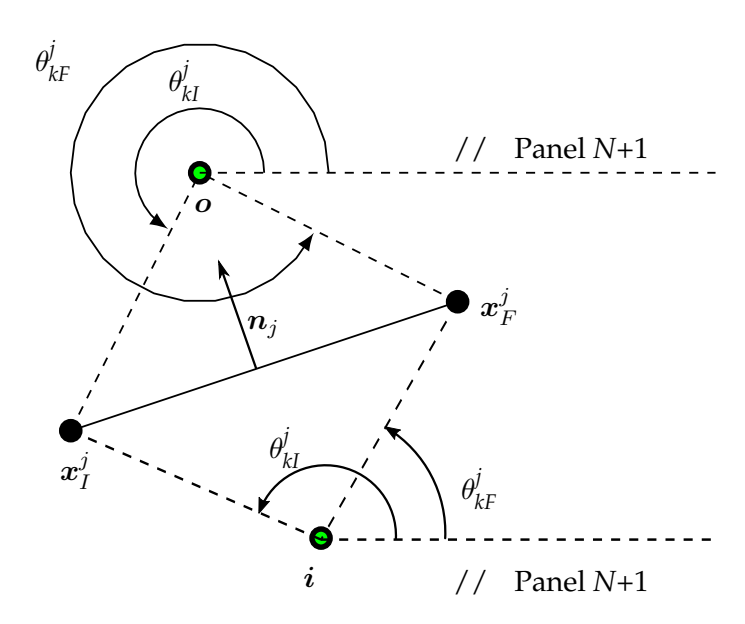


FIGURE 2.5: Representation of panel j with its associated normal vector  $\boldsymbol{n}$  pointing to the outer fluid flow. Point  $\boldsymbol{o}$  is placed inside the outer flow and point  $\boldsymbol{i}$  is placed in the inner flow (inside the body for thick airfoils).

### 2.2.2 Neumann Formulation for Zero-Thickness Bodies

Nowadays, the potential methods most widely used to solve zero-thickness bodies are the vortex-lattice method for 3D configurations and the discrete vortex method for 2D configurations (Katz and Plotkin, 2001). These methods can be derived from the Neumann formulation, where some information of the Green's integral equation is lost in the derivation.

The Neumann resolution method is based on the derivation of Eq. (2.6) and the imposition of the boundary condition  $\nabla_{x_{cp}^k} \Phi_k \cdot n_k = 0$  on the surface of the body. In this section the Neumann equations are reformulated by modeling the zero-thickness bodies by panels with two wet faces (see Fig. 2.6).

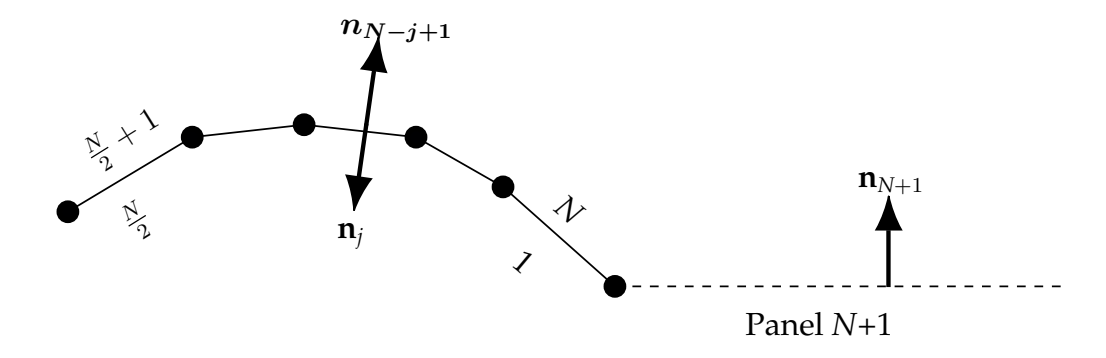


FIGURE 2.6: Discretization of geometry for a zero thickness obstacle.

Taking the advantage of the developments done in the previous section for the Dirichlet formulation in a 2-D case, Eq. (2.11) leads to

$$2\pi\Phi_{k} = 2\pi\Phi_{\infty_{k}} + \sum_{j=1}^{j=N} \Phi_{j} \left(\theta_{kF}^{j} - \theta_{kI}^{j}\right) + \left(\Phi_{N} - \Phi_{1}\right) \theta_{k}^{\infty}, \tag{2.12}$$

and expanding the summation and the discontinuity term,

$$\sum_{j=1}^{j=N} \Phi_{j} \left( \theta_{kF}^{j} - \theta_{kI}^{j} \right) + \left( \Phi_{N} - \Phi_{1} \right) \theta_{k}^{\infty} = \Phi_{1} \left( \theta_{kF}^{1} - \theta_{kI}^{1} - \theta_{k}^{\infty} \right) +$$

$$+ \Phi_{N} \left( \theta_{kF}^{N} - \theta_{kI}^{N} + \theta_{k}^{\infty} \right) + \sum_{j=2}^{j=\frac{N}{2}} \Phi_{j} \left( \theta_{kF}^{j} - \theta_{kI}^{j} \right) + \sum_{j=\frac{N}{2}+1}^{j=N-1} \Phi_{j} \left( \theta_{kF}^{j} - \theta_{kI}^{j} \right). \tag{2.13}$$

By using,

$$\theta_{kI}^1 + \theta_k^\infty = 0 \tag{2.14}$$

$$\theta_{kF}^N + \theta_k^\infty = 0 \tag{2.15}$$

$$\theta_{kI}^j = \theta_{kF}^{N+1-j} \tag{2.16}$$

and being  $\gamma_j$  the potential jump between upper and lower surfaces of the same panel (see Fig. 2.4),

$$\gamma_i = \Phi_i - \Phi_{N-i+1},\tag{2.17}$$

then, Eq. (2.13) can be rewriten as:

$$\sum_{j=1}^{j=N} \Phi_j \left( \theta_{kF}^j - \theta_{kI}^j \right) + \left( \Phi_N - \Phi_1 \right) \theta_k^{\infty} = -\gamma_N \theta_{kI}^N + \sum_{j=\frac{N}{2}+1}^{j=N-1} \gamma_j \left( \theta_{kF}^j - \theta_{kI}^j \right). \tag{2.18}$$

Using the expression in Eq. (2.18), Eq. (2.12) can be written as follows:

$$2\pi\Phi_{k} = 2\pi\Phi_{\infty_{k}} - \gamma_{N}\theta_{kI}^{N} + \sum_{j=\frac{N}{2}+1}^{j=N-1} \gamma_{j} \left(\theta_{kF}^{j} - \theta_{kI}^{j}\right), \tag{2.19}$$

and imposing the boundary condition over the body at the collocation point k,

$$\nabla_{\boldsymbol{x}_{cn}^k} \Phi_k \cdot \boldsymbol{n}_k = 0, \tag{2.20}$$

this leads to

$$0 = 2\pi \nabla_{\boldsymbol{x}_{cp}^{k}} \Phi_{\infty_{k}} \cdot \boldsymbol{n}_{k} - \gamma_{N} \theta_{kI}^{'N} + \sum_{j=\frac{N}{2}+1}^{j=N-1} \gamma_{j} \left( \theta_{kF}^{'j} - \theta_{kI}^{'j} \right), \tag{2.21}$$

where

$$\nabla_{\boldsymbol{x}_{cp}^k} \theta_k^j \cdot \boldsymbol{n}_k = \theta_k^{'j} \tag{2.22}$$

and the Kutta condition,

$$\gamma_{N+1} - \gamma_N = 0 \tag{2.23}$$

has been imposed. The expression  $\theta_k^{'j}$  is the normal component of the gradient of  $\theta_k^j$  with respect to  $\boldsymbol{x}_{cp}^k$  and is obtained from Appendix B by setting  $\boldsymbol{x} = \boldsymbol{x}_{cp}^k$  and  $\boldsymbol{y} = \boldsymbol{x}^j$  in Eq. (B.3). The expressions  $\theta_{kI}^{'j}$ ,  $\theta_{kF}^{'j}$  and  $\theta_{kI}^{'N}$  in Eq. (2.21) are obtained by

setting  ${m y}={m x}_I^j$ ,  ${m y}={m x}_F^j$  and  ${m y}={m x}_I^N$  in Eq. (B.3) respectively.

Renaming the panels in the sum in order to begin from the leading edge of the airfoil, reordering terms in Eq. (2.21) and changing the dummy index j to l=j-N/2 we finally have the algebraic system of equations that allows one to obtain M values of the jump of the potential. It is remarkable that with Neumann conditions the N unknowns of the potential cannot be obtained, but only M=N/2 unknowns: the jump of potential between the faces of the panels,  $\gamma_l$ .

$$\gamma_M \theta_{kI}^{'M} - \sum_{l=1}^{l=M-1} \gamma_l \left( \theta_{kF}^{'l} - \theta_{kI}^{'l} \right) = 2\pi \nabla_{\boldsymbol{x}_{cp}^k} \Phi_{\infty_k} \cdot \boldsymbol{n}_k$$
 (2.24)

### Chapter 3

# Panel Method for Mixed Configurations with Finite Thickness and Zero Thickness

In this chapter a new formulation is developed to solve zero-thickness bodies and mixed configurations with both finite-thickness and zero-thickness bodies. Particular developments are written for special configurations and to conclude the chapter numerical results for the pressure coefficients and their comparison with the analytical results are discussed.

## 3.1 Mixed Dirichlet-Neumann Formulation for Zero-Thickness Bodies

In this section we obtain a new formulation for zero-thickness bodies, that combines the Dirichlet formulation presented in Section 2.2.1 and the Neumann formulation presented in Section 2.2.2. First, Eq. (2.11) is duplicated and applied at the collocation points k situated on the lower surface,  $k \leq N/2$ , and upper surface, k > N/2. Here the panel numbering introduced in Fig. 2.6 is taken into

account.

$$\Phi_{k} = \Phi_{\infty_{k}} + \sum_{\substack{j=1\\j\neq k}}^{\frac{N}{2}} \frac{\Phi_{j}}{2\pi} \left(\theta_{kF}^{j} - \theta_{kI}^{j}\right) + \sum_{\substack{j=\frac{N}{2}+1\\j\neq N+1+k}}}^{N} \frac{\Phi_{j}}{2\pi} \left(\theta_{kF}^{j} - \theta_{kI}^{j}\right) + \frac{\Phi_{k}}{2} + \frac{\Phi_{N+1-k}}{2} + \frac{\Phi_{N} - \Phi_{1}}{2\pi} \theta_{k}^{\infty} \qquad \text{for } k \leq \frac{N}{2}.$$
(3.1)

$$\Phi_{k} = \Phi_{\infty_{k}} + \sum_{\substack{j=1\\j\neq N+1+k}}^{\frac{N}{2}} \frac{\Phi_{j}}{2\pi} \left(\theta_{kF}^{j} - \theta_{kI}^{j}\right) + \sum_{\substack{j=\frac{N}{2}+1\\j\neq k}}^{N} \frac{\Phi_{j}}{2\pi} \left(\theta_{kF}^{j} - \theta_{kI}^{j}\right) + \frac{\Phi_{k}}{2} + \frac{\Phi_{N+1-k}}{2} + \frac{\Phi_{N} - \Phi_{1}}{2\pi} \theta_{k}^{\infty} \qquad \text{for } k > \frac{N}{2}.$$
(3.2)

Setting l = N + 1 - j and introducing it into the first sum of Eq. (3.1) and Eq. (3.2) we have,

$$\Phi_{k} = \Phi_{\infty_{k}} + \sum_{\substack{l=N\\l\neq k}}^{\frac{N}{2}+1} \frac{\Phi_{l}}{2\pi} \left(\theta_{kF}^{l} - \theta_{kI}^{l}\right) + \sum_{\substack{j=\frac{N}{2}+1\\j\neq N+1-k}}^{N} \frac{\Phi_{j}}{2\pi} \left(\theta_{kF}^{j} - \theta_{kI}^{j}\right) + \frac{\Phi_{k}}{2} + \frac{\Phi_{N+1-k}}{2} + \frac{\Phi_{N} - \Phi_{1}}{2\pi} \theta_{k}^{\infty} \qquad \text{for } k \leq \frac{N}{2}.$$
(3.3)

$$\Phi_{k} = \Phi_{\infty_{k}} + \sum_{\substack{l=N\\l\neq k}}^{\frac{N}{2}+1} \frac{\Phi_{l}}{2\pi} \left(\theta_{kF}^{l} - \theta_{kI}^{l}\right) + \sum_{\substack{j=\frac{N}{2}+1\\j\neq k}}^{N} \frac{\Phi_{j}}{2\pi} \left(\theta_{kF}^{j} - \theta_{kI}^{j}\right) + \frac{\Phi_{k}}{2} + \frac{\Phi_{N+1-k}}{2} + \frac{\Phi_{N} - \Phi_{1}}{2\pi} \theta_{k}^{\infty} \qquad \text{for } k > \frac{N}{2}. \quad (3.4)$$

Reversing the order in the first sum of Eq. (3.3) and Eq. (3.4), taking into account

$$\theta_{kF}^{j} - \theta_{kI}^{j} = -(\theta_{kF}^{N+1-j} - \theta_{kI}^{N+1-j}), \tag{3.5}$$

noting that k is the same point on the lower and upper surfaces and identifying the corresponding potentials on the upper surface  $(\Phi_k^+)$  and lower surface  $(\Phi_k^-)$ , the equations become,

$$\Phi_{k}^{-} = \Phi_{\infty_{k}} + \sum_{\substack{j=\frac{N}{2}+1\\j\neq k}}^{N} \frac{\Phi_{j}^{+} - \Phi_{j}^{-}}{2\pi} \left(\theta_{kF}^{j} - \theta_{kI}^{j}\right) + \frac{\Phi_{k}^{-}}{2} + \frac{\Phi_{k}^{+}}{2} + \frac{\Phi_{N} - \Phi_{1}}{2\pi} \theta_{k}^{\infty}.$$
(3.6)

$$\Phi_{k}^{+} = \Phi_{\infty_{k}} + \sum_{\substack{j = \frac{N}{2} + 1 \\ j \neq k}}^{N} \frac{\Phi_{j}^{+} - \Phi_{j}^{-}}{2\pi} \left(\theta_{kF}^{j} - \theta_{kI}^{j}\right) + \frac{\Phi_{k}^{+}}{2} + \frac{\Phi_{k}^{-}}{2} + \frac{\Phi_{N} - \Phi_{1}}{2\pi} \theta_{k}^{\infty}.$$
(3.7)

Finally, using  $\gamma_j = \Phi_j^+ - \Phi_j^-$ , as defined in the previous section, we have

$$\Phi_{k}^{-} = \Phi_{\infty_{k}} + \sum_{\substack{j=1\\j\neq k}}^{M} \frac{\gamma_{j}}{2\pi} \left(\theta_{kF}^{j} - \theta_{kI}^{j}\right) - \frac{\gamma_{j}}{2} + \frac{\gamma_{M}}{2\pi} \theta_{k}^{\infty}.$$
(3.8)

$$\Phi_k^+ = \Phi_{\infty_k} + \sum_{\substack{j=1\\j \neq k}}^M \frac{\gamma_j}{2\pi} \left( \theta_{kF}^j - \theta_{kI}^j \right) + \frac{\gamma_j}{2} + \frac{\gamma_M}{2\pi} \theta_k^{\infty}.$$
 (3.9)

This system needs the Neumann formulation for zero-thickness bodies, formulated in the previous chapter, so the combined equation system is composed by Eq. (2.24), Eq. (3.8) and Eq. (3.9). The goal is to be able to calculate the N unknowns that are the potential values  $\Phi$  at each panel; N/2 unknowns in the lower side of the panels  $\Phi_k^-$  and N/2 unknowns in the upper side of the panels  $\Phi_k^+$ . From Eq. (2.24) we are able to obtain the M=N/2 jump of potential between the faces of the panels  $\gamma_j$ , which enable us to calculate the N potential values  $\Phi_k^-$  and  $\Phi_k^+$  from the system of N equations provided in Eq. (3.8) and Eq. (3.9). This development will be applied in the next section to calculate the velocity potentials on the zero-thickness part of the combined body.

and Zero Thickness

## 3.2 Formulation for Mixed Finite-Thickness and Zero-Thickness Bodies

The geometry of the body is shown in Fig. 3.1. The zero-thickness part of the body is modeled by M panels numbered from the trailing edge of the finite-thickness airfoil towards the trailing edge of the airfoil itself and with normal vectors pointing upwards. The finite-thickness part is divided in N panels numbered clockwise and starting from the lower surface trailing edge. The normal vector for the panels in the zero-thickness part points towards the upper surface. The discontinuity surface is taken as panel N+M+1 and its normal vector is oriented upwards. As in the previous case, a collocation point is placed at the center of each panel.

The solution of the coupled problem is achieved by calculating the potential jump at each of the panels of the zero-thickness part with Eq. (2.24). The potential jump of the panels of the finite-thickness part is calculated using Eq. (2.11), the definition of  $\gamma_j$  given in Eq. (2.17) and equating the potential of the inner surface of the finite-thickness panels to the internal potential, that is, zero. Thus we can write that  $\gamma_j = \Phi_j$ , with  $\Phi_j$  being the outer potential of the finite-thickness part. Eq. (2.11) can be written as follows:

$$\gamma_k = \Phi_{\infty_k} + \frac{\gamma_k}{2\pi} \left( \theta_{kF}^k - \theta_{kI}^k \right) + \sum_{\substack{j=1\\j \neq k}}^N \frac{\gamma_j}{2\pi} \left( \theta_{kF}^j - \theta_{kI}^j \right) + \frac{\gamma_N}{2\pi} \theta_k^{\infty}, \tag{3.10}$$

where  $\theta_{kF}^k - \theta_{kI}^k = \pi$ , as can be derived from the left scheme in Fig. 2.4 when letting the point k tend to the panel itself.

Finally, reordering terms in Eq. (3.10) and using the required index in the summation term, a set of algebraic equations is obtained,

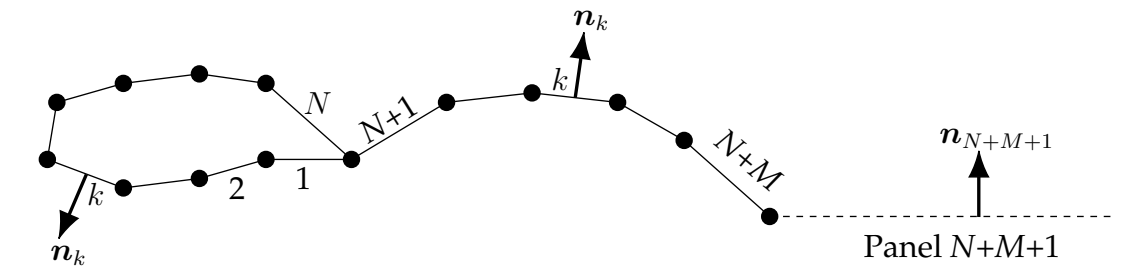


FIGURE 3.1: Mixed configuration (thick and non-thick) panel discretization.

$$\sum_{\substack{j=1\\j\neq k}}^{j=N+M} \frac{\gamma_j}{2\pi} \left(\theta_{kF}^j - \theta_{kI}^j\right) - \frac{\gamma_k}{2} + \frac{\gamma_{N+M}}{2\pi} \theta_k^{\infty} = -\Phi_{\infty_k} \text{ for } k = 1, \dots, N.$$
 (3.11)

$$\gamma_{N+M}\theta_{kI}^{'N+M} - \sum_{j=1}^{j=N+M-1} \gamma_j \left( \theta_{kF}^{'j} - \theta_{kI}^{'j} \right) = 2\pi \nabla \Phi_{\infty_k} \cdot \boldsymbol{n}_k$$

$$\text{for } k = N+1, \dots, N+M. \tag{3.12}$$

It is important to note here that Eq. (3.11) is a set of N equations for the potential jump calculation of the finite-thickness part panels, where it has been taken into account also the contribution of the potential jumps of the zero-thickness part through their inclusion in the summation term (terms  $j = N+1, \ldots, N+M$ ). Eq. (3.12) is a set of M equations that allows to calculate the potential jump of the zero-thickness part panels, where the contribution of the potential jump of the finite-thickness panels have been also included in the summation term (terms  $j = 1, \ldots, N$ ). Eq. (3.11) and Eq. (3.12) constitute a N + M set of algebraic equations, where the N+M potential jumps at each of the panels  $\gamma_k$  are the unknowns.

In matrix form,

$$[A_k^j]\{\gamma_i\} = \{b_k\}$$

$$[A_k^j] = \begin{bmatrix} -\frac{1}{2} & \frac{\theta_{1F}^2 - \theta_{1I}^2}{2\pi} & \frac{\theta_{1F}^j - \theta_{1I}^j}{2\pi} & \cdots & \frac{\theta_{1F}^{N+M} - \theta_{1I}^{N+M} + \theta_{1}^\infty}{2\pi} \\ \frac{\theta_{2F}^1 - \theta_{2I}^1}{2\pi} & -\frac{1}{2} & \frac{\theta_{2F}^j - \theta_{2I}^j}{2\pi} & \cdots & \frac{\theta_{2F}^{N+M} - \theta_{2I}^{N+M} + \theta_{2}^\infty}{2\pi} \\ \vdots & \vdots & \vdots & \vdots & \vdots & \vdots & \vdots \\ \frac{\theta_{NF}^1 - \theta_{NI}^1}{2\pi} & \frac{\theta_{NF}^j - \theta_{NI}^j}{2\pi} & \cdots & -\frac{1}{2} & \cdots & \frac{\theta_{NF}^{N+M} - \theta_{NI}^{N+M} + \theta_{N}^\infty}{2\pi} \\ \frac{\theta_{(N+1)F}^{'1} - \theta_{(N+1)I}^{'1}}{2\pi} & \frac{\theta_{(N+1)F}^{'j} - \theta_{(N+1)I}^{'j}}{2\pi} & \vdots & \vdots & \vdots & \vdots \\ \frac{\theta_{(N+M)F}^{'1} - \theta_{(N+M)I}^{'1}}{2\pi} & \frac{\theta_{(N+M)F}^{'j} - \theta_{(N+M)I}^{'j}}{2\pi} & \vdots & \vdots & \vdots & \vdots \\ \frac{\theta_{(N+M)F}^{'1} - \theta_{(N+M)I}^{'1}}{2\pi} & \frac{\theta_{(N+M)F}^{'j} - \theta_{(N+M)I}^{'j}}{2\pi} & \vdots & \vdots & \vdots & \vdots \\ \frac{\theta_{(N+M)F}^{'1} - \theta_{(N+M)I}^{'1}}{2\pi} & \frac{\theta_{(N+M)F}^{'j} - \theta_{(N+M)I}^{'j}}{2\pi} & \vdots & \vdots & \vdots & \vdots \\ \frac{\theta_{(N+M)F}^{'1} - \theta_{(N+M)I}^{'1}}{2\pi} & \frac{\theta_{(N+M)F}^{'j} - \theta_{(N+M)I}^{'j}}{2\pi} & \vdots & \vdots & \vdots & \vdots \\ \frac{\theta_{(N+M)F}^{'1} - \theta_{(N+M)I}^{'1}}{2\pi} & \frac{\theta_{(N+M)F}^{'1} - \theta_{(N+M)I}^{'1}}{2\pi} & \vdots & \vdots & \vdots & \vdots \\ \frac{\theta_{(N+M)I}^{'1}}{2\pi} & \frac{\theta_{(N+M)I}^{'1} - \theta_{(N+M)I}^{'1}}{2\pi} & \vdots & \vdots & \vdots \\ \frac{\theta_{(N+M)I}^{'1} - \theta_{(N+M)I}^{'1}}{2\pi} & \frac{\theta_{(N+M)I}^{'1} - \theta_{(N+M)I}^{'1}}{2\pi} & \vdots & \vdots & \vdots \\ \frac{\theta_{(N+M)I}^{'1} - \theta_{(N+M)I}^{'1}}{2\pi} & \frac{\theta_{(N+M)I}^{'1} - \theta_{(N+M)I}^{'1}}{2\pi} & \vdots & \vdots & \vdots \\ \frac{\theta_{(N+M)I}^{'1} - \theta_{(N+M)I}^{'1}}{2\pi} & \frac{\theta_{(N+M)I}^{'1} - \theta_{(N+M)I}^{'1}}{2\pi} & \vdots & \vdots & \vdots \\ \frac{\theta_{(N+M)I}^{'1} - \theta_{(N+M)I}^{'1}}{2\pi} & \frac{\theta_{(N+M)I}^{'1} - \theta_{(N+M)I}^{'1}}{2\pi} & \vdots & \vdots \\ \frac{\theta_{(N+M)I}^{'1} - \theta_{(N+M)I}^{'1}}{2\pi} & \frac{\theta_{(N+M)I}^{'1} - \theta_{(N+M)I}^{'1}}{2\pi} & \vdots & \vdots & \vdots \\ \frac{\theta_{(N+M)I}^{'1} - \theta_{(N+M)I}^{'1}}{2\pi} & \frac{\theta_{(N+M)I}^{'1} - \theta_{(N+M)I}^{'1}}{2\pi} & \vdots & \vdots & \vdots \\ \frac{\theta_{(N+M)I}^{'1} - \theta_{(N+M)I}^{'1}}{2\pi} & \frac{\theta_{(N+M)I}^{'1} - \theta_{(N+M)I}^{'1}}{2\pi} & \vdots & \vdots & \vdots \\ \frac{\theta_{(N+M)I}^{'1} - \theta_{(N+M)I}^{'1}}{2\pi} & \frac{\theta_{(N+M)I}^{'1} - \theta_{(N+M)I}^{'1}}{2\pi} & \vdots & \vdots & \vdots \\ \frac{\theta_{(N+M)I}^{'1} - \theta_{(N+M)I}^{'1}}{2\pi} & \frac{\theta_{(N+M)I}^{'1} - \theta_{(N+M)I}^{'1}}{2\pi} & \vdots & \vdots & \vdots \\ \frac{\theta_{(N+M)I}^{'1} - \theta_{(N+M)I}^{'1}}{2\pi} & \frac{\theta_{(N+M)I}^{'1} - \theta_{(N+M$$

$$\{\gamma_{j}\} = \begin{cases} \gamma_{1} \\ \gamma_{2} \\ \vdots \\ \gamma_{N} \\ \gamma_{N+1} \\ \vdots \\ \gamma_{N+M} \end{cases} \begin{cases} b_{k}\} = \begin{cases} -\Phi_{\infty_{1}} \\ -\Phi_{\infty_{2}} \\ \vdots \\ -\Phi_{\infty_{N}} \\ \nabla \Phi_{\infty_{N+1}} \cdot \boldsymbol{n}_{N+1} \\ \vdots \\ \nabla \Phi_{\infty_{N+M}} \cdot \boldsymbol{n}_{N+M} \end{cases} = \begin{cases} -U_{\infty}(x_{cp}^{1} \cos \alpha + y_{cp}^{1} \sin \alpha) \\ -U_{\infty}(x_{cp}^{2} \cos \alpha + y_{cp}^{2} \sin \alpha) \\ \vdots \\ -U_{\infty}(x_{cp}^{N} \cos \alpha + y_{cp}^{N} \sin \alpha) \\ -U_{\infty}(n_{x_{cp}^{N+1}} \cos \alpha + n_{y_{cp}^{N+1}} \sin \alpha) \\ \vdots \\ -U_{\infty}(n_{x_{cp}^{N+M}} \cos \alpha + n_{y_{cp}^{N+M}} \sin \alpha) \end{cases}$$

$$(3.13)$$

where the definition  $\Phi_{\infty_k} = U_\infty(x_{cp}^k \cos \alpha + y_{cp}^k \sin \alpha)$  introduced in Section 2.1 has been used. By defining  $\boldsymbol{n}_k = (n_{x_{cp}^k}, n_{y_{cp}^k})$ , with  $n_{x_{cp}^k}$  and  $n_{y_{cp}^k}$  being the coordinates of the normal vector to panel k in a fixed reference frame, it can be written that,  $\nabla \Phi_{\infty_k} = U_\infty(\cos \alpha + \sin \alpha)$ , and thus,  $\nabla \Phi_{\infty_k} \cdot \boldsymbol{n}_k = U_\infty(n_{x_{cp}^k} \cos \alpha + n_{y_{cp}^k} \sin \alpha)$ .

The resolution of the system 3.13 provides the N+M potential jumps at each of the panels  $\gamma_k$ . Now, the potential of each panel is easily obtained from Eqs. (3.8) and (3.9), and taking into account the definition of the jump of the potential, Eq. (2.17), we have

$$\Phi_{k}^{+} = \gamma_{k} 
\Phi_{k}^{-} = \Phi_{i} = 0$$
for  $k = 1, ..., N$ . (3.14)

$$\Phi_{k}^{+} = \Phi_{\infty_{k}} + \sum_{\substack{j=1\\j\neq k}}^{j=N+M} \frac{\gamma_{j}}{2\pi} \left( \theta_{kF}^{j} - \theta_{kI}^{j} \right) + \frac{\gamma_{k}}{2} + \frac{\gamma_{N+M}}{2\pi} \theta_{k}^{\infty} 
\Phi_{k}^{-} = \Phi_{k}^{+} - \gamma_{k}$$

for 
$$k = N + 1, \dots, N + M$$
. (3.15)

With the formulation developed in Eq. (3.14) and in Eq. (3.15), the velocity potential can be calculated in both the finite-thickness and the zero-thickness part.

The velocity on the body, in the fluid domain side, can be calculated using

$$V_i^+ = \frac{\Phi_i^+ - \Phi_{i-1}^+}{|x_{cp}^i - x_{cp}^{i-1}|}$$
 for  $i = 2, ..., N$ . (3.16)

$$V_i^{\pm} = \frac{\Phi_i^{\pm} - \Phi_{i-1}^{\pm}}{|x_{cp}^i - x_{cp}^{i-1}|}$$
 for  $k = N + 2, \dots, N + M$ . (3.17)

$$V_1^+ = \frac{\Phi_{N+1}^- - \Phi_1^+}{|x_{cn}^{N+1} - x_{cn}^1|}$$
 for  $i = 1$ . (3.18)

$$V_{N+1}^{+} = \frac{\Phi_{N+1}^{+} - \Phi_{N}^{+}}{|x_{cp}^{N+1} - x_{cp}^{N}|}$$
 for  $i = N + 1$  in the upper surface. (3.19)

$$V_{N+1}^{-} = \frac{\Phi_{N+1}^{-} - \Phi_{N+2}^{-}}{|x_{cr}^{N+1} - x_{cr}^{N+2}|} \qquad \text{for } i = N+1 \text{ in the lower surface.}$$
 (3.20)

where  $|x_{cp}^i - x_{cp}^{i-1}|$  is the distance between adjacent collocation points of each panel.

The pressure coefficient can be calculated on the lower and upper surfaces with

$$c_{pi}^{\pm} = 1 - \left(\frac{V_i^{\pm}}{V_{\infty}}\right)^2$$
 (3.21)

#### 3.3 Analytical solution

In the next section (3.4), numerical experiments for mixed zero-thickness and finite-thickness obstacles solved with the method proposed in section 3.1 are presented. However, it is required to have exact analytical solutions of those obstacles to compare with the numerical results and be able to analyse the accuracy of the new method. The method used to obtain the analytical solution for the mixed bodies of interest is based on the circle theorem and the conformal map transformations.

First, we give here some notes about the conformal maps (see Katz and Plotkin, 2001 for detailed developments). A body in a physical plane  $\sigma = x + iy$  is map to a body in a plane t = u + iv through a conformal mapping  $\sigma = \sigma(t)$ . Then, if the complex potential in the t plane is g(t), the complex potential in the  $\sigma$  plane is given by  $g(\sigma) = g(t(\sigma))$ . Second, the complex velocity potential expression that describes the fluid flow around a circle is very well known (see Katz and Plotkin, 2001 and Eq. (3.26)). Then, if we find the conformal map transformations required to transform a mixed zero-thickness and finite-thickness body, which is in the real plane, into a circle located in an imaginary plane, we are enabled to obtain the complex velocity potential in the real plane using the known complex velocity potential around the circle.

The body configuration in the physical plane, which consists of a curved airfoil and a camber line (see Fig. 3.2.A), is map to a circle (see Fig. 3.2.D) through three conformal transformations: one Karman-Trefftz transformation and two Joukowski transformations. Next, the complete transformation sequence shown in Fig. 3.2 is described.

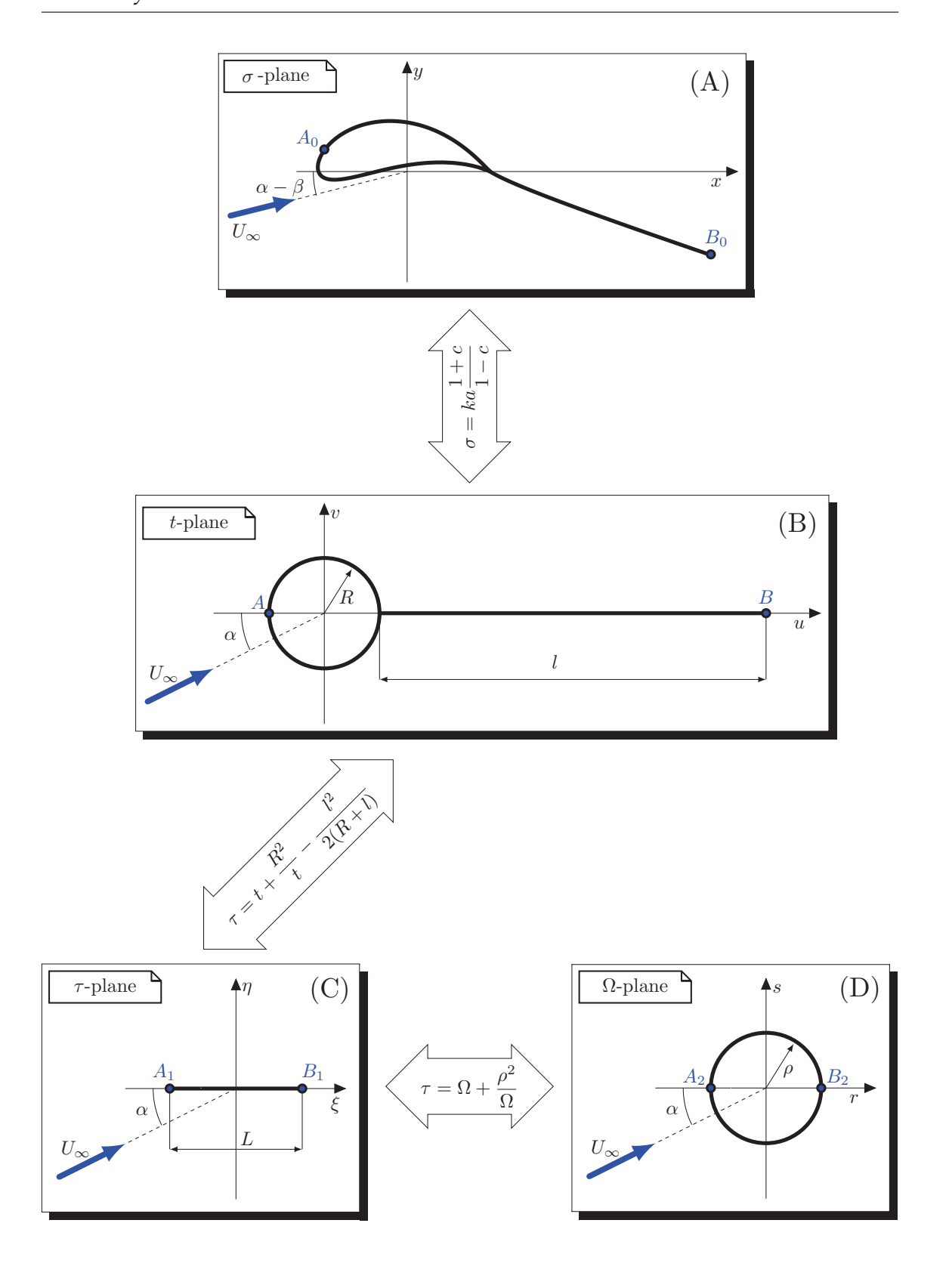


FIGURE 3.2: Complete conformal map transformation.

and Zero Thickness

First, a generalized Karman-Trefftz transformation is used to map a curved airfoil and a camber line in the real plane ( $\sigma$ -plane, Fig. 3.2.A) into a symmetric configuration formed by a circular body and a flat plate (t-plane, Fig. 3.2.B). Note that the physical angle of attack of the mixed body represented in the  $\sigma$ -plane (Fig. 3.2.A) is  $\alpha - \beta$ . This is because of the Karman-Trefftz transformation properties: the whole configuration in the t-plane is rotated an angle,  $\beta$ , about the origin,

$$\beta = \arctan\left(\frac{a\delta}{\sqrt{R^2 - (a\delta)^2}}\right),\tag{3.22}$$

and translated to point  $t_0 = a(-\lambda + i\delta)$ , where  $\delta$  and  $\lambda$  are the camber and the thickness parameters of the Karman-Trefftz transformation, R is the radius of the circular body and  $a = R/\sqrt{(1+\lambda)^2 + \delta^2}$ . Then, the Karman-Trefftz transformation leads to

$$\sigma = ka \frac{1+c}{1-c}$$
, where  $c = \left(\frac{(te^{-i\beta} + t_0) - a}{(te^{-i\beta} + t_0) + a}\right)^k$ , for  $1 \le k \le 2$ . (3.23)

The second transformation, a Joukowski transformation from the t-plane (Fig. 3.2.B) to the  $\tau$ -plane (Fig. 3.2.C), maps the circle and zero-thickness plate to a single plate, with the following expression:

$$\tau = t + \frac{R^2}{t} - \frac{l^2}{2(R+l)}. (3.24)$$

The length of the plate in the  $\tau$ -plane is:  $L = \frac{4R\left(R+l\right) + l^2}{R+l}$ .

The third transformation is a Joukowski transformation from the  $\tau$ -plane (Fig. 3.2.C) to the  $\Omega$ -plane (Fig. 3.2.D), using the following expression:

$$\tau = \Omega + \frac{\rho^2}{\Omega}$$
 with  $\rho = L/4$ . (3.25)

The circle theorem is used in the  $\Omega$ -plane (Fig. 3.2.D) and an appropriate vortex intensity is included to obtain the complex velocity potential:

$$g(\Omega) = U_{\infty} \left( \Omega e^{-i\alpha} + \frac{\rho^2}{\Omega} e^{i\alpha} \right) + \frac{i\Gamma}{2\pi} \log \Omega, \tag{3.26}$$

where

$$\Gamma = 4\pi \rho U_{\infty} \sin \alpha. \tag{3.27}$$

Now, the complex velocity potential in the physical plane,  $g(\sigma)$ , can be calculated using Eq. (3.26) and the inverse expressions of Eqs. (3.25) and (3.23) and Eq. (3.24).

#### 3.4 Numerical Results and Discussion

The upcoming sections present the numerical calculation of the pressure coefficient using the mixed Dirichlet-Neumann formulation (see section 3.1) for different obstacle topologies in which a finite-thickness body is attached to a zero-thickness tail (see section 3.3). The criteria to select the obstacles were the availability of an analytical solution and the presence of some key geometries of interest for aerodynamics. The analytical solution enables the comparison between the numerical and the exact results, so that some conclusions on the convergence of the new method can be given.

In addition, the pressure coefficient is calculated using the standard discrete vortex method, so that a direct comparison between the new method and the typical vortex method can be carried out. All the calculations of the discrete vortex method presented in the thesis have been performed using the standard method presented by Katz and Plotkin (Katz and Plotkin, 2001), in which a vortex is placed at a quarter of the panel chord and a collocation point at three quarters of the panel chord. The calculation errors in the pressure coefficients of the

proposed method are presented and compared with those of the vortex method, along with a dissertation about the results.

#### 3.4.1 Circle with a Flat Plate

The first numerical experiment attempted is making use of two very simple and basic configurations in aerodynamics theory, a circle and a flat plate, but, when assembled together, they create a not so simple configuration (see Fig. 3.3). The amount of panels in the surfaces of the thick profile and the straight line is such that their lengths are approximately the same.

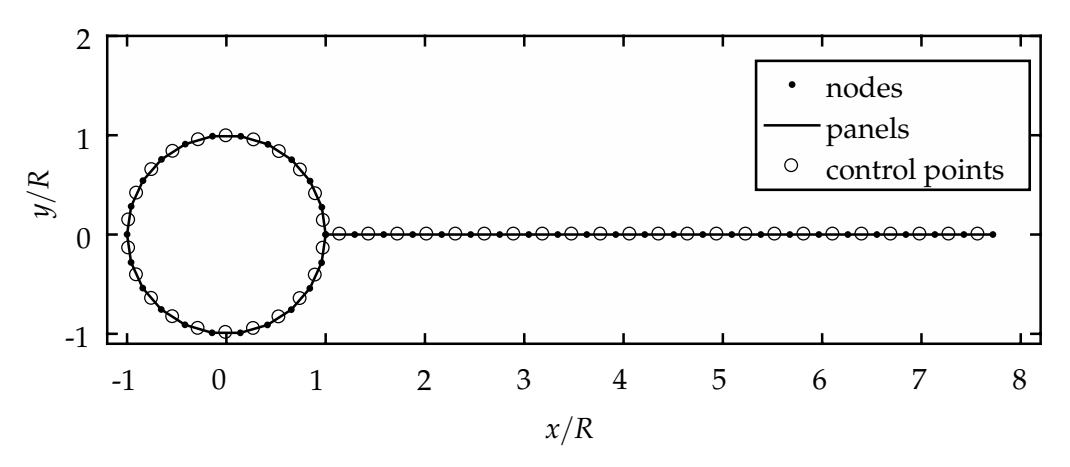
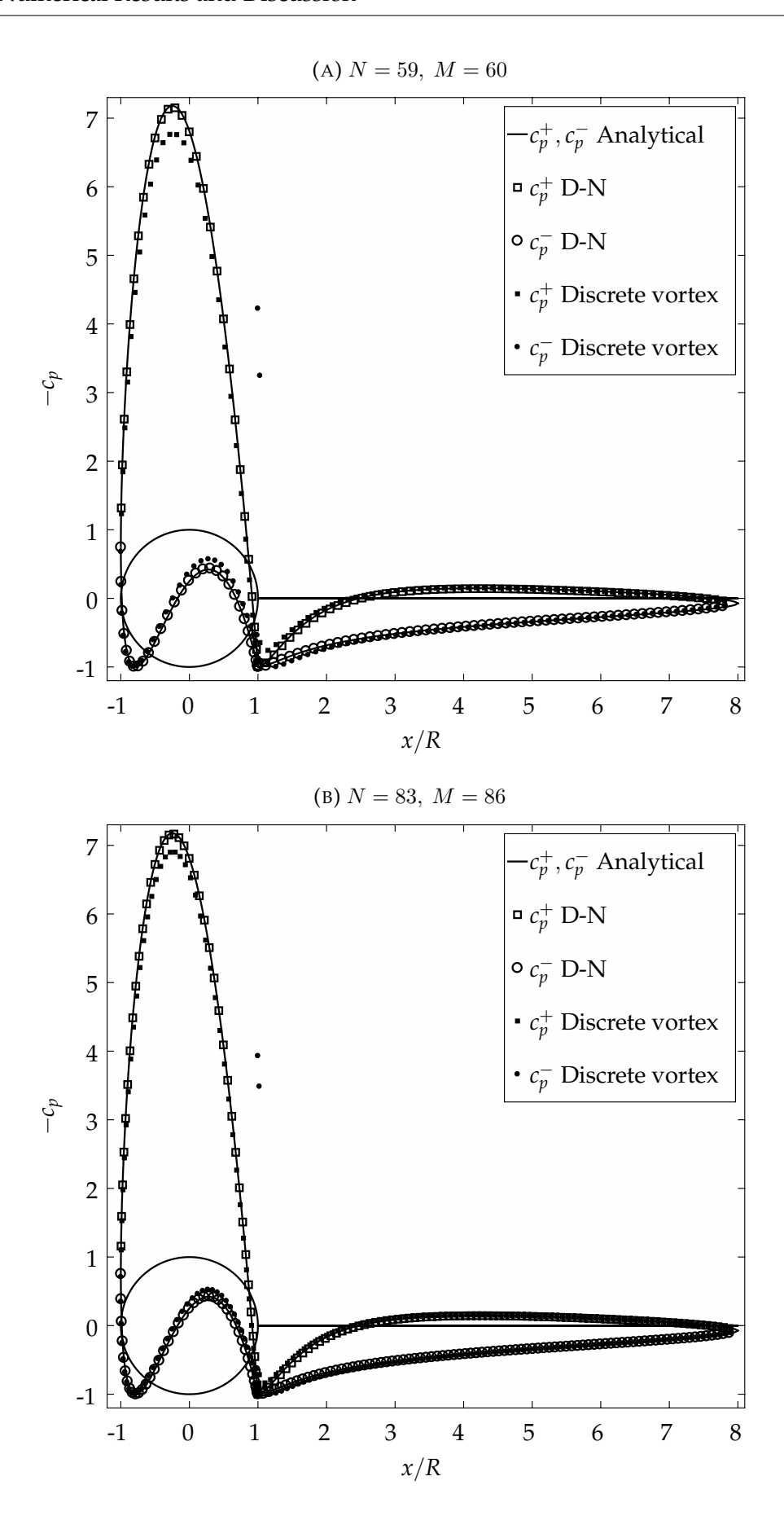


FIGURE 3.3: Circle with a flat plate body representation. The parameters of the configuration are: l/R = 7, k = 1,  $\lambda = 0$ ,  $\delta = 0$ .

Fig. 3.4 compares the pressure coefficient from the analytical solution described in Section 3.3 with the pressure coefficient obtained with the numerical scheme proposed in 3.2 and with the result obtained using the discrete vortex method. The pressure coefficient is calculated for the three methods using the definition provided in Eq. (3.21). As this figure shows, the agreement is very good even with only 59 panels for the body and 60 for the plate. The behaviour in the junction between the thickness and zero-thickness part of the body is perfectly recovered as well.



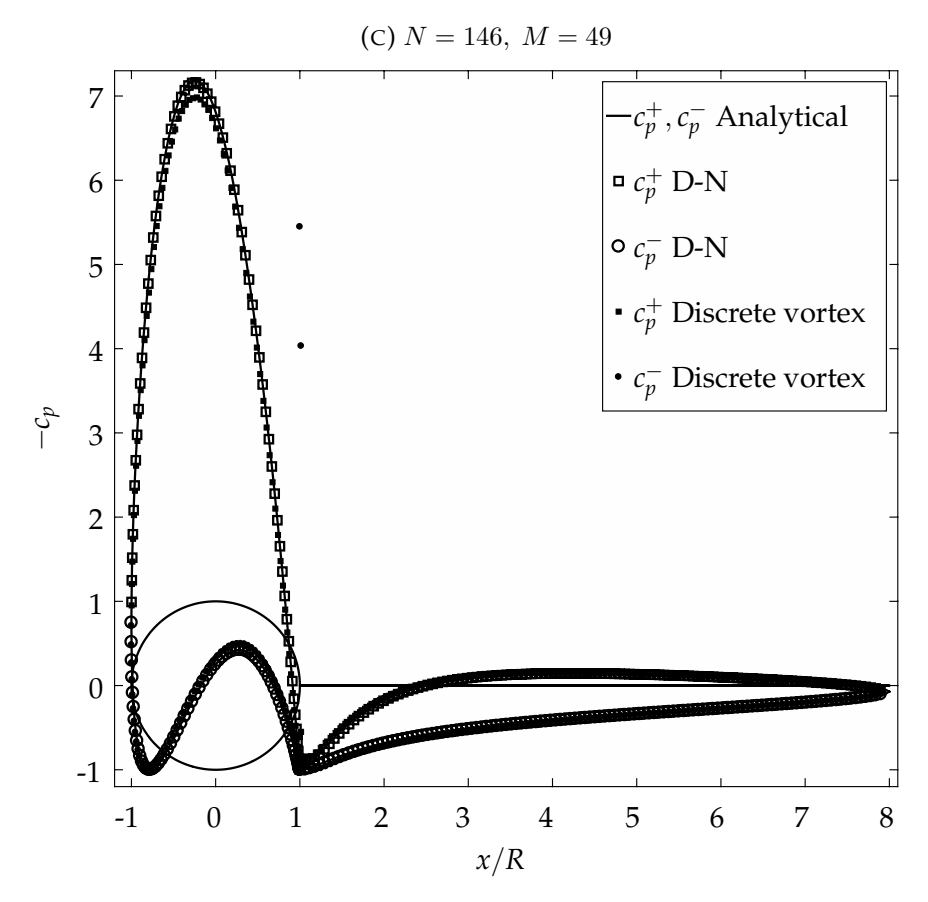


FIGURE 3.4: Comparison of the pressure coefficient obtained with the analytical solution of Section 3.3, the mixed Dirichlet-Neumann numerical approach proposed in Section 3.2 (D-N) and the discrete vortex method for different panel numbers for different panel numbers. The parameters of the configuration are:  $\alpha=12^\circ$ , l/R=7, k=1,  $\lambda=0$ ,  $\delta=0$ . The body is represented again in these figures to ease the pressure coefficient evolution visualization.

The error in the pressure coefficient is calculated as:

error= $|c_{p,\text{numerical}} - c_{p,\text{analytical}}|$  and is plotted in Fig. 3.5 computed with both numerical methods for an increasing number of panels. From Fig. 3.4 it can be stated that our method fits the analytical solution much faster, in terms of number of panels, and better than the vortex method along the finite thickness part of the body. For the zero-thickness part of the body the differences between both methods are not easily noticeable, but looking at the pressure coefficient error plots, the performance of our method is higher if close to the junction or of the same magnitude if close to the trailing edge of the tail.

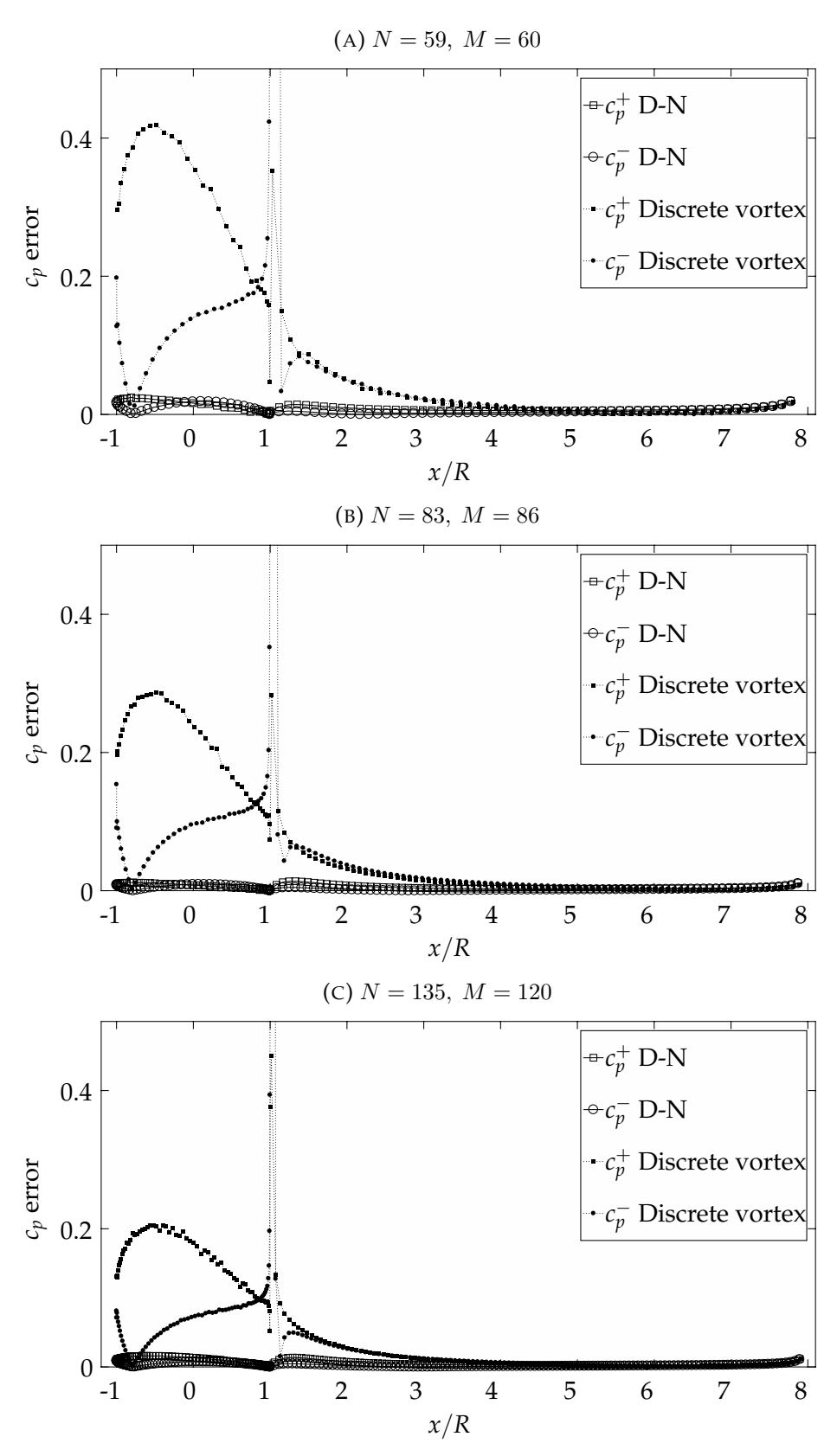


FIGURE 3.5: Error in the pressure coefficient calculated with the mixed Dirichlet-Neumann numerical approach proposed in Section 3.2 (D-N) and the discrete vortex method for different number of panels. The parameters of the configuration are:  $\alpha=12^\circ, l/R=7, k=1, \lambda=0, \delta=0$ .

and Zero Thickness

#### 3.4.2 Slender Body with a Tilted Flat Plate

A body configuration like the one shown in Fig. 3.6 could be a representative example of a shape of interest in the aerodynamics field; a slender body with a flat plate attached to its trailing edge. Here again, and for the remainder of the chapter, the number of panels in the surfaces of the thick profile and the straight line is such that their lengths are approximately the same.

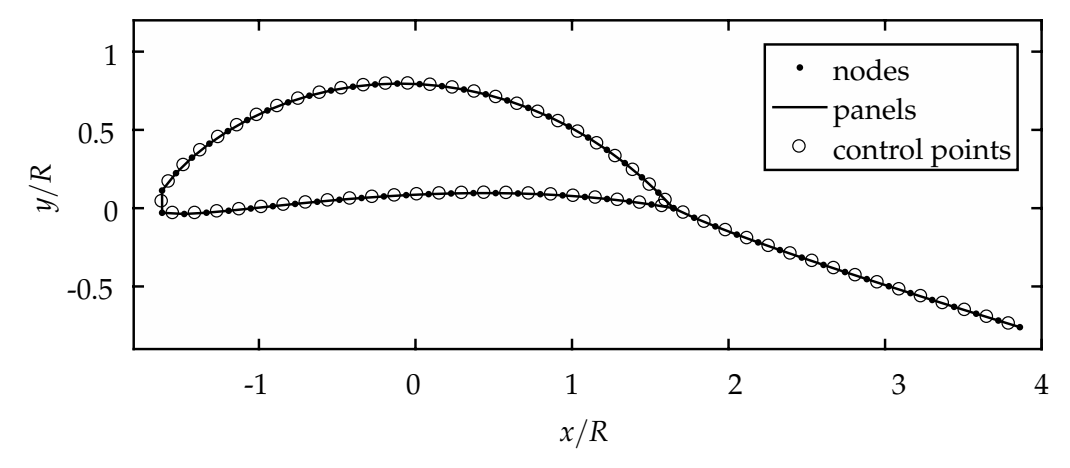
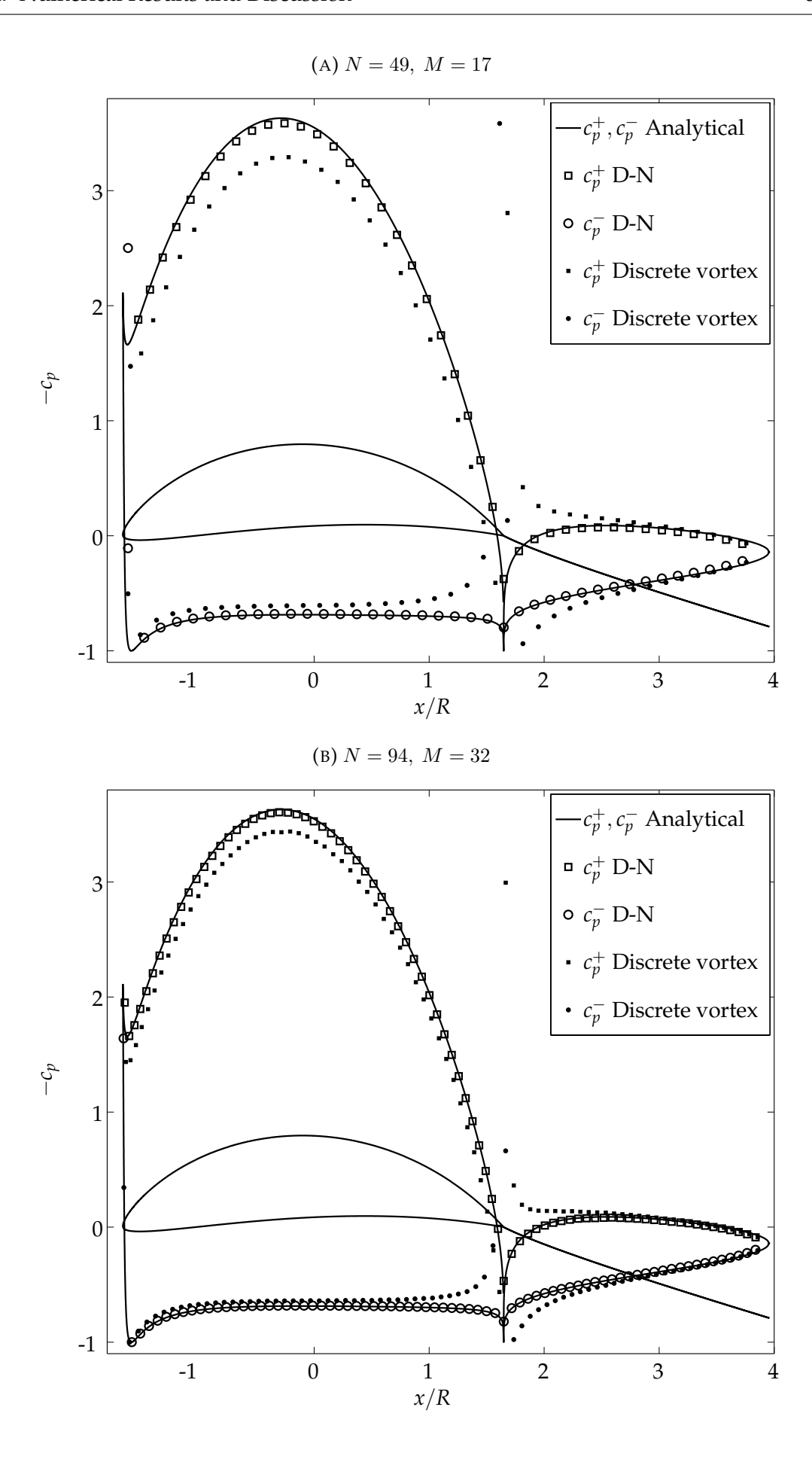


FIGURE 3.6: Slender body with a tilted flat plate body representation. The parameters of the configuration are: l/R=3, k=1.8,  $\lambda=0.05$ ,  $\delta=0.3$ .

Fig. 3.7 compares the pressure coefficient from the analytical solution described in Section 3.3 with the pressure coefficient obtained with the numerical scheme proposed in Section 3.2 and with the result obtained using the discrete vortex method.



and Zero Thickness

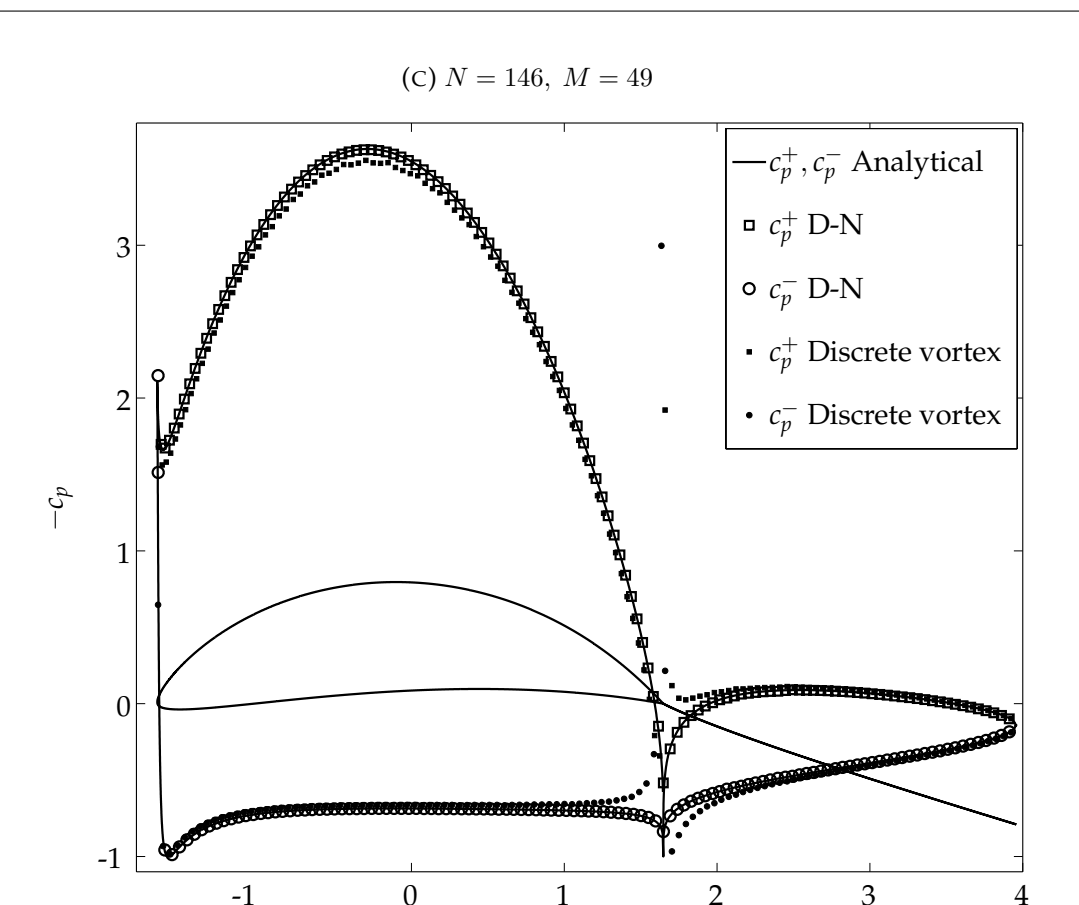


FIGURE 3.7: Pressure coefficient obtained with the analytical solution of Section 3.3, the mixed Dirichlet-Neumann numerical approach proposed in Section 3.2 (D-N) and the discrete vortex method for different panel numbers. The data of the configuration are:  $\alpha - \beta = 2^{\circ}$ , l/R = 3, k = 1.8,  $\lambda = 0.05$ ,  $\delta = 0.3$ . The body is represented again in these figures to ease the pressure coefficient evolution visualization.

x/R

2

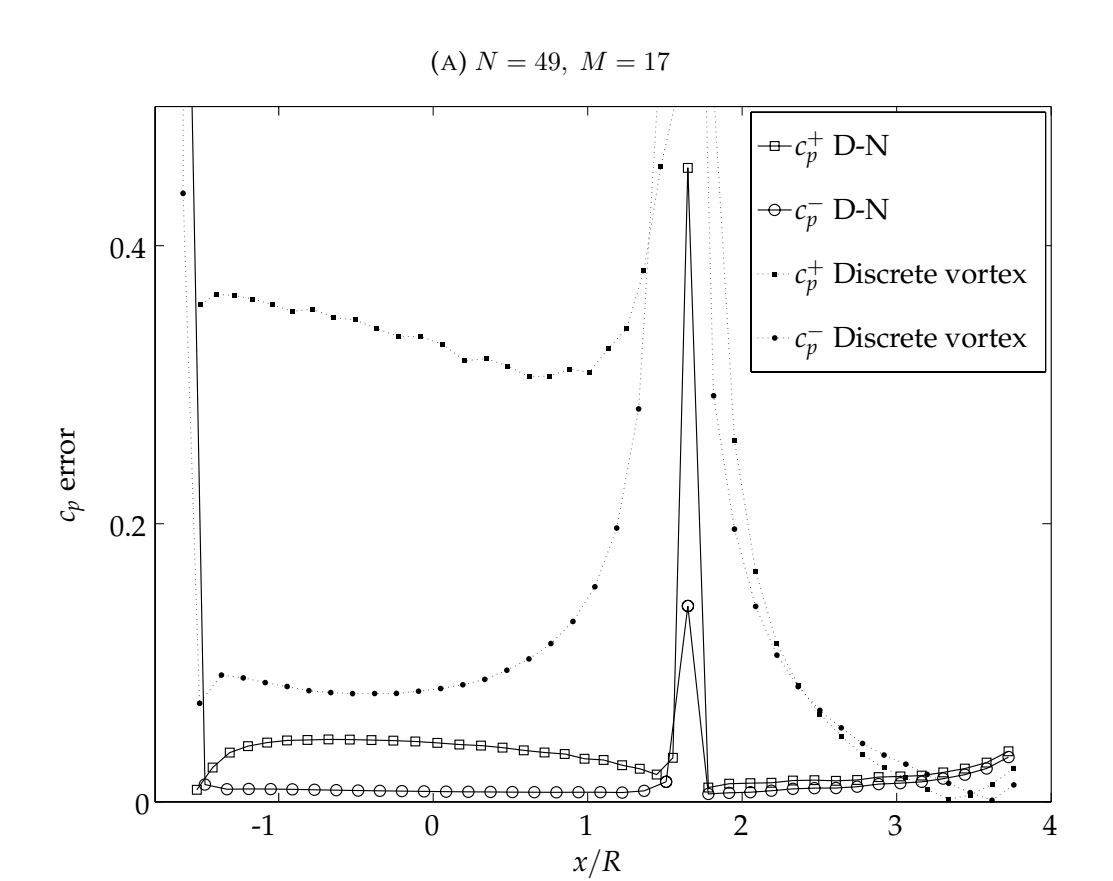
3

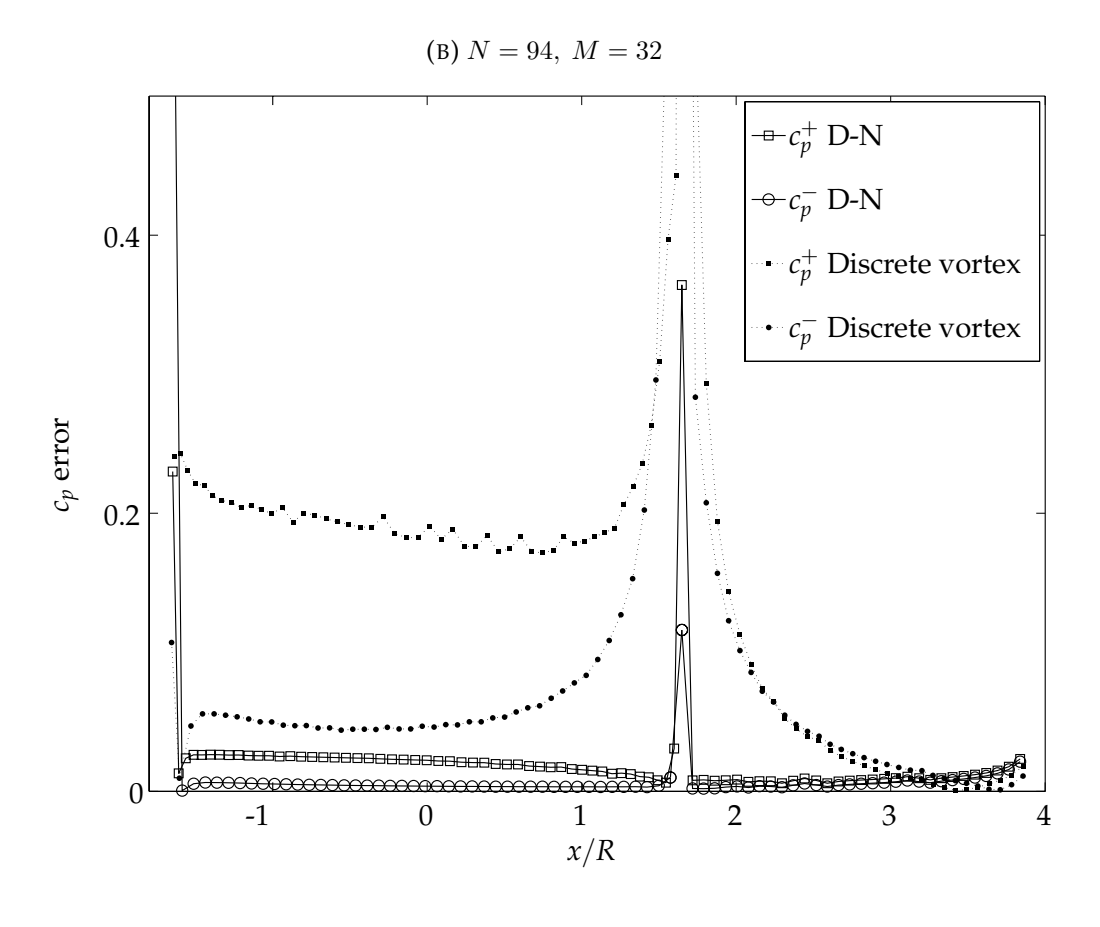
-1

The error in the pressure coefficient is calculated as: error= $|c_{p,\text{numerical}}-c_{p,\text{analytical}}|$ and is plotted in Fig. 3.8 computed with each numerical method for an increasing number of panels. These figures show that:

i The error in our method is significantly smaller than the one in discrete vortex method, and the difference is more important for a small number of panels. Increasing the number of panels in the discrete vortex method does not reduce the error to the level found in our method. For example, in the case of Fig. 3.8(c), the mean relative error with respect to the analytical solution is: 1% in the upper surface and 0.2% in the lower surface calculated with our method, and 16% in the upper surface and 10% in the lower surface calculated with the discrete vortex method.

- ii When the number of panels increases, the error of the discrete vortex method decreases, but this method never recovers correctly the behavior in the junction between the finite thickness and zero-thickness elements. The maximum error in the junction obtained with our method in case (a) is 0.4559 for  $C_p^+$  and 0.8388 for  $C_p^-$ , in case (b) is 0.3641 for  $C_p^+$  and 0.8354 for  $C_p^-$  and, in case (c), is 0.3131 for  $C_p^+$  and 0.6121 for  $C_p^-$ . The maximum error in the junction obtained with the discrete vortex method in case (a) is 3.143 for  $C_p^+$  and 4.367 for  $C_p^-$ , in case (b) is 3.423 for  $C_p^+$  and 5.069 for  $C_p^-$  and, in case (c), is 2.406 for  $C_p^+$  and 3.819 for  $C_p^-$ . Our method does significantly better in the junction even with a small number of panels.
- iii Our method fits much better than the discrete vortex method with the analytical solution in the finite thickness part. This is because the order of magnitude of the error in the discrete vortex method is the same as the order of magnitude in the Neumann method error, which is higher than the order of magnitude in the Dirichlet method error.





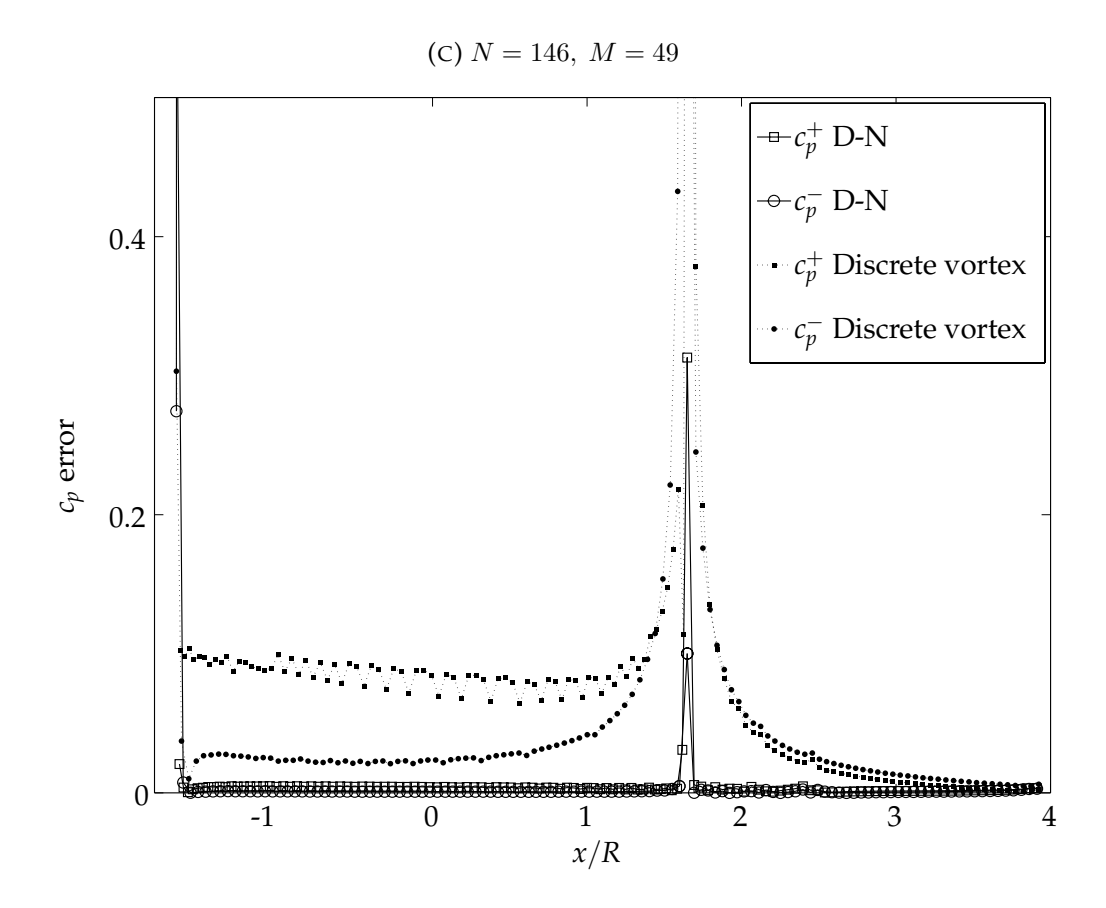


FIGURE 3.8: Error in the pressure coefficient calculated with the mixed Dirichlet-Neumann numerical approach proposed in Section 3.2 (D-N) and the discrete vortex method for different panel numbers. The data of the configuration are:  $\alpha - \beta = 2^{\circ}$ , l/R = 3, k = 1.8,  $\lambda = 0.05$ ,  $\delta = 0.3$ .

#### 3.4.3 Karman-Trefftz Body with a Cosine-shaped Camber Line

Fig. 3.9 shows a typical Karman-Trefftz body followed by a special zero-thickness part; a cosine-shaped camber line that forms a special geometry in the junction with the finite thickness part. Notice that in the lower surface the angle in the junction is greater than 180°, and therefore the velocity is infinite, whereas in the upper surface the angle is smaller than 180° and the velocity is zero.

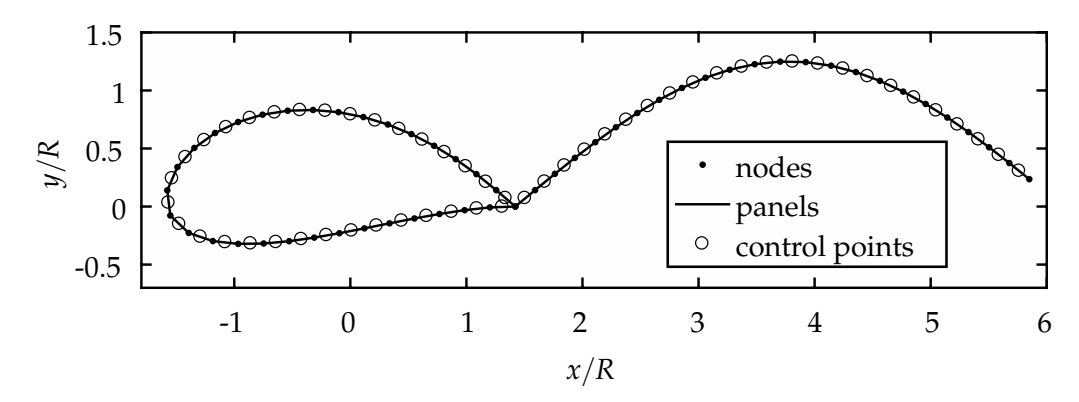
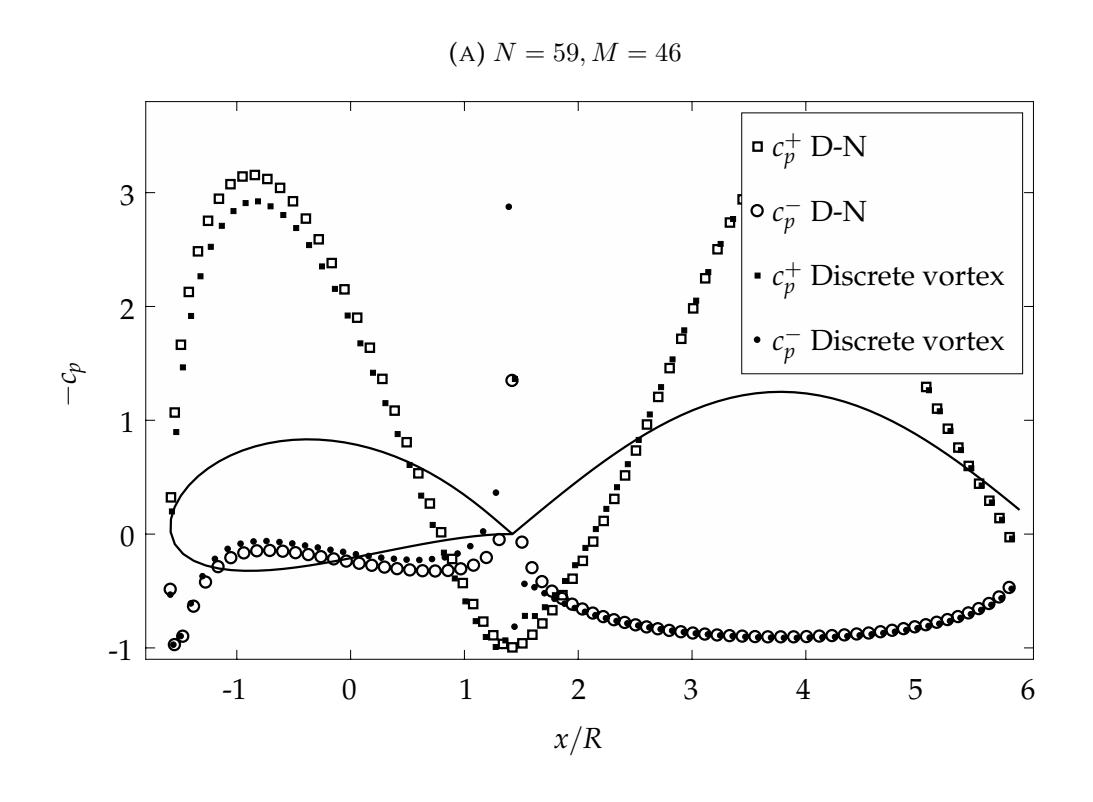
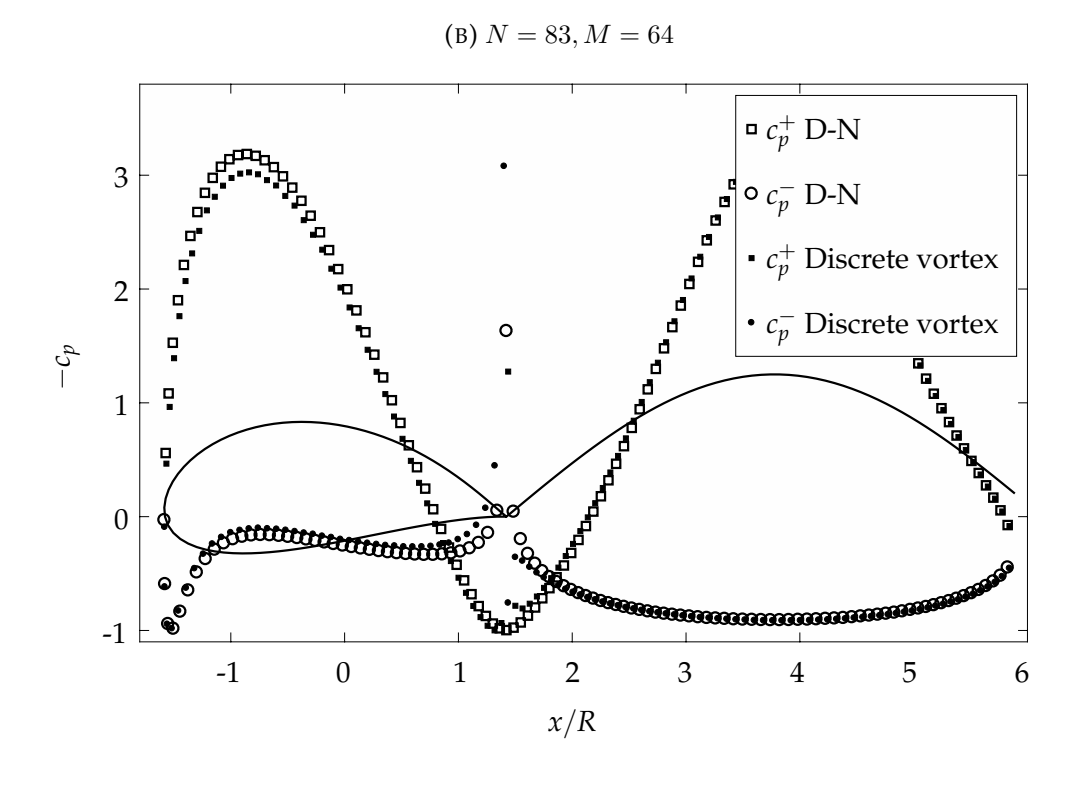


FIGURE 3.9: Karman-Trefftz body with a cosine-shaped camber line body representation. The data of the configuration are: k=1.8,  $\lambda=0.19$ ,  $\delta=0.2$ .

Fig. 3.10 shows the pressure coefficient obtained using the numerical approach of Section 3.2 and the discrete vortex method for the Karman-Trefftz body with a cosine-shaped camber line represented in Fig. 3.9. An analytical solution for this body is not available as such a camber line cannot be generated through the use of the conformal transform presented in Section 3.3, so a direct error comparison between both method is not possible. It is shown in the results that the proposed mixed Dirichlet-Neumann numerical method recovers correctly the behaviour in the junction, and from a qualitative comparison, better than the discrete vortex method if the attention is focused in the junction part and in particular in the camber line zone, where the new Dirichlet-Neumann method provides a very uniform curve. By comparison of the results for an increasing number of panels, it can be seen that the discrete vortex method results slowly tends to the mixed Dirichlet-Neuman method results, which is another proof of the goodness of this new method. Similar results are obtained with different panel number, angle of attack or body configuration.





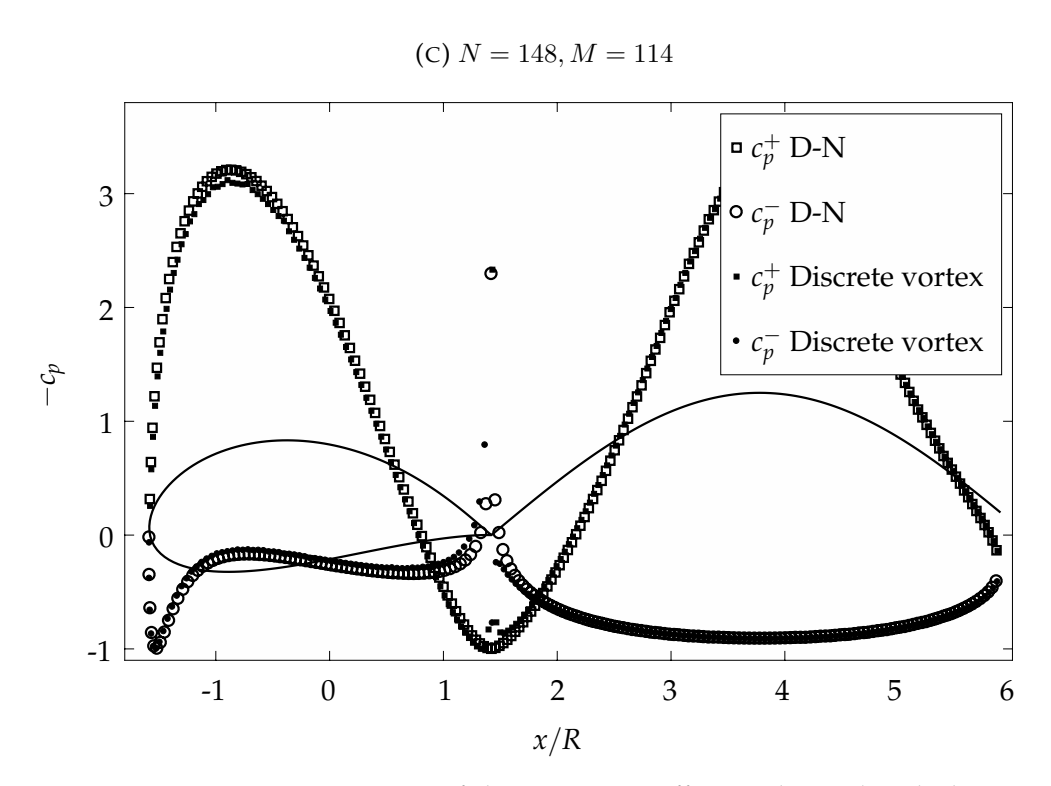


FIGURE 3.10: Comparison of the pressure coefficient obtained with the mixed Dirichlet-Neumann numerical approach proposed in Section 3.2 (D-N) and the discrete vortex method for for different panel numbers. The data of the configuration are:  $\alpha-\beta=2^\circ$ , k=1.8,  $\lambda=0.19$ ,  $\delta=0.2$ . The body is represented again in these figures to ease the pressure coefficient evolution visualization.

#### 3.4.4 Thin Symmetric Body with a Flat Plate

Fig. 3.11 shows a Karman-Trefftz profile, with k = 1.95, which gives an airfoil with 3.96% of maximum thickness and a trailing edge angle of 10.04°, followed by a flat plate.

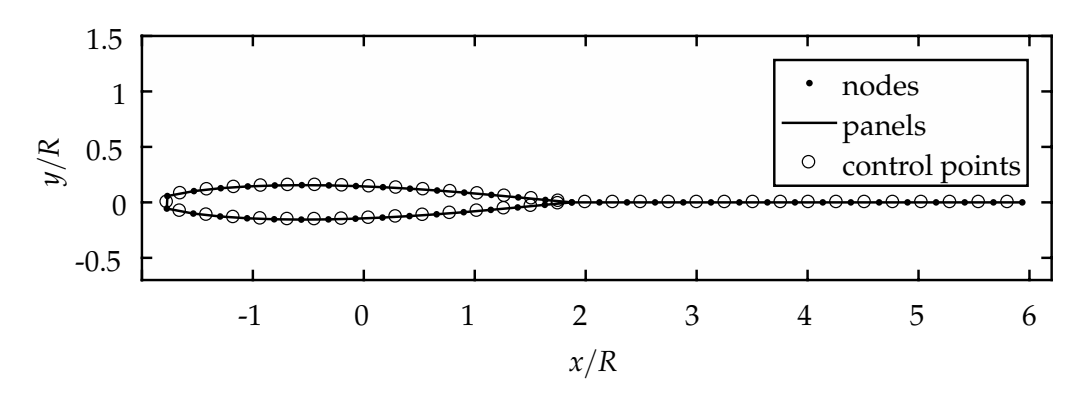


FIGURE 3.11: Thin symmetric body with a flat plate representation. The data of the configuration are: l/R=5, k=1.95,  $\lambda=0.04$ ,  $\delta=0$ .

Fig. 3.12 compares the pressure coefficient from the analytical solution described in Section 3.3 and the discrete vortex method with the pressure coefficient obtained with the numerical scheme proposed in Section 3.2 for a very thin airfoil. The pressure coefficient is calculated for an angle of the incident flow of 5°. We have used 61 panels in the airfoil and 34 panels in the tail. As can be seen the numerical solution fits extremely well with the analytical exact solution even for this very thin airfoil. It is well known that the discrete vortex method is not applicable to very thin configurations, as this one, being the error committed very high in comparison with the mixed Dirichlet-Neumann method error (see Fig. 3.13).

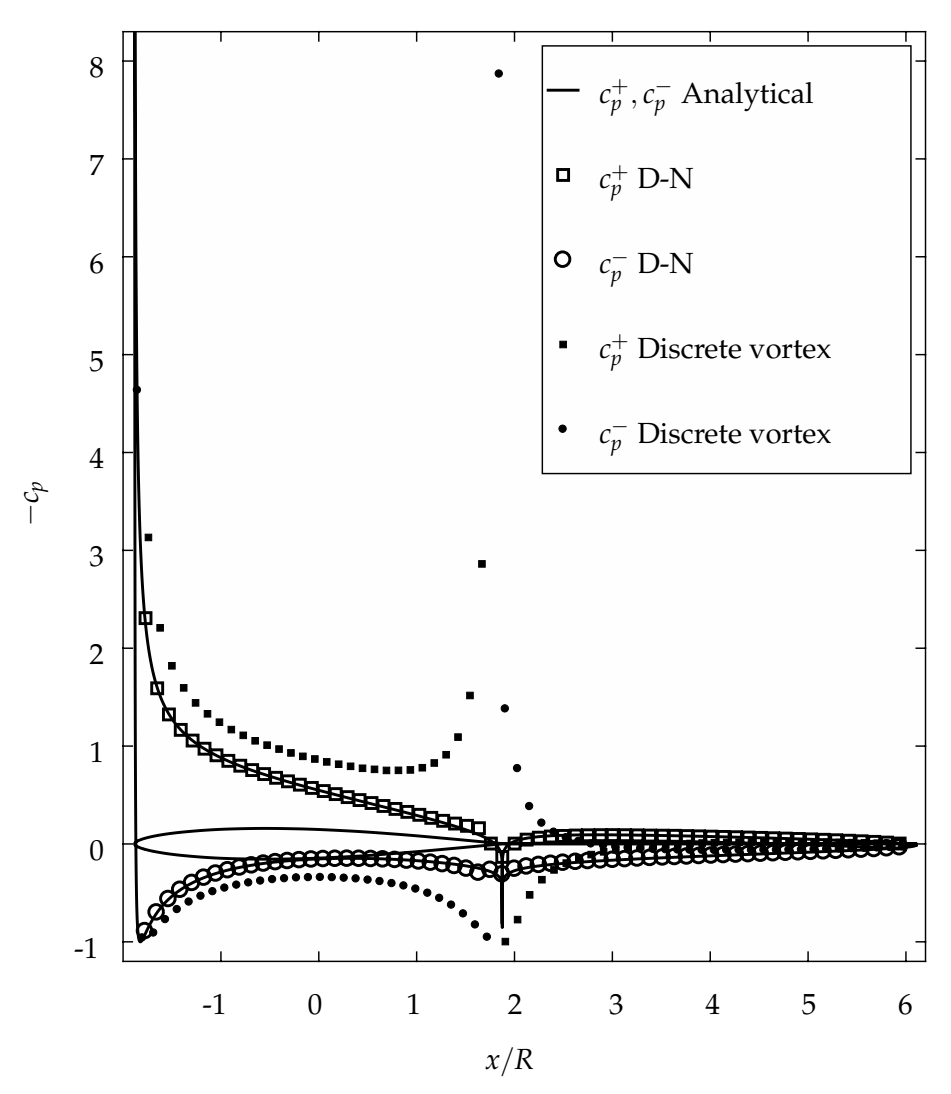


FIGURE 3.12: Comparison of the pressure coefficient obtained with the analytical solution of Section 3.3, the mixed Dirichlet-Neumann numerical approach proposed in Section 3.2 (D-N) and the discrete vortex method for different panel numbers for N=61, M=34. The parameters of the configuration are:  $\alpha=5^{\circ}$ , l/R=5, k=1.95,  $\lambda=0.04$ ,  $\delta=0$ . The body is represented again in this figure to ease the pressure coefficient evolution visualization.

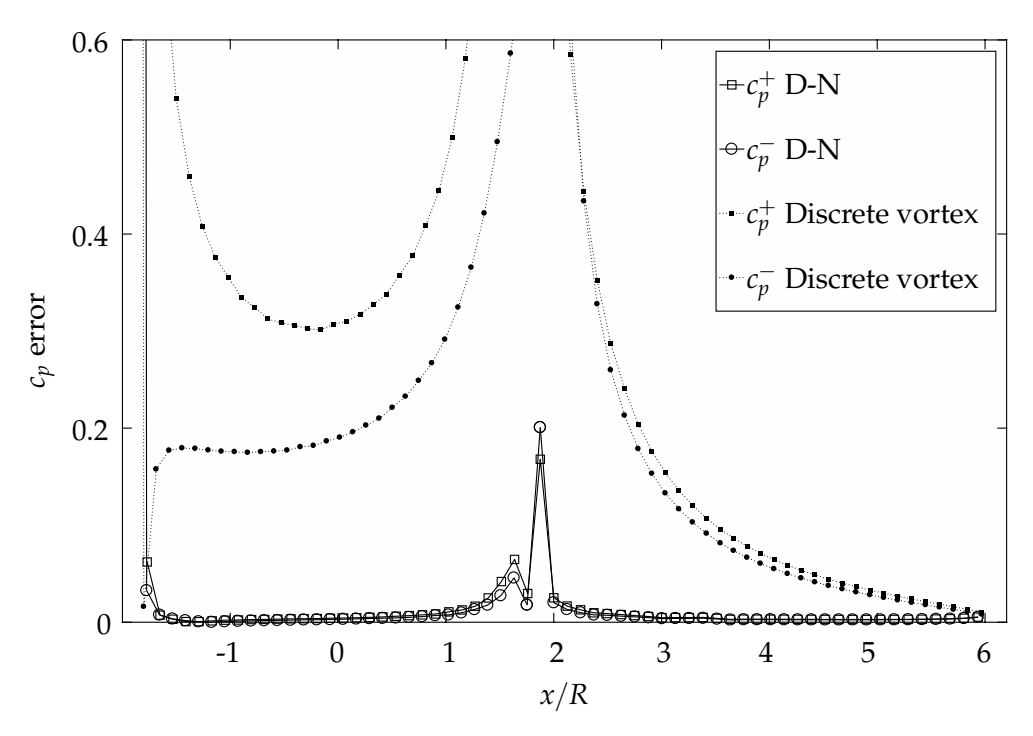


FIGURE 3.13: Error in the pressure coefficient calculated with the mixed Dirichlet-Neumann numerical approach proposed in Section 3.2 (D-N) and the discrete vortex method for N=61, M=34. The parameters of the configuration are:  $\alpha=5^{\circ}, l/R=5, k=1.95, \lambda=0.04, \delta=0$ .

#### 3.4.5 Cusped Trailing Edge Thick Body with a Tilted Flat Plate

The method here described is also capable of providing good results even for configurations with cusped trailing edges as can be seen in Fig. 3.14.

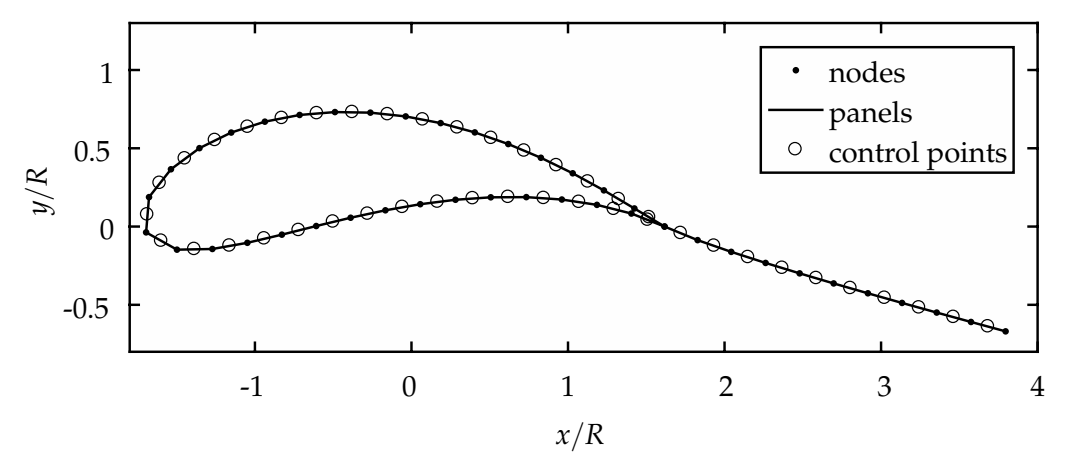
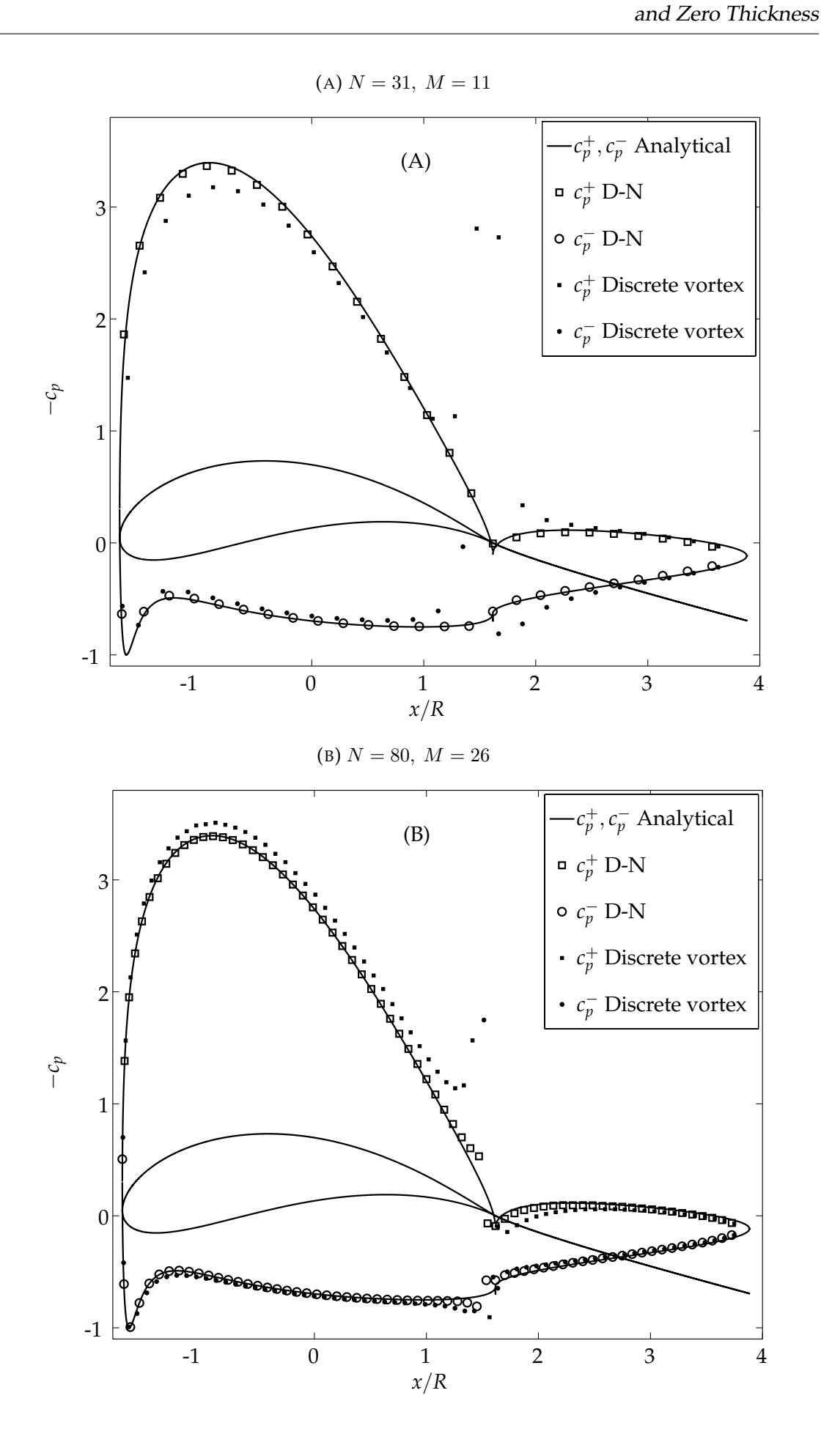


FIGURE 3.14: Cusped trailing edge thick body with a tilted flat plate representation. The data of the configuration are: l/R=3, k=2,  $\lambda=0.2$ ,  $\delta=0.3$ .

In Fig. 3.15 the pressure coefficient computed with the discrete vortex method and our method are compared to the pressure coefficient obtained with the analytical solution, for an increasing number of panels. The error in the calculation of the pressure coefficient obtained with the numerical scheme and the discrete vortex method is shown in Fig. 3.16, for an increasing number of panels. These figures show that:

- i Our method fits much better than the discrete vortex method with the analytical solution. In fact, in the discrete vortex method the error increases when the number of panels increases and this method does not converge to the analytical solution. The maximum error in the junction obtained with our method in case (a) is 0.1787 for  $C_p^+$  and 0.0970 for  $C_p^-$ , in case (b) is 0.2313 for  $C_p^+$  and 0.1256 for  $C_p^-$  and, in case (c), is 0.2368 for  $C_p^+$  and 0.1457 for  $C_p^-$ . The maximum error in the junction obtained with the discrete vortex method in case (a) is 2.732 for  $C_p^+$  and 6.603 for  $C_p^-$ , in case (b) is 4.183 for  $C_p^+$  and 2.456 for  $C_p^-$  and, in case (c), is 13.367 for  $C_p^+$  and 5.583 for  $C_p^-$ .
- ii Our method fits very well with the analytical solution even for a low number of panels. For increasing number of panels our method converges to the analytical solution, and the method performs well even near the junction.



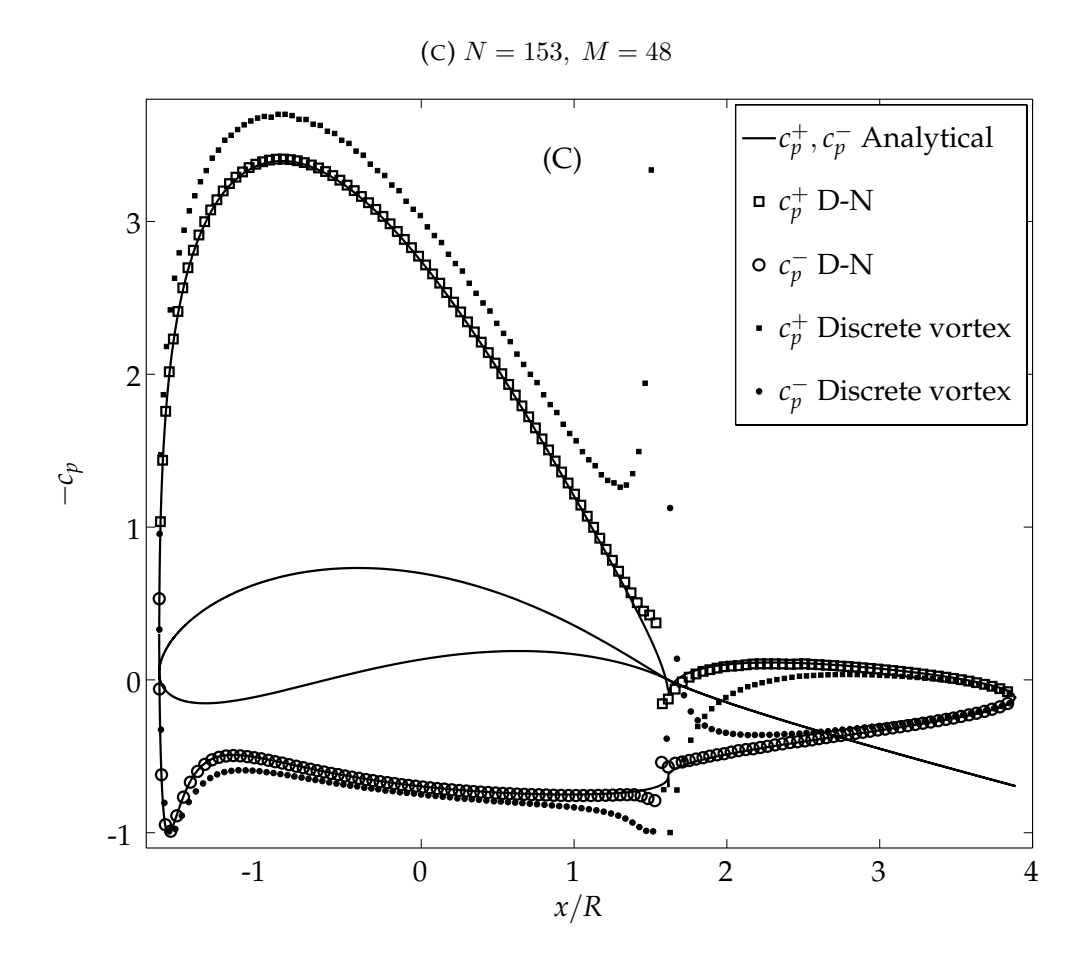
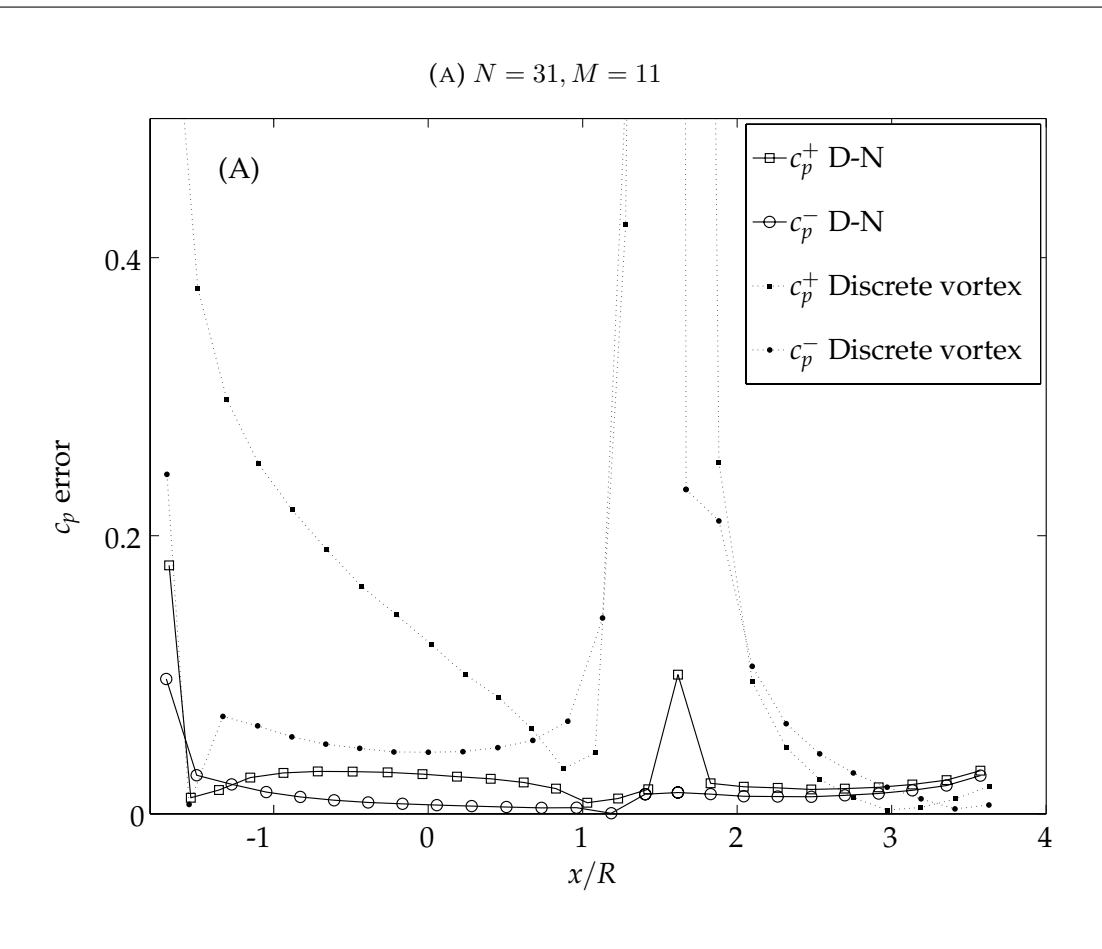
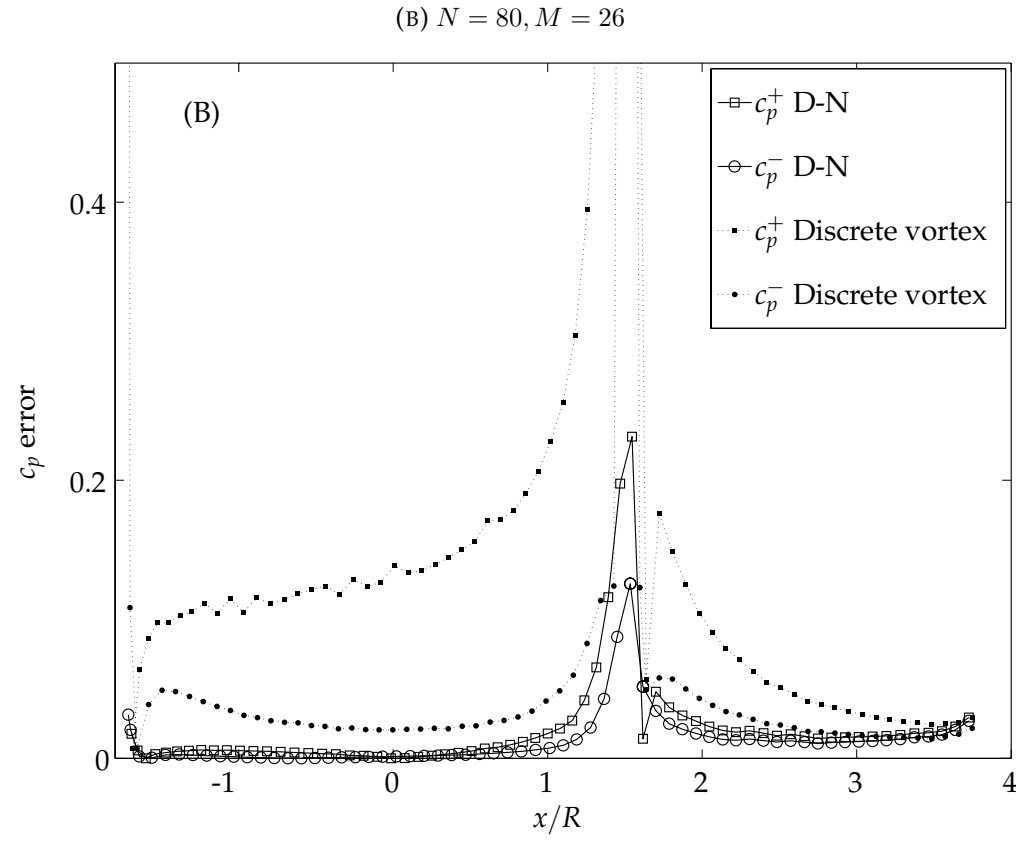


FIGURE 3.15: Pressure coefficient calculated with the analytical solution of Section 3.3, the mixed Dirichlet-Neumann numerical approach proposed in Section 3.2 (D-N) and the discrete vortex method for different panel numbers. The data of the configuration are:  $\alpha-\beta=2^{\circ}$ , l/R=3, k=2,  $\lambda=0.2$ ,  $\delta=0.3$ . The body is represented again in these figures to ease the pressure coefficient evolution visualization.





3.5. Discussions 49

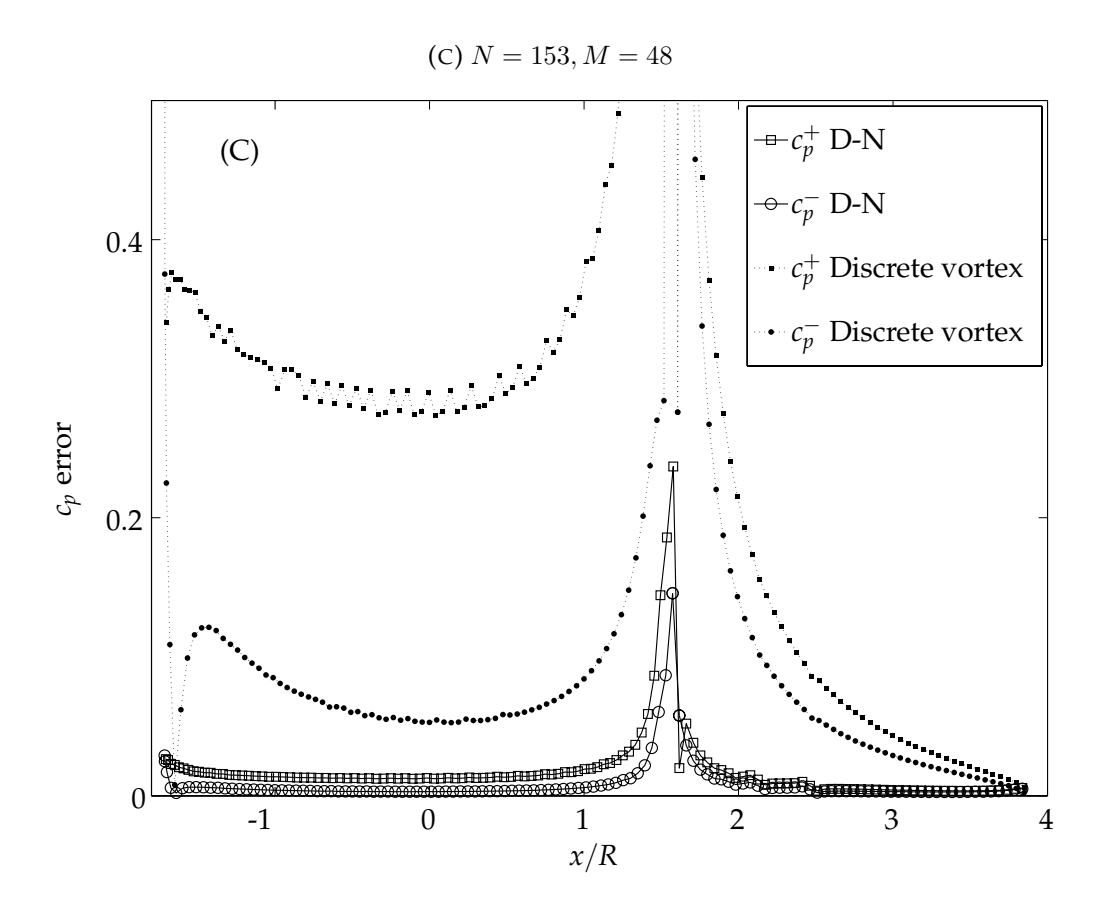


FIGURE 3.16: Error in the pressure coefficient obtained with the mixed Dirichlet-Neumann numerical approach proposed in Section 3.2 (D-N) and the discrete vortex method for different panel numbers. The data of the configuration are:  $\alpha - \beta = 2^{\circ}$ , l/R = 3, k = 2,  $\lambda = 0.2$ ,  $\delta = 0.3$ .

#### 3.5 Discussions

In this work a new formulation for combined finite-thickness and zero-thickness bodies has been developed. This formulation has been tested by comparison with analytical solutions and with the standard discrete vortex method and gives very good agreement even for very thin airfoils and airfoils with cusped trailing edge. The convergence of this new formulation has also been tested.

The method can be very useful for preliminary design in all kinds of problems that combine both finite-thickness and zero-thickness bodies; these include sailing boats, Gurney flap configurations, and the study of realistic aircraft aerodynamics.

### **Chapter 4**

# Global Error Analysis of Two-Dimensional Panel Methods for Dirichlet Formulation

This chapter introduces the efforts done in providing a formal analytical estimation of the global error assumed when employing the Dirichlet formulation to solve the Green's integral equation. The solution of this system of equations allows obtaining the velocity potential values in a discretized domain derived from an obstacle embedded in a fluid domain. The calculation of the velocity potentials in the complete fluid domain or some interesting values, e.g. the pressure coefficients or the fluid velocity around the obstacle is then a matter of straightforward computations. This computations have been performed during the years, but their level of confidence relay on the matching with physical experiments or the experience of the expert in the field. This thesis chapter provides a full global analysis that estimates the order of the errors.

Shown below is the development of the analytical and numerical problem equations so that a system of equations for the potential velocity error can be written. Then, each term is analysed and its order is estimated, yielding a result that requires to be validated. The formal analysis is then proved with several

experiments in which the obstacle velocity potentials are available, both in an analytical and numerical manner. Key considerations about the shape of the bodies under study are discussed as well as the importance of the discretization method applied when solving the numerical problem.

#### 4.1 Global error estimate for Dirichlet formulation

Here we derive an estimate for the expected numerical error upon solving Eq. (2.6) with the lower order panel method. This equation can be written as

$$\Phi(\boldsymbol{p}) = \frac{1}{2\pi} \int_{S_B} \frac{\Phi(\boldsymbol{s})(\boldsymbol{p} - \boldsymbol{s}) \cdot \boldsymbol{n}}{|\boldsymbol{p} - \boldsymbol{s}|^2} ds + \frac{\Gamma}{2\pi} \int_{S_W} \frac{(\boldsymbol{p} - \boldsymbol{\xi}_w) \cdot \boldsymbol{n}_w}{|\boldsymbol{p} - \boldsymbol{\xi}_w|^2} d\xi_w + \Phi_{\infty}(\boldsymbol{p}), \tag{4.1}$$

where, in the first integral, the variable of integration, s, is the arc length parameter along the body surface, s = s(s) is a point on the body surface  $S_B$ , and n = n(s) is the (unit) normal vector directed outward from that point. In the second integral the variable of integration is  $\xi_w$ , measuring distance along the wake panel  $S_W$ , while  $\xi_w = \xi_w(\xi_w)$  is a point on the wake panel and  $n_w$  is a unit normal vector directed upwards. The prefactor  $\Gamma = \Phi^+ - \Phi^-$  denotes the circulation around the body.

In what follows, the geometry of the body will be approximated with a collection of flat panels  $\ell_i$ , i=1..N of length  $l_i$ . We assume that the intensity of the doublet distribution is constant on each individual panel and that all panels are of comparable size, i.e, with a characteristic lengthscale l=O(1/N); hereafter, we use the Landau notation " $O(\cdot)$ " for order of magnitude. The discretization of the body surface and the wake are illustrated in Figure 4.1.

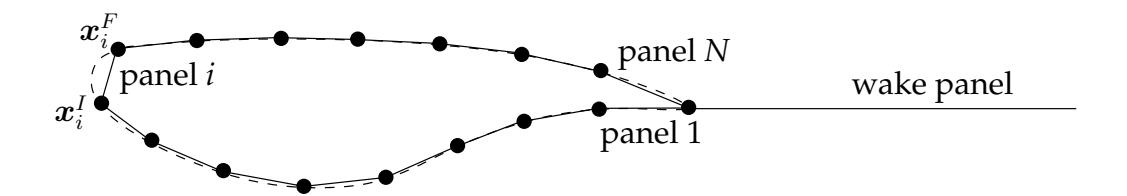


FIGURE 4.1: Discretization of the body surface.

Enumeration of the panels begins at the point of attachment of the wake, with panel number 1, and continues clockwise around the body, ultimately reaching the starting point again after panel N (this time from above the wake panel). As illustrated in Figure 4.1, the endpoints of these panels (which lie on the body surface) similarly divide the true body surface into N (curved) segments  $L_i$ . We may thus decompose the first integral term in Eq. (4.1) to get

$$\Phi(\boldsymbol{p}) = \frac{1}{2\pi} \sum_{i=1}^{N} \int_{L_{i}} \frac{\Phi(\boldsymbol{s}_{i})(\boldsymbol{p} - \boldsymbol{s}_{i}) \cdot \boldsymbol{n}}{|\boldsymbol{p} - \boldsymbol{s}_{i}|^{2}} ds_{i} + \frac{\Gamma}{2\pi} \int_{S_{W}} \frac{(\boldsymbol{p} - \boldsymbol{\xi}_{w}) \cdot \boldsymbol{n}_{w}}{|\boldsymbol{p} - \boldsymbol{\xi}_{w}|^{2}} d\xi_{w} + \Phi_{\infty}(\boldsymbol{p}),$$
(4.2)

where we use the subscript i to indicate that  $s_i$  or  $s_i$  is restricted to the curved segment  $L_i$ . The idea is to use this equation, evaluated at an appropriate point p that tends from the outside to the body surface (see Figure 4.2), and to compare the value of  $\Phi(p)$  with the "numerical" potential  $\Phi^n(p)$ , which is calculated by assuming a constant doublet distribution along each of the N panels  $\ell_i$ . This latter potential can be written as

$$\Phi^{n}(\boldsymbol{p}) = \frac{1}{2\pi} \sum_{i=1}^{N} \Phi_{i}^{n} \int_{\ell_{i}} \frac{(\boldsymbol{p} - \boldsymbol{\xi}_{i}) \cdot \boldsymbol{n}_{i}}{|\boldsymbol{p} - \boldsymbol{\xi}_{i}|^{2}} d\xi_{i} + \frac{\Gamma^{n}}{2\pi} \int_{S_{W}} \frac{(\boldsymbol{p} - \boldsymbol{\xi}_{w}) \cdot \boldsymbol{n}_{w}}{|\boldsymbol{p} - \boldsymbol{\xi}_{w}|^{2}} d\xi_{w} + \Phi_{\infty}(\boldsymbol{p}), \quad (4.3)$$

where  $\xi_i$  is a point on panel i, with  $\xi_i$  measuring distance along it (see Figure C.1 in Appendix C),  $n_i$  is an outward unit normal to this panel, and  $\Gamma^n$  is the numerically calculated circulation. The doublet strengths (potentials)  $\Phi^n_i$  are determined by evaluating Eq. (4.3) at N collocation points  $x_i$  (where we have dropped the subindex 'cp' and converted the superindex 'i' to subindex 'i' for convenience),

one located on each of the N control panels  $\ell_i$ ,

$$\Phi_i^n = \frac{1}{2\pi} \sum_{j=1}^N \Phi_j^n \int_{\ell_j} \frac{(\boldsymbol{x}_i - \boldsymbol{\xi}_j) \cdot \boldsymbol{n}_j}{|\boldsymbol{x}_i - \boldsymbol{\xi}_j|^2} d\xi_j + \frac{\Gamma^n}{2\pi} \int_{S_W} \frac{(\boldsymbol{x}_i - \boldsymbol{\xi}_w) \cdot \boldsymbol{n}_w}{|\boldsymbol{x}_i - \boldsymbol{\xi}_w|^2} d\xi_w + \Phi_{\infty}(\boldsymbol{x}_i), \quad (4.4)$$

which generates an N-dimensional linear system of equations.

We define the error as  $\varepsilon = \Phi(\mathbf{p}) - \Phi^n(\mathbf{p})$ , which, for panel *i*, becomes

$$\varepsilon_i = \Phi(\boldsymbol{p}_i) - \Phi^n(\boldsymbol{p}_i). \tag{4.5}$$

The reference point p is used to calculate the errors and, when associated with panel i, will be denoted by  $p_i$ ; the relationship between  $p_i$  and  $x_i$  is depicted in Figure 4.2.

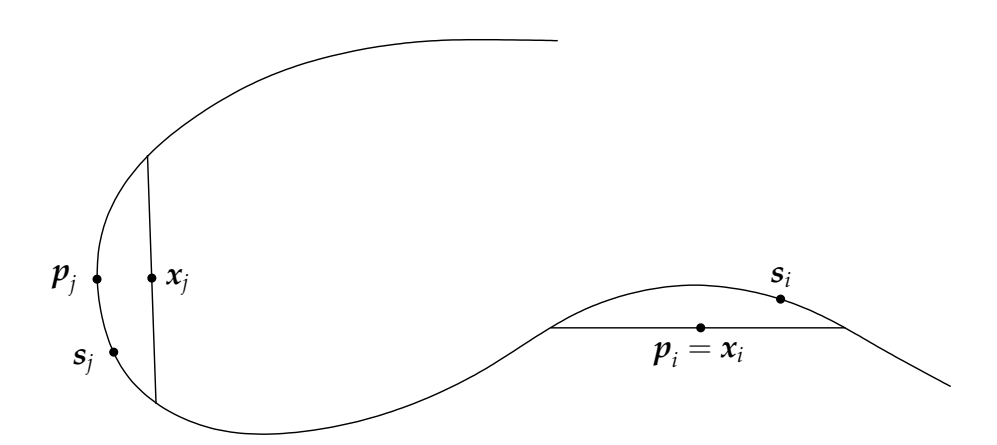


FIGURE 4.2: Relationship between  $p_i$ ,  $x_i$ , and  $s_i$  in the concave (panel i) and convex (panel j) cases.

In the convex case (the typical situation) we let the point  $p_i$  tend to the true body surface. On the other hand, if the body is concave at panel i then we let  $p_i$  tend to the panel itself (in practice, and for simplicity, we take  $p_i = x_i$ ). This distinction is necessary so that both  $\Phi$  and  $\Phi^n$  are well defined at the point of comparison  $p_i$ .

To estimate the error  $\varepsilon_i$  we take the appropriate point  $p_i$  on each panel and subtract Eq. (4.3) from Eq. (4.2) to get

$$2\pi\varepsilon_{i} = \sum_{j=1}^{N} \int_{L_{j}} \frac{\Phi(\boldsymbol{s}_{j})(\boldsymbol{p}_{i} - \boldsymbol{s}_{j}) \cdot \boldsymbol{n}}{|\boldsymbol{p}_{i} - \boldsymbol{s}_{j}|^{2}} ds_{j} - \sum_{j=1}^{N} \Phi_{j}^{n} \int_{\ell_{j}} \frac{(\boldsymbol{p}_{i} - \boldsymbol{\xi}_{j}) \cdot \boldsymbol{n}_{i}}{|\boldsymbol{p}_{i} - \boldsymbol{\xi}_{j}|^{2}} d\xi_{j} + (\Gamma - \Gamma^{n}) \int_{S_{W}} \frac{(\boldsymbol{p}_{i} - \boldsymbol{\xi}_{w}) \cdot \boldsymbol{n}_{w}}{|\boldsymbol{p}_{i} - \boldsymbol{\xi}_{w}|^{2}} d\xi_{w}.$$

$$(4.6)$$

Next, we employ the mean value theorem, writing for panels in the convex case

$$\Phi(\mathbf{s}_i) = \Phi(\mathbf{p}_i) + \frac{\partial \Phi}{\partial s}(\mathbf{z}_s) \left[ s(\mathbf{s}_i) - s(\mathbf{p}_i) \right] = 
= \Phi^n(\mathbf{p}_i) + \varepsilon_i + \frac{\partial \Phi}{\partial s}(\mathbf{z}_s) \left[ s(\mathbf{s}_i) - s(\mathbf{p}_i) \right] = 
= \Phi^n(\mathbf{x}_i) + \varepsilon_i + \psi_i(\mathbf{s}_i),$$
(4.7)

with

$$\psi_i(\boldsymbol{s}_i) = \frac{\partial \Phi}{\partial s}(\boldsymbol{z}_s) \left[ s(\boldsymbol{s}_i) - s(\boldsymbol{p}_i) \right] + \nabla \Phi^n(\boldsymbol{z}_i) \cdot (\boldsymbol{p}_i - \boldsymbol{x}_i), \tag{4.8}$$

where s is the aforementioned arc parameter but could, in principle, be any scalar variable that parameterizes a path tending to the body surface from outside (where  $\Phi$  is well-defined) connecting  $s_i$  and  $p_i$ . The point  $z_s$  is located along that path, while  $z_i$  is another point (on a line segment) between  $p_i$  and  $x_i$ .

In the concave case we set  $p_i = x_i$  and write

$$\Phi(\mathbf{s}_i) = \Phi(\mathbf{x}_i) + \psi_i(\mathbf{s}_i) = \Phi^n(\mathbf{x}_i) + \varepsilon_i + \psi_i(\mathbf{s}_i), \tag{4.9}$$

with

$$\psi_i(\mathbf{s}_i) = \nabla \Phi(\mathbf{z}_s) \cdot (\mathbf{s}_i - \mathbf{x}_i). \tag{4.10}$$

In the above,  $z_s$  is a point (on a line segment) between  $s_i$  and  $x_i$ . Note that the only difference between the convex and concave cases is in the definition of  $\psi_i$ .

By introducing Eqs. (4.7) and (4.9) in Eq. (4.6), we obtain

$$2\pi\varepsilon_{i} = \sum_{j=1}^{N} \int_{L_{j}} \frac{\left[\Phi_{j}^{n} + \varepsilon_{j} + \psi_{j}(\boldsymbol{s}_{j})\right](\boldsymbol{p}_{i} - \boldsymbol{s}_{j}) \cdot \boldsymbol{n}}{|\boldsymbol{p}_{i} - \boldsymbol{s}_{j}|^{2}} ds_{j}$$
$$- \sum_{j=1}^{N} \Phi_{j}^{n} \int_{\ell_{j}} \frac{(\boldsymbol{p}_{i} - \boldsymbol{\xi}_{j}) \cdot \boldsymbol{n}_{j}}{|\boldsymbol{p}_{i} - \boldsymbol{\xi}_{j}|^{2}} d\xi_{j} + (\Gamma - \Gamma^{n}) \delta_{i\infty}. \tag{4.11}$$

Note the fact that

$$\int_{C} \frac{(\boldsymbol{p}_{i} - \boldsymbol{s}_{j}) \cdot \boldsymbol{n}}{|\boldsymbol{p}_{i} - \boldsymbol{s}_{j}|^{2}} ds_{j} = \int_{C} d\theta_{p_{i}s_{j}} = \theta_{p_{i}x_{j}}^{F} - \theta_{p_{i}x_{j}}^{I} = \delta_{ij}, \tag{4.12}$$

where  $\theta_{p_is_j}$  is the (polar) angle associated with the vector  $\mathbf{s}_j - \mathbf{p}_i$  (see Figure 4.3), a function of the position  $\mathbf{s}_j$  along a path C,  $\theta_{p_ix_j}^I$ , corresponds to the node  $\mathbf{x}_j^I$  of panel j, and  $\theta_{p_ix_j}^F$ , corresponds to the node  $\mathbf{x}_j^F$  and  $\delta_{ij}$  is the angle subtended by panel j as viewed from  $\mathbf{p}_i$ . The reference axis for  $\theta_{p_is_j}$  is taken parallel to the wake panel.

Eq. (4.12) shows that the value of the integral on the left-hand side only depends on the relative position between the endpoints of the path C, and therefore

$$\int_{L_j} \frac{(\boldsymbol{p}_i - \boldsymbol{s}_j) \cdot \boldsymbol{n}}{|\boldsymbol{p}_i - \boldsymbol{s}_j|^2} ds_j = \int_{\ell_j} \frac{(\boldsymbol{p}_i - \boldsymbol{\xi}_j) \cdot \boldsymbol{n}_j}{|\boldsymbol{p}_i - \boldsymbol{\xi}_j|^2} d\xi_j = \delta_{ij}.$$
(4.13)

One important conclusion can be written at this point regarding the use of curved panels instead of flat panels for the body discretization. Note that in Eq. (4.4), used to calculate the numerical values of the velocity potential,  $\delta_{ij}$  is the angle subtended by panel j as viewed from  $x_i$ , which is a point located on the panel itself. If instead of using flat panels for the body discretization, we use curved panels, the point  $x_i$  turns to be located on the curved line while the integration limits used to calculate the value of  $\delta_{ij}$ , the endpoints of panel j, are not modified. This allow us to write the following statement: the only difference in

the numerical calculations if curved panels are used instead of flat panels, is the position of  $x_i$ , which is placed on the curved panel instead of on the flat one (see Figure 4.3).

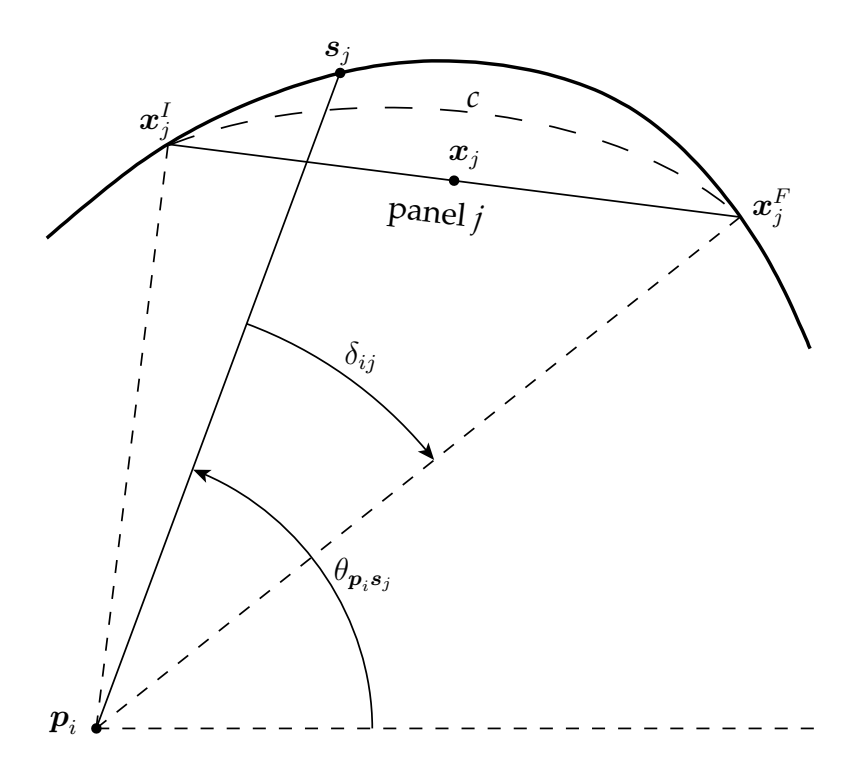


FIGURE 4.3: Definition of  $\theta_{p_i s_j}$  and  $\delta_{ij}$ .

By introducing Eq. (4.13) into Eq. (4.11) we have

$$2\pi\varepsilon_i = \sum_{j=1}^N \delta_{ij}\varepsilon_j + \sum_{j=1}^N \beta_{ij} + (\Gamma - \Gamma^n)\delta_{i\infty}, \tag{4.14}$$

with

$$\beta_{ij} = \int_{L_j} \frac{\psi_j(\boldsymbol{s}_j)(\boldsymbol{p}_i - \boldsymbol{s}_j) \cdot \boldsymbol{n}}{|\boldsymbol{p}_i - \boldsymbol{s}_j|^2} ds_j, \tag{4.15}$$

and

$$\delta_{i\infty} = \int_{S_W} \frac{(\boldsymbol{p}_i - \boldsymbol{\xi}_w) \cdot \boldsymbol{n}_w}{|\boldsymbol{p}_i - \boldsymbol{\xi}_w|^2} d\xi_w, \tag{4.16}$$

where  $\delta_{i\infty}$  is the angle subtended by the wake panel as viewed from  $p_i$ .

Finally, we can use the Kutta condition to express the circulation in terms of the velocity potential at the trailing edge:

$$\Gamma = \Phi(\boldsymbol{x}_{N}^{F}) - \Phi(\boldsymbol{x}_{1}^{I}), \tag{4.17a}$$

$$\Gamma^n = \Phi_N^n - \Phi_1^n, \tag{4.17b}$$

where  $x_N^F$  (the final point on the Nth panel) and  $x_1^I$  (the initial point on the first panel) should be thought of as tending to the trailing edge from above and below, respectively. Using Eqs. (4.17) in Eq. (4.14) gives

$$2\pi\varepsilon_{i} = \sum_{j=1}^{N} \delta_{ij}\varepsilon_{j} + \sum_{j=1}^{N} \beta_{ij} + [\Phi(\boldsymbol{x}_{N}^{F}) - \Phi_{N}^{n} - \Phi(\boldsymbol{x}_{1}^{I}) + \Phi_{1}^{n}]\delta_{i\infty} =$$

$$= \sum_{j=1}^{N} \delta_{ij}\varepsilon_{j} + \sum_{j=1}^{N} \beta_{ij} + [\varepsilon_{N} + \psi_{N}(\boldsymbol{x}_{N}^{F}) - \varepsilon_{1} - \psi_{1}(\boldsymbol{x}_{1}^{I})]\delta_{i\infty}. \tag{4.18}$$

Applying Eq. (4.18) to each of the N panels yields a linear system of equations for the "unknowns"  $\varepsilon_i$ . Eq. (4.18) can be expressed as a matrix equation,

$$\begin{pmatrix} \tilde{\delta}_{11} - \delta_{1\infty} & \delta_{12} & \delta_{13} & \cdots & \delta_{1N} + \delta_{1\infty} \\ \delta_{21} - \delta_{2\infty} & \tilde{\delta}_{22} & \delta_{23} & \cdots & \delta_{2N} + \delta_{2\infty} \\ \vdots & \vdots & \vdots & \vdots & \vdots \\ \delta_{N1} - \delta_{N\infty} & \delta_{N2} & \delta_{N3} & \cdots & \tilde{\delta}_{NN} + \delta_{N\infty} \end{pmatrix} \begin{pmatrix} \varepsilon_1 \\ \varepsilon_2 \\ \vdots \\ \varepsilon_N \end{pmatrix} = \begin{pmatrix} \beta_1 \\ \beta_2 \\ \vdots \\ \beta_N \end{pmatrix} + \Delta_{1N} \begin{pmatrix} \delta_{1\infty} \\ \delta_{2\infty} \\ \vdots \\ \delta_{N\infty} \end{pmatrix}$$
(4.19)

where  $\tilde{\delta}_{ii} = \delta_{ii} - 2\pi$ ,  $\beta_i = -\sum_{j=1}^N \beta_{ij}$  and  $\Delta_{1N} = \psi_1(\boldsymbol{x}_1^I) - \psi_N(\boldsymbol{x}_N^F)$ . Note that, for the coefficients  $\delta_{ij}$  and  $\delta_{i\infty}$  in Eq. (4.18), the integration path is irrelevant; they do not depend on the panel shapes, only on the endpoints of the panels. So, if there is any influence on the error magnitude of the panel shapes, it can only be through the coefficients  $\beta_i$  or  $\Delta_{1N}$ .

To estimate the error  $\varepsilon_i$  we need to estimate the right-hand side (RHS) of Eq. (4.19) and to establish that the  $N \times N$  matrix is invertible and that its eigenvalues are well-behaved (i.e., not too large or too small). In the next section we estimate the order of the RHS of Eq. (4.19) analytically. Then, in Sections 4.3.1, 4.3.2, 4.3.3 and 4.3.4 we analytically obtain the order of magnitude of the error for different body configurations and validate these against several numerical experiments.

### 4.2 Details of error estimate

We estimate here the size of the RHS of Eq. (4.19). First, recall that  $\beta_i = -\sum_{j=1}^N \beta_{ij}$ , where  $\beta_{ij}$  was defined in (4.15). By using the polar angle  $\theta_{p_i s_j}$ , defined in Eq. (4.12), we have

$$\beta_{ij} = \int_{L_j} \psi_j(\mathbf{s}_j) d\theta_{p_i s_j}, \tag{4.20}$$

where  $\psi_i$  is defined by Eq. (4.8) in the convex case and Eq. (4.10) in the concave case.

We first consider the convex case and focus on the second term in Eq. (4.8). We can use the mean value theorem, applied to each component of  $\nabla \Phi^n$ , to establish

$$\nabla \Phi^n(\mathbf{z}_i) = \nabla \Phi^n(\mathbf{x}_i) + O(l), \tag{4.21}$$

and may write

$$\nabla \Phi^{n}(\boldsymbol{x}_{i}) \cdot (\boldsymbol{p}_{i} - \boldsymbol{x}_{i}) =$$

$$= [\nabla \Phi^{n}(\boldsymbol{x}_{i}) \cdot \boldsymbol{t}_{i}][(\boldsymbol{p}_{i} - \boldsymbol{x}_{i}) \cdot \boldsymbol{t}_{i}] + [\nabla \Phi^{n}(\boldsymbol{x}_{i}) \cdot \boldsymbol{n}_{i}][(\boldsymbol{p}_{i} - \boldsymbol{x}_{i}) \cdot \boldsymbol{n}_{i}]. \quad (4.22)$$

In general, we have  $|\nabla \Phi^n(x_i)| = O(1)$ ,  $(p_i - x_i) \cdot n_i = O(l^2)$  and  $(p_i - x_i) \cdot t_i = O(l)$ , so we expect an O(l) contribution from this term in Eq. (4.8) unless  $(p_i - x_i) \cdot t_i = O(l)$ 

 $O(l^2)$ , i.e., unless the point of comparison  $p_i$  on the surface is taken to be "directly above" the collocation point  $x_i$ . We hereafter assume this to be the case, and write

$$\psi_i(\boldsymbol{s}_i) = \frac{\partial \Phi}{\partial s}(\boldsymbol{z}_s) \left[ s(\boldsymbol{s}_i) - s(\boldsymbol{p}_i) \right] + O(l^2). \tag{4.23}$$

Note that if we use curved panels this term could be  $O(l^2)$ .

The remaining term is O(l) but makes a contribution to  $\beta_{ij}$  of lower order if the collocation points are taken to be the midpoints of the panels  $\ell_i$ , as they usually are. To prove this we appeal to the mean value theorem to write

$$\frac{\partial \Phi}{\partial s}(\boldsymbol{z}_s) = \frac{\partial \Phi}{\partial s}(\boldsymbol{p}_i) + \nabla \frac{\partial \Phi}{\partial s}(\tilde{\boldsymbol{z}}_s) \cdot [s(\boldsymbol{z}_s) - s(\boldsymbol{p}_i)] = \frac{\partial \Phi}{\partial s}(\boldsymbol{p}_i) + O(l), \tag{4.24}$$

where  $\tilde{z}_s$  is a point on the surface between  $p_i$  and  $z_s$ . Thus

$$\psi_{i}(\mathbf{s}_{i}) = \left[\frac{\partial \Phi}{\partial s}(\mathbf{p}_{i}) + O(l)\right] \left[\xi_{i}(\mathbf{s}_{i}) - \xi_{i}(\mathbf{p}_{i})\right] \left[1 + O(l^{2})\right] + O(l^{2}) =$$

$$= \frac{\partial \Phi}{\partial s}(\mathbf{p}_{i}) \left[\xi_{i}(\mathbf{s}_{i}) - \xi_{i}(\mathbf{x}_{i})\right] + O(l^{2}), \tag{4.25}$$

where we have made use of Eq. (C.3) and the fact that  $\xi_i(p_i) = \xi_i(x_i)$  if  $(p_i - x_i) \cdot t_i = 0$ . Note that if we use curved panels the estimate of the first term of the RHS would be the same.

Using Eq. (4.25), Eq. (4.20) simplifies to

$$\beta_{ij} = \frac{\partial \Phi}{\partial s}(\boldsymbol{p}_j) \int_{L_j} [\xi_j(\boldsymbol{s}_j) - \xi_j(\boldsymbol{x}_j)] d\theta_{p_i s_j} + O(l^3).$$
(4.26)

It remains to estimate the integral in Eq. (4.26), which is a matter of straightforward geometry. For  $i \neq j$ , using the definitions in Figure 4.4 we write  $\xi_j(s_j) - \xi_j(x_j) = l_1 + l_2$  and immediately conclude, since  $h(\xi_j) = O(l^2)$  (see Appendix C) that  $l_2 = O(l^2)$ . Then, we have

$$\xi_{j}(\boldsymbol{s}_{j}) - \xi_{j}(\boldsymbol{x}_{j}) = l_{1} + O(l^{2}) = -\rho \cos \bar{\theta} + \rho \frac{\sin \bar{\theta} \cos \theta}{\sin \theta} + O(l^{2}) =$$

$$= \frac{\rho \sin \theta}{\sin \theta} + O(l^{2}), \tag{4.27}$$

where we have dropped the subscripts for convenience. Then, if we use

$$\theta = \bar{\theta} + O(l),\tag{4.28}$$

we have

$$\xi_j(\mathbf{s}_j) - \xi_j(\mathbf{x}_j) = \frac{\rho}{\sin \bar{\theta}} (\bar{\theta} - \theta) + O(l^2). \tag{4.29}$$

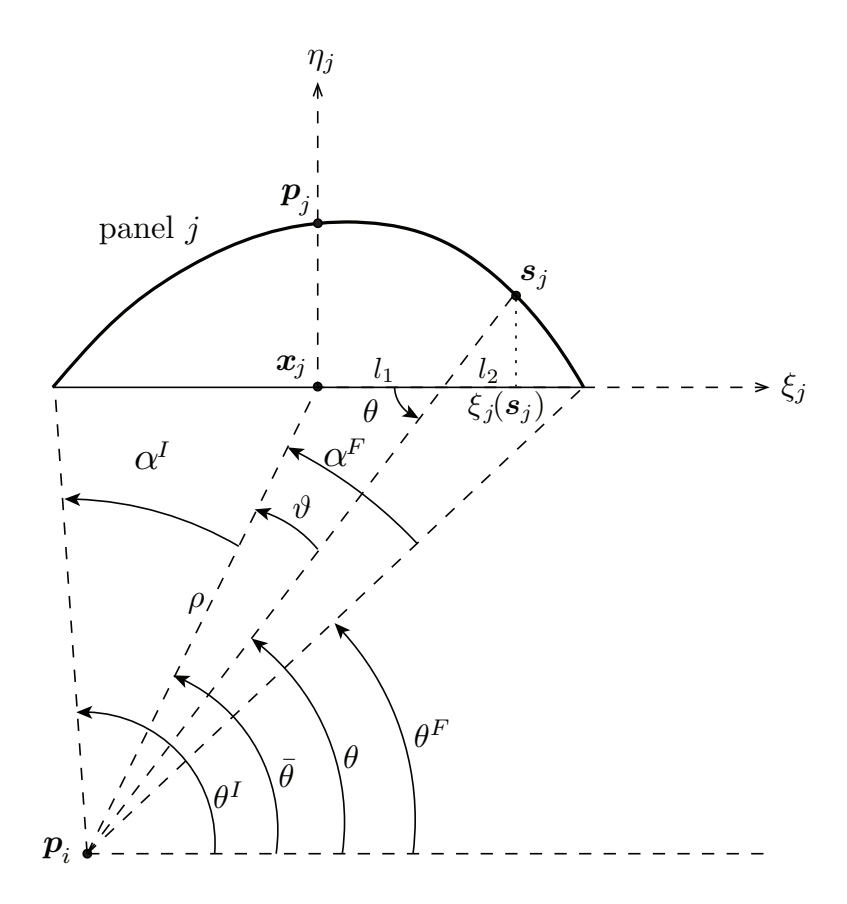


FIGURE 4.4: Definitions used in evaluating the integral in Eq. (4.26) in the convex case. For simplicity, we drop the subscripts on the angles here.

By using Eq. (4.29), the integral in Eq. (4.26) is easily evaluated,

$$\int_{\rho_I}^{\theta^F} \left[ \frac{\rho}{\sin \bar{\theta}} (\bar{\theta} - \theta) + O(l^2) \right] d\theta = \frac{\rho}{2 \sin \bar{\theta}} (\alpha^I - \alpha^F) (\alpha^I + \alpha^F) + O(l^3), \tag{4.30}$$

where we have defined the O(l) quantities  $\alpha^I = \theta^I - \bar{\theta}$  and  $\alpha^F = \bar{\theta} - \theta^F$ . Note that  $\alpha^I + \alpha^F = \delta_{ij}$  is the angle subtended by panel j as viewed from  $\boldsymbol{p}_i$  while  $\alpha^I - \alpha^F$  is

the difference between the angles subtended by the portions of  $\ell_j$  before and after (in a clockwise sense)  $x_j$ . In general this difference will be O(l) as well, but in the case where  $x_j$  is located at the center of the panel (total length  $l_j$ ) the leading order terms cancel. To see this we use

$$\frac{\sin(\bar{\theta} + \alpha^I)}{\rho} = \frac{2\sin\alpha^I}{l_i},\tag{4.31}$$

$$\frac{\sin(\bar{\theta} - \alpha^F)}{\rho} = \frac{2\sin\alpha^F}{l_j},\tag{4.32}$$

and expand in  $l_i$  to get,

$$\alpha^{I} = \frac{l_j}{2\rho} \sin \bar{\theta} \left(1 + \frac{l_j}{2\rho} \cos \bar{\theta}\right) + O(l^3), \tag{4.33}$$

$$\alpha^F = \frac{l_j}{2\rho} \sin \bar{\theta} (1 - \frac{l_j}{2\rho} \cos \bar{\theta}) + O(l^3). \tag{4.34}$$

It then follows that

$$\alpha^{I} - \alpha^{F} = \left(\frac{l_{j}}{2\rho}\right)^{2} \sin(2\bar{\theta}) + O(l^{3}), \tag{4.35}$$

and, returning to Eq. (4.26), that

$$\beta_{ij} = \frac{l_j^2 \delta_{ij} \cos \bar{\theta}}{4\rho} \frac{\partial \Phi}{\partial s}(\boldsymbol{p}_j) + O(l^3) = O(l^3). \tag{4.36}$$

For i=j, considering  $\boldsymbol{p}_i$  "directly above"  $\boldsymbol{x}_i$  we have:

$$\xi_j(\mathbf{s}_j) - \xi_j(\mathbf{x}_j) = \rho \cos \theta, \tag{4.37}$$

so the integral in Eq. (4.26) is,

$$\int_{\theta^I}^{\theta^F} \rho \cos \theta d\theta = \rho(\sin \theta^F - \sin \theta^I) = O(l^3). \tag{4.38}$$

In the concave case we have

$$\psi_i(\mathbf{s}_i) = \nabla \Phi(\mathbf{z}_s) \cdot (\mathbf{s}_i - \mathbf{x}_i). \tag{4.39}$$

We again make use of the mean value theorem, and write

$$\nabla \Phi(\boldsymbol{z}_s) = \nabla \Phi(\boldsymbol{s}_i) + O(l) = \frac{\partial \Phi}{\partial s}(\boldsymbol{s}_i)\boldsymbol{t} + O(l), \tag{4.40}$$

and also

$$\frac{\partial \Phi}{\partial s}(\boldsymbol{s}_i) = \frac{\partial \Phi}{\partial s}(\boldsymbol{x}_i) + \nabla \frac{\partial \Phi}{\partial s}(\hat{\boldsymbol{z}}_s) \cdot (\boldsymbol{s}_i - \boldsymbol{x}_i) = \frac{\partial \Phi}{\partial s}(\boldsymbol{x}_i) + O(l), \tag{4.41}$$

where  $\hat{z}_s$  is a point between  $s_i$  and  $x_i$ . Together Eqs. (4.40), (4.41), and (C.2) imply

$$\psi_{i}(\mathbf{s}) = \left[\frac{\partial \Phi}{\partial s}(\mathbf{x}_{i})\mathbf{t}_{i} + O(l)\right] \cdot (\mathbf{s}_{i} - \mathbf{x}_{i})$$

$$= \frac{\partial \Phi}{\partial s}(\mathbf{p}_{i})\left[\xi_{i}(\mathbf{s}_{i}) - \xi_{i}(\mathbf{x}_{i})\right] + O(l^{2}),$$
(4.42)

where we have used  $p_i = x_i$  to conform with Eq. (4.25). The expression for  $\beta_{ij}$ , which is again given by Eq. (4.26), is obtained much as before. The geometric situation in the concave case for  $i \neq j$  is depicted in Figure 4.5. We write  $\xi_i(s_i) - \xi_i(x_i) = l_1 - l_2$  and observe that  $l_2 = O(l^2)$ , as before. We have

$$l_1 = \frac{\rho \sin \vartheta}{\sin \theta},\tag{4.43}$$

and thus

$$\xi_i(\boldsymbol{s}_i) - \xi_i(\boldsymbol{x}_i) = \frac{\rho \sin \vartheta}{\sin \theta} + O(l^2) = \frac{\rho}{\sin \bar{\theta}} (\bar{\theta} - \theta) + O(l^2). \tag{4.44}$$

The remaining steps in estimating the integral in Eq. (4.26) are exactly as in the convex case, the result being Eq. (4.36).

Thus, under the assumptions that the collocation points  $x_i$  are located at the center of the panels and that the points of (error) comparison  $p_i$  are taken to be directly outside of (or, in the concave case, coincident with) the  $x_i$ , such that  $(p_i -$ 

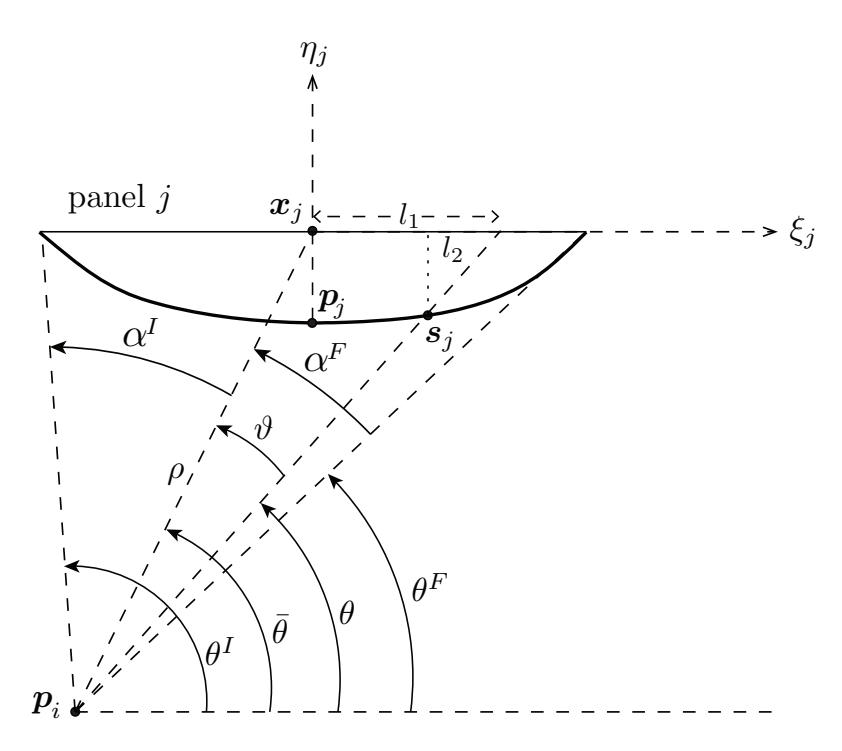


FIGURE 4.5: Definitions used in evaluating the integral in Eq. (4.26) in the concave case.

 $\mathbf{x}_i) \cdot \mathbf{t}_i = O(l^2)$ , we have  $\beta_{ij} = O(l^3)$ . This implies, since  $l = O(N^{-1})$ , that  $\beta_i = -\sum_{j=1}^N \beta_{ij} = O(l^2)$ . Note that the use of curved panels would not affect the order of  $\beta_i$ .

It only remains to show that the second term on the RHS of Eq. (4.19), which is proportional to  $\Delta_{1N}=\psi_1(\boldsymbol{x}_1^I)-\psi_N(\boldsymbol{x}_N^F)$  is not larger. In the case of a body whose upper and lower surfaces meet with a finite angle at the trailing edge, we know from continuity of the fluid velocity that the trailing edge is a stagnation point. We thus expect  $\frac{\partial \Phi}{\partial s}(\boldsymbol{p}_i)=O(l), i=1,N$ , which implies via Eqs. (4.25) and (4.42) that  $\psi_1(\boldsymbol{x}_1^I)$  and  $\psi_N(\boldsymbol{x}_N^F)$  are both  $O(l^2)$ , the same as  $\beta_i$ . If the upper and lower surfaces are tangent at the trailing edge (i.e., there is a cusp) then we have  $\frac{\partial \Phi}{\partial s}(\boldsymbol{p}_1)=-\frac{\partial \Phi}{\partial s}(\boldsymbol{p}_N)+O(l)$ , i.e., the velocities are (nearly) equal while the sense of ds is opposite. This means, assuming that  $\ell_N=\ell_1+O(l^2)$ , that

$$\Delta_{1N} = \psi_1(\boldsymbol{x}_1^I) - \psi_N(\boldsymbol{x}_N^F) 
= \left[ -\frac{l_1}{2} \frac{\partial \Phi}{\partial s}(\boldsymbol{p}_1) + O(l^2) \right] - \left[ \frac{l_1}{2} \frac{\partial \Phi}{\partial s}(\boldsymbol{p}_N) + O(l^2) \right] 
= -\frac{l_1}{2} \left[ \frac{\partial \Phi}{\partial s}(\boldsymbol{p}_1) + \frac{\partial \Phi}{\partial s}(\boldsymbol{p}_N) \right] + O(l^2) = O(l^2).$$
(4.45)

Thus the second term on the RHS of Eq. (4.19) is, like  $\beta_i$ ,  $O(l^2)$ .

### 4.2.1 Details of error estimate for sharp trailing edge

In Figure 4.6 a sketch of the panels near the trailing edge is shown.

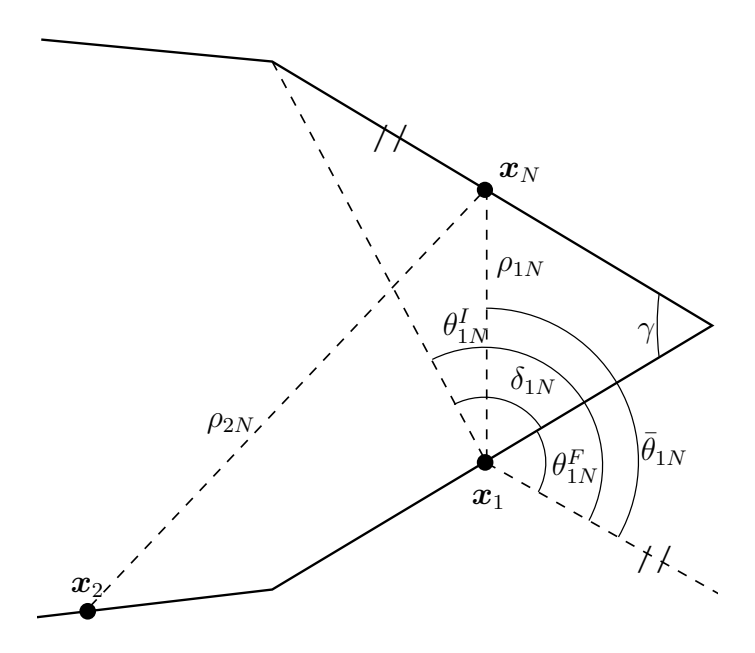


FIGURE 4.6: Sketch of trailing edge in a sharp body.

In this case, for the panels near the trailing edge, we cannot use the approximation of Eq. (4.28). To estimate the leading term of the integral in Eq. (4.26) we use Eq. (4.27), obtaining:

$$\int_{\theta^{I}}^{\theta^{F}} \left[ -\rho \cos \bar{\theta} + \frac{\rho \sin \bar{\theta} \cos \theta}{\sin \theta} \right] d\theta =$$

$$= -\rho \cos \bar{\theta} (\theta^{F} - \theta^{I}) + \rho \sin \bar{\theta} \left( \log|\sin \theta^{F}| - \log|\sin \theta^{I}| \right). \quad (4.46)$$

For i = 1, j = N we have

$$\rho = l\sin(\gamma/2), \quad \bar{\theta}_{1N} = \frac{\pi + \gamma}{2}, \quad \theta_{1N}^F = \gamma, \quad \theta_{1N}^I = \delta_{1N} + \gamma, \tag{4.47}$$

Dirichlet Formulation

with

$$\cos \delta_{1N} = \frac{4\sin^2(\gamma/2) - 1}{\sqrt{1 + 8\sin^2(\gamma/2)}}.$$
(4.48)

Note that when  $\gamma$  tends to  $\pi$  then  $\delta_{1N}$  tends to zero, and when  $\gamma$  tends to zero  $\delta_{1N}$  tends to  $\pi$ . The integral in Eq. (4.46) for panels 1 and N is then

$$\int_{\theta^{I}}^{\theta^{F}} \left[ \rho \cos \bar{\theta} + \frac{\rho \sin \bar{\theta} \cos \theta}{\sin \theta} \right] d\theta = 
= l \sin \left( \frac{\gamma}{2} \right) \left[ \delta_{1N} \cos \left( \frac{\pi + \gamma}{2} \right) + \sin \left( \frac{\pi + \gamma}{2} \right) \log \left| \frac{\sin \gamma}{\sin(\gamma + \delta_{1N})} \right| \right].$$
(4.49)

Thus, not only for panels 1 and N, but also for other panels near the trailing edge, the integral is not  $O(l^3)$  as obtained in (4.38), but O(l). However, as this occurs only for the panels near the trailing edge,  $\partial \Phi(\boldsymbol{p}_j)/\partial s \simeq O(l)$ , so we have  $\beta_{ij} \simeq O(l^2)$  for these panels (see Eq. (4.26)) and  $\beta_{ij} \simeq O(l^3)$  for panels sufficiently far from the trailing edge. Depending on the shape of the profile, the order of  $\beta_i = -\sum_{j=1}^N \beta_{ij}$  is  $O(l^p)$  with  $p \in [1,2]$ .

### 4.3 Results and Discussions

In this section the errors  $\varepsilon_i$  are estimated analytically for bodies with and without sharp corners and with concave or convex parts. In order to validate the theoretical results several numerical experiments are performed for which an accurate analytical solution is known. A comparison of the numerical and analytical solutions determines the true numerical error and we check whether this result agrees with the theoretical prediction.

For all numerical experiments described in this section, the wake is oriented parallel to the x axis, and the angle of attack  $\alpha$  is defined as the angle between this axis and the incident flow, which is given in each case. The modulus of the far field velocity is set to unity:  $U_{\infty}$ =1.

### 4.3.1 Numerical error results for thick bodies without sharp corners

Eq. (C.5) in Appendix C shows that  $\delta_{ii}=\pi+O(l)$ , so  $\tilde{\delta}_{ii}=-\pi+O(l)$  and  $\delta_{ij}$ , with  $i\neq j,\infty$ , is O(l) or smaller for these bodies. Moreover we have  $\delta_{1\infty}=-\delta_{N\infty}=\pi/2+O(l)$  and  $\delta_{1N}=\delta_{N1}=O(l)$ , so the  $N\times N$  matrix in Eq. (4.19) can be expressed as

$$\begin{pmatrix}
-3\pi/2 + O(l) & O(l) & O(l) & \cdots & \pi/2 + O(l) \\
-\delta_{2\infty} + O(l) & -\pi & O(l) & \cdots & \delta_{2\infty} + O(l) \\
\vdots & \vdots & \vdots & \vdots & \vdots \\
\pi/2 + O(l) & O(l) & O(l) & \cdots & -3\pi/2 + O(l)
\end{pmatrix}.$$
(4.50)

The matrix is, therefore, well-behaved since the off-diagonal terms are O(l) or smaller except for the first and the last column while the diagonal entries are, in general, close to  $-\pi$ . We thus expect the errors  $\varepsilon_i$  to be of the same order as the RHS. Section 4.2 shows the RHS of Eq. (4.19) to be  $O(l^2)$  provided two conditions hold:

- i The collocation points  $x_i$  are located at the center of the panels  $\ell_i$ .
- ii The points of comparison  $p_i$  are located "directly above" (or coincident with, in the concave case) the  $x_i$  such that  $t_i \cdot (p_i x_i) = O(l^2)$  where  $t_i$  is a unit vector tangent to panel i.

If either of these conditions is violated the error is O(l).

To confirm these results we obtain the numerical error in known cases, beginning with the flow around a thick ellipse with major axis of length 5 and minor axis of length 3; see Figure 4.7.

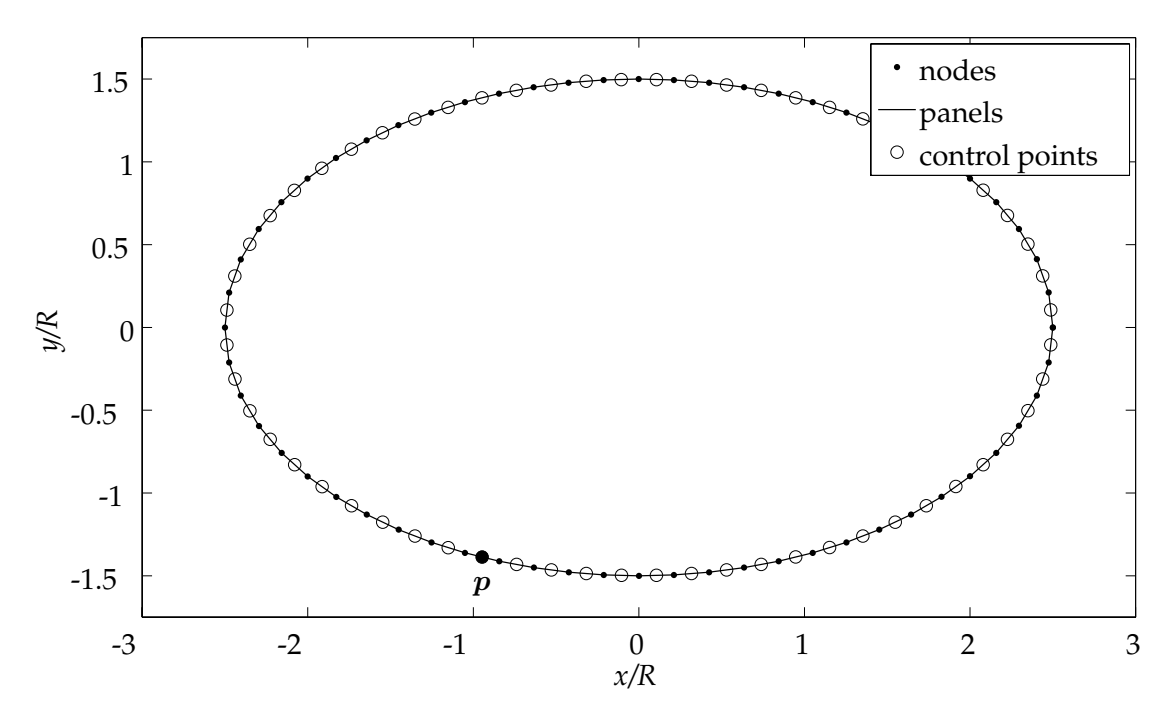


FIGURE 4.7: Ellipse with axis length 5 and 3.

The ellipse and the analytical expression for the velocity potential around it have been obtained from a Joukowski transformation:

$$\sigma = t + \frac{a^2}{t},\tag{4.51}$$

of a circle centered at  $(x_0, y_0) = (0, 0)$  with radius R = 2 and a = 1. In Eq. (4.51) t is a complex variable in the original domain (circle plane),  $\sigma$  is a complex variable in the transformed space and a is a constant. Since the complex potential around a circle has the analytical expression,

$$g(t) = U_{\infty}(t - t_0) \exp(-i\alpha) + U_{\infty} \frac{R^2}{t - t_0} \exp(i\alpha) + \frac{i\Gamma}{2\pi} \log(t - t_0), \tag{4.52}$$

with  $t_0 = x_0 + iy_0$ , we can express (see Katz and Plotkin, 2001) the complex potential around the body in the transformed space as  $g(t(\sigma))$ ; the velocity potential  $\Phi$  is the real part of  $g(t(\sigma))$ .

Figure 4.8 shows the numerical error obtained with this body by comparing the analytical and numerical solutions with  $\alpha=2^{\rm o}$ . This is calculated as a function of the number of panels, with the collocation points placed at the center of

the panels, and at a point p placed (see Figure 4.7) at (x,y) = (-0.947, -1.388). A (base 10) logarithmic scale has been used on both axis to show the order of the error. This figure shows that the numerical error is  $O(1/N^2)$  when the collocation points are placed at the center of the panels, as the theoretical analysis predicts. Similar results are found at other points of the body. This figure also shows the numerical error for this body when the collocation points are placed, instead, at the position  $l_i/3$ ; the order of the error in this case is O(1/N), as predicted by the theory. Hereafter, the numerical error will be calculated with the collocation points placed at the center of the panels.

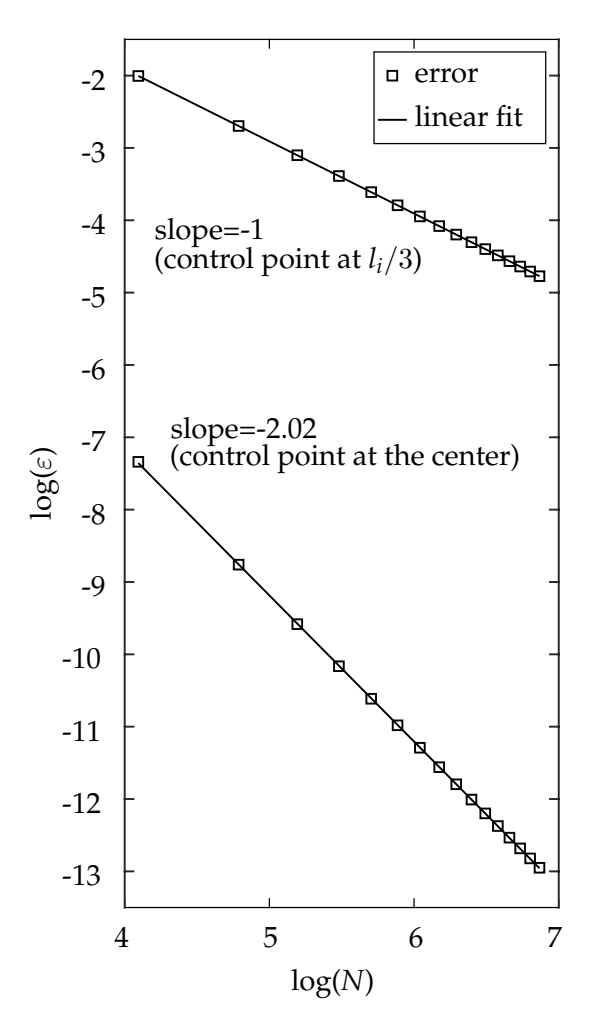


FIGURE 4.8: Comparison of the numerical error using the Dirichlet formulation for a thick ellipse with the collocation points placed at the center of the panels (lower curve) and at the position  $l_i/3$  (upper curve) for  $\alpha = 2^{\circ}$ .

To validate the theoretical results for bodies with both convex and concave parts, we calculate the numerical error for the body of Figure 4.9. The body and

the analytical solution for the potential velocity around it have been obtained from a Joukowski transformation with a=1 of a circle with radius R=2 centered at  $(x_0,y_0)=(0,1)$ .

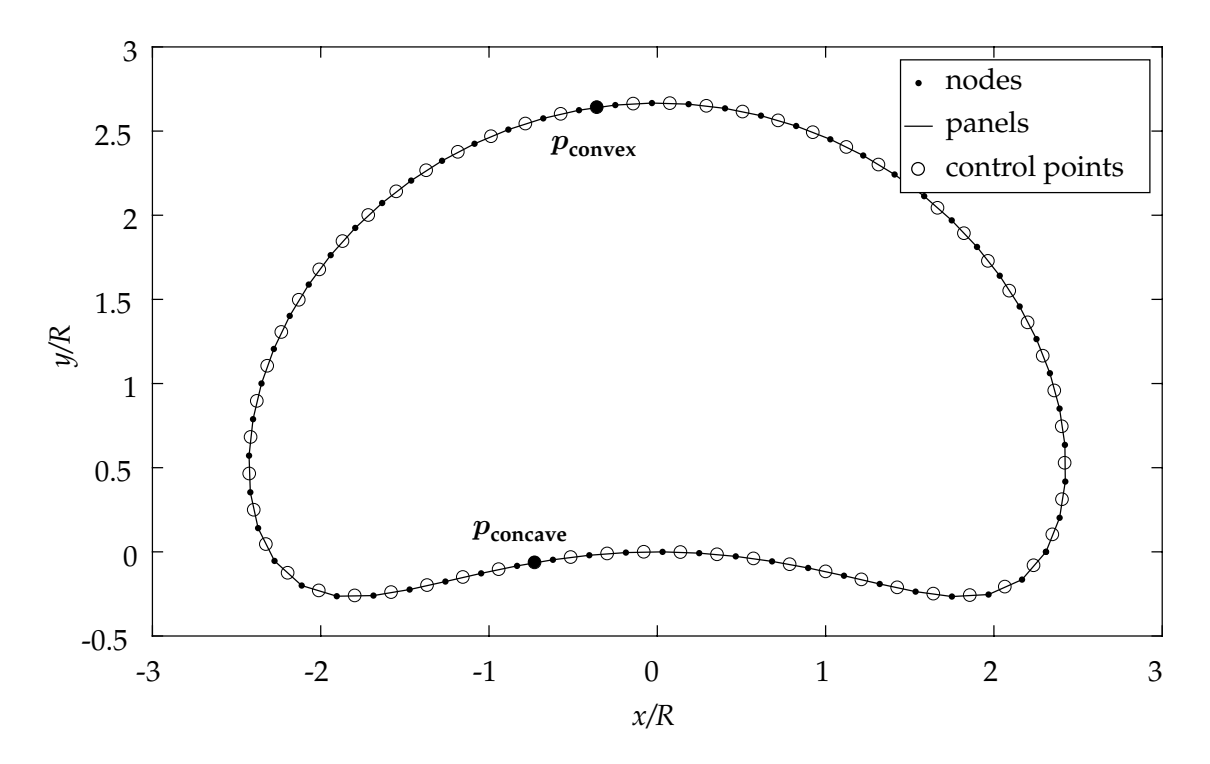


FIGURE 4.9: Nonsymmetric body with concave and convex parts

Figure 4.10 shows the numerical error at two points placed at (x,y)=(-0.358,2.643) (on the convex part of the profile) and (x,y)=(-0.727,-0.0653) (the concave part of the profile) for  $\alpha=2^{\rm o}$  as a function of the number of panels. Even though it is not distinguishable due to the scale of Figure 4.9, the point in the concave part is placed directly on the panel, while the point in the convex part is placed on the body surface, "directly above" the collocation point of the corresponding panel. This figure shows that the numerical error is  $O(1/N^2)$  for both points, which is as the theoretical analysis predicts. Similar results are found at other points of the body.

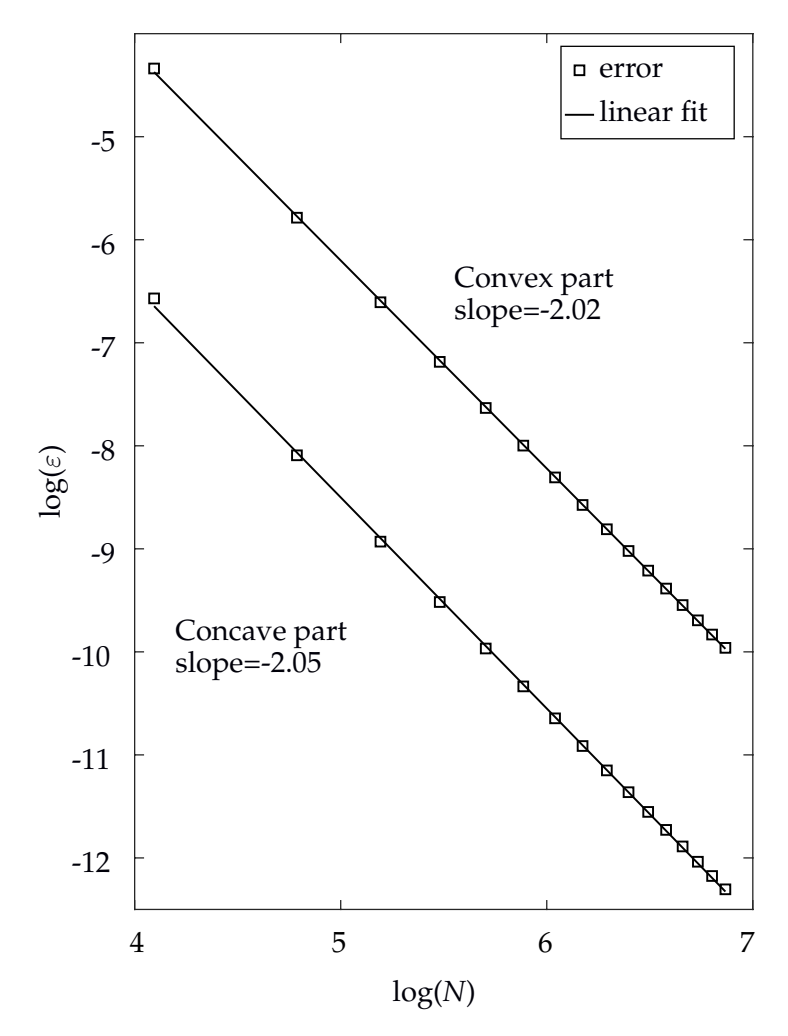


FIGURE 4.10: Numerical error using the Dirichlet formulation for a non-symmetric body with concave and convex parts for  $\alpha=2^{\circ}$ .

# 4.3.2 Numerical error results for thin bodies without sharp corners

For these types of bodies (see, e.g., the ellipse of Figure 4.11, it is necessary to take  $l \ll h$ , with h being a characteristic thickness of the body, such as the length of the vertical axis for the ellipse in Figure 4.11, to avoid the following problems:

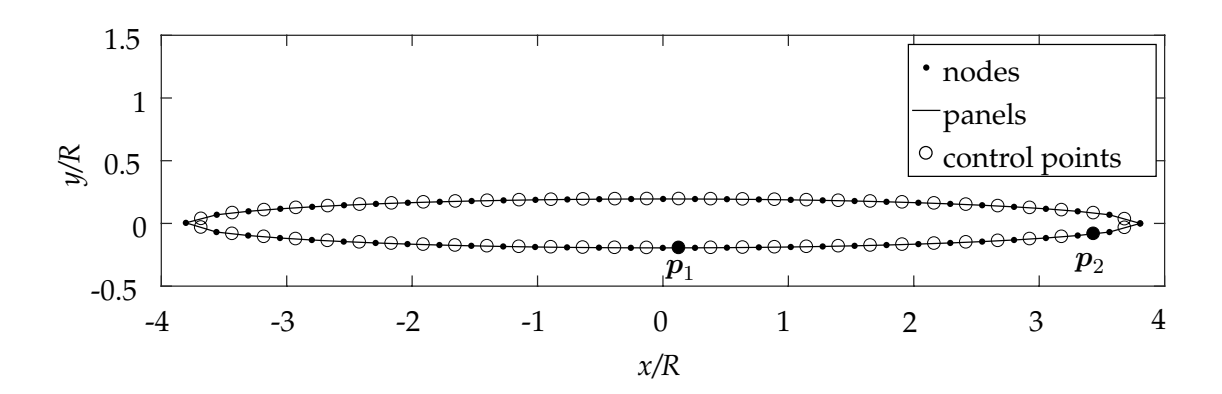


FIGURE 4.11: Thin ellipse

i The  $N \times N$  matrix could be close to singular. To illustrate this problem we suppose all panels are the same length. If  $h \ll l$  the  $N \times N$  matrix in Eq. (4.19) would be as follows for rows k and  $\bar{k} = N - k + 1$ , with panel k on the lower surface and  $\bar{k}$  on the upper surface, both sufficiently far from the leading and trailing edges:

$$\begin{pmatrix}
\tilde{\delta}_{11} - \delta_{1\infty} & \delta_{12} & \cdots & \delta_{1k} & \cdots & \delta_{1\bar{k}} & \cdots & \delta_{1N} + \delta_{1\infty} \\
\delta_{21} - \delta_{2\infty} & \tilde{\delta}_{22} & \cdots & \delta_{2k} & \cdots & \delta_{2\bar{k}} & \cdots & \delta_{2N} + \delta_{2\infty} \\
\vdots & \vdots \\
-\delta_{k\infty} + O(l) & O(l) & \cdots & -\pi + O(l) & \cdots & \pi + O(l) & \cdots & \delta_{k\infty} + O(l) \\
\vdots & \vdots \\
\delta_{k\infty} + O(l) & O(l) & \cdots & \pi + O(l) & \cdots & -\pi + O(l) & \cdots & -\delta_{k\infty} + O(l) \\
\vdots & \vdots \\
\delta_{N1} - \delta_{N\infty} & \delta_{N2} & \cdots & \delta_{Nk} & \cdots & \delta_{NN-k+1} & \cdots & \tilde{\delta}_{NN} + \delta_{N\infty}
\end{pmatrix}$$
(4.53)

Here we have used the fact that, if  $h \ll l$ , then  $\delta_{k\bar{k}} = \pi + O(l)$ ,  $\delta_{\bar{k}k} = \pi + O(l)$  and  $\delta_{\bar{k}\infty} = -\delta_{k\infty} + O(l)$ . The matrix eigenvalues could thus be ill-behaved.

ii Besides the problem above, when  $h \ll l$  the configuration of the panels near the trailing edge is as in Figure 4.12, which shows the trailing edge of the ellipse of Figure 4.11 in detail. In this case, the angle of the panels at the leading and trailing edges is not close to  $\pi$ , so the body would behave as if it had a sharp corner. In this situation we cannot use the approximation in

Eq. (4.28), and the order of  $\beta_i$  may not be  $O(l^2)$ , as explained in Section 4.2.1 and discussed in the next section.

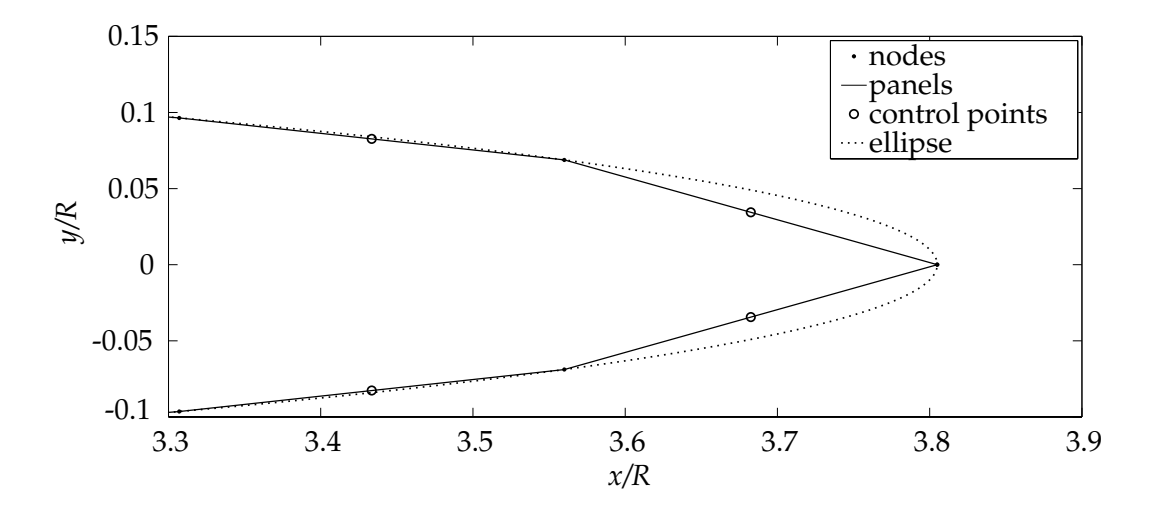


Figure 4.12: Detail of the panels near the trailing edge of a thin ellipse with  $h \ll l$ 

To validate the analytical results we calculate the numerical error for the ellipse of Figure 4.11, with major axis of length 7.61 and minor axis of length 0.39. The ellipse and the analytical solution for the velocity potential around it have been obtained from a Joukowski transformation with a=1.9 of a circle centered at  $(x_0,y_0)=(0,0)$  with radius R=2. Figure 4.13 shows the numerical error for  $\alpha=2^\circ$  at two points:  $p_1$ , at (x,y)=(0.127,-0.195) and  $p_2$ , at (x,y)=(3.439,-0.083) (near the trailing edge), as a function of the number of panels. This figure shows how the order of the numerical error decreases when the length of the panel decreases. It is  $O(1/N^2)$  when the length of the panel is sufficiently small compared to the length of the vertical axis of the ellipse, h.

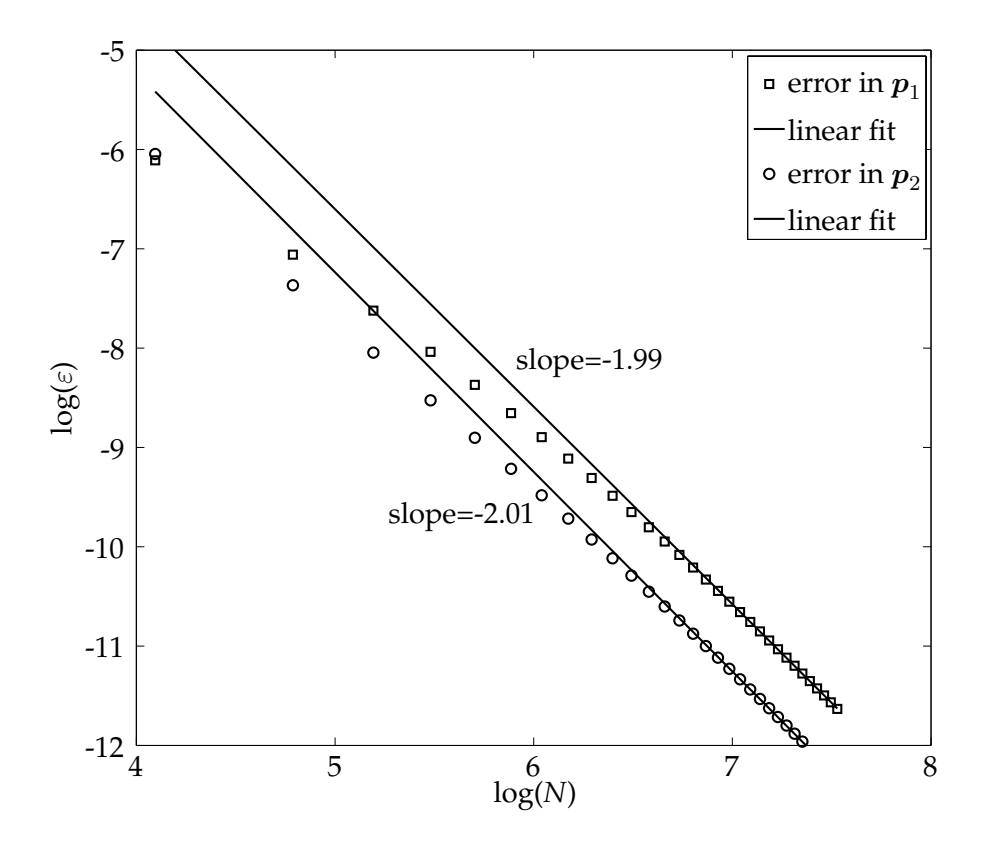


FIGURE 4.13: Numerical error using the Dirichlet formulation for a thin ellipse for  $\alpha=2^{\rm o}$ .

A comparison of this figure 4.13 with Figure 4.8 shows that the slope of the error curve changes in the case of the thin ellipse and remains nearly constant for the thick one.

Thus, if the length of the panels, which is O(1/N), is sufficiently small compared to the thickness of the body, the order of the error is  $O(1/N^2)$  with flat panels in both cases, including near the points of higher curvature, as the theoretical analysis predicts. In particular, the error is not O(1/N) for flat panels and  $O(1/N^2)$  for curved panels, as other authors suggest in their works (Bellamy-Knights et al., 1989). In the work by Vaz (Vaz, Eça, and Campos, 2003), it is found that thickness does not affect the order of magnitude of the error if the number of panels is large enough. However, in that reference, the authors do not give an analytical explanation for this fact but, instead, present calculations with different Karman-Treftz bodies, situations where the effect of the trailing edge angle may be more important than the effect of the thickness.

### 4.3.3 Numerical error results for bodies with sharp corners

For bodies of this type the order of  $\beta_i$  may not be  $O(l^2)$ , as explained in Section 4.2.1. From Eq. (4.19) and the approximation of the  $N \times N$  matrix in Eq. (4.50) we can obtain the leading order of the error for panels 1, N, and for a generic panel k:

$$i = 1: -\frac{3\pi}{2}\varepsilon_1 + \frac{\pi}{2}\varepsilon_N = \beta_1 + O(l^2); \tag{4.54}$$

$$i = k: -\delta_{k\infty}\varepsilon_1 - \pi\varepsilon_k + \delta_{k\infty}\varepsilon_N = \beta_k + O(l^2);$$
(4.55)

$$i = N: \frac{\pi}{2}\varepsilon_1 - \frac{3\pi}{2}\varepsilon_N = \beta_N + O(l^2); \tag{4.56}$$

so

$$\varepsilon_1 = -\frac{3\beta_1 + \beta_N}{4\pi} + O(l^2),\tag{4.57}$$

$$\varepsilon_N = -\frac{\beta_1 + 3\beta_N}{4\pi} + O(l^2),\tag{4.58}$$

$$\varepsilon_k \simeq \frac{1}{\pi} \left( \delta_{k\infty} \frac{\beta_1 - \beta_N}{2\pi} - \beta_k \right) + O(l^2).$$
(4.59)

If panel k is far enough from the trailing edge, the term  $\beta_k$  would be of order  $O(l^2)$ . However, the error is also influenced by the terms  $\beta_1$  and  $\beta_N$ , as we show in Section 4.2.1, for bodies with a sharp trailing edge; depending on the shape of the profile, they could be  $O(l^p)$  with  $p \in [1,2]$ . The numerical error could thus be  $O(1/N^p)$  with  $p \in [1,2]$  even though the point in question is far from the trailing edge.

To validate the analytical results we consider different bodies, both symmetric and asymmetric.

### 4.3.3.1 Symmetric bodies with sharp corners

Figure 4.14 shows several symmetric bodies obtained from a Karman-Trefft transformation:

$$\frac{\tau - k_T a}{\tau + k_T a} = \left(\frac{t - a}{t + a}\right)^{k_T},\tag{4.60}$$

with different values of  $k_T$ ; the constant a is given by:

$$(a - x_0)^2 = R^2 - y_0^2, (4.61)$$

with  $(x_0, y_0) = (-0.2, 0)$  and R = 1.

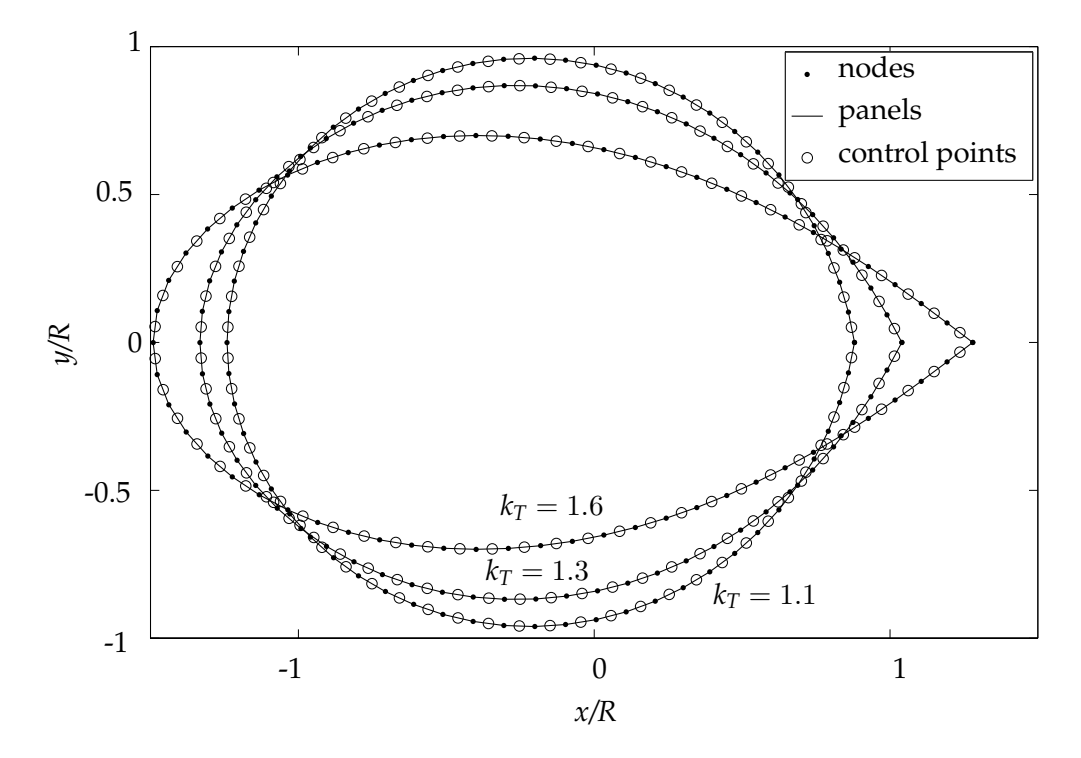


FIGURE 4.14: Symmetric bodies with a sharp corner obtained from a Karman-Trefft transformation with  $k_T=1.1,1.3$  and 1.6.

Figure 4.15 shows the numerical error for  $\alpha=2^{\rm o}$  as a function of the number of panels. As this figure shows, the numerical error is  $O(1/N^p)$  with  $p\in[1,2]$ , and p decreases when  $k_T$  increases because the angle at the trailing edge,  $\gamma$ , decreases. Similar behaviour for the error is obtained with other panels.

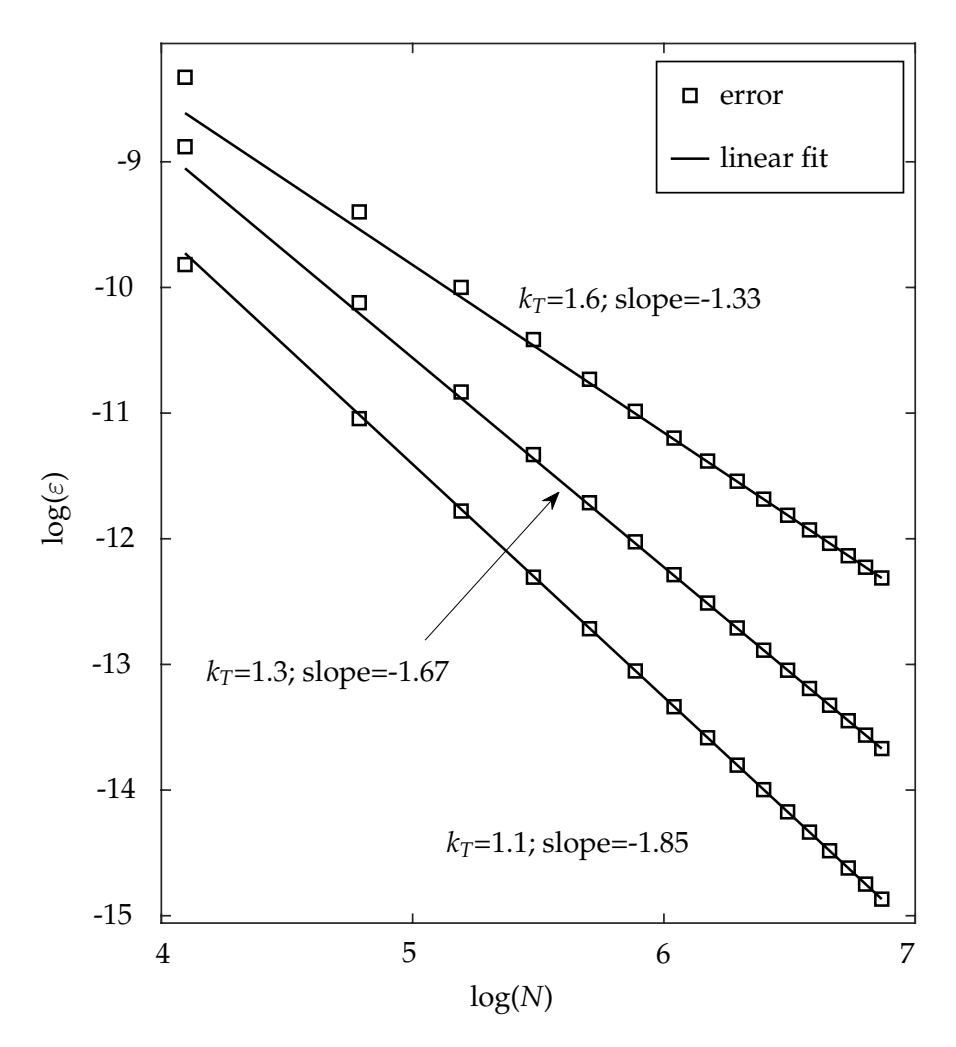


FIGURE 4.15: Numerical error using the Dirichlet formulation for symmetric bodies with sharp corners for  $\alpha=2^{\rm o}$ .

There is an exception for symmetric bodies when  $\alpha=0^o$ . In this particular case, with symmetric geometry and symmetric flow around the body we have  $\partial \Phi(\boldsymbol{p}_k)/\partial s = \partial \Phi(\boldsymbol{p}_{N-k+1})/\partial s$ . Since the integral in Eq. (4.26) depends only on geometry we conclude than  $\beta_k = \beta_{N-k+1}$  and, in particular,  $\beta_1 = \beta_N$ . In this case, from Eqs. (4.57), (4.58) and (4.59) we obtain:

$$\varepsilon_1 = \varepsilon_N \simeq -\frac{\beta_1}{\pi},$$
(4.62)

$$\varepsilon_k \simeq -\frac{\beta_k + \Delta_{1N}}{\pi},$$
 (4.63)

so, for panels far from the trailing edge, the error is  $O(1/N^2)$  as Figure 4.16 shows.

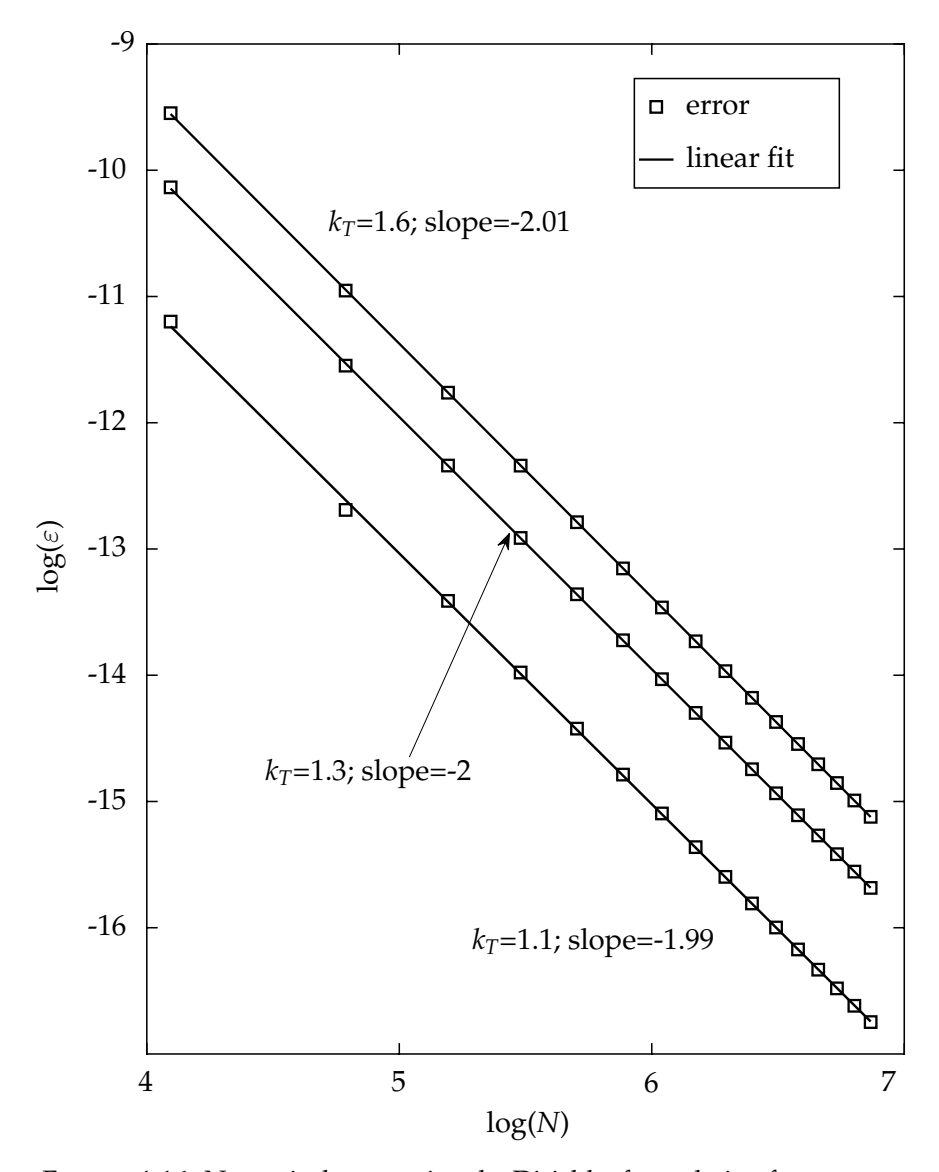


FIGURE 4.16: Numerical error using the Dirichlet formulation for symmetric bodies with sharp corners for  $\alpha=0^{\rm o}$ .

Figure 4.17 shows the numerical error for  $\alpha=10^{\rm o}$  as a function of the number of panels. By comparison of this figure with Figure 4.15, it can be stated that the error order estimation is valid also for longer angles of attack  $\alpha$ . For even longer angles of attack the results are very similar. The only exception occurs for  $\alpha=0^{\rm o}$  as predicted by the theory.

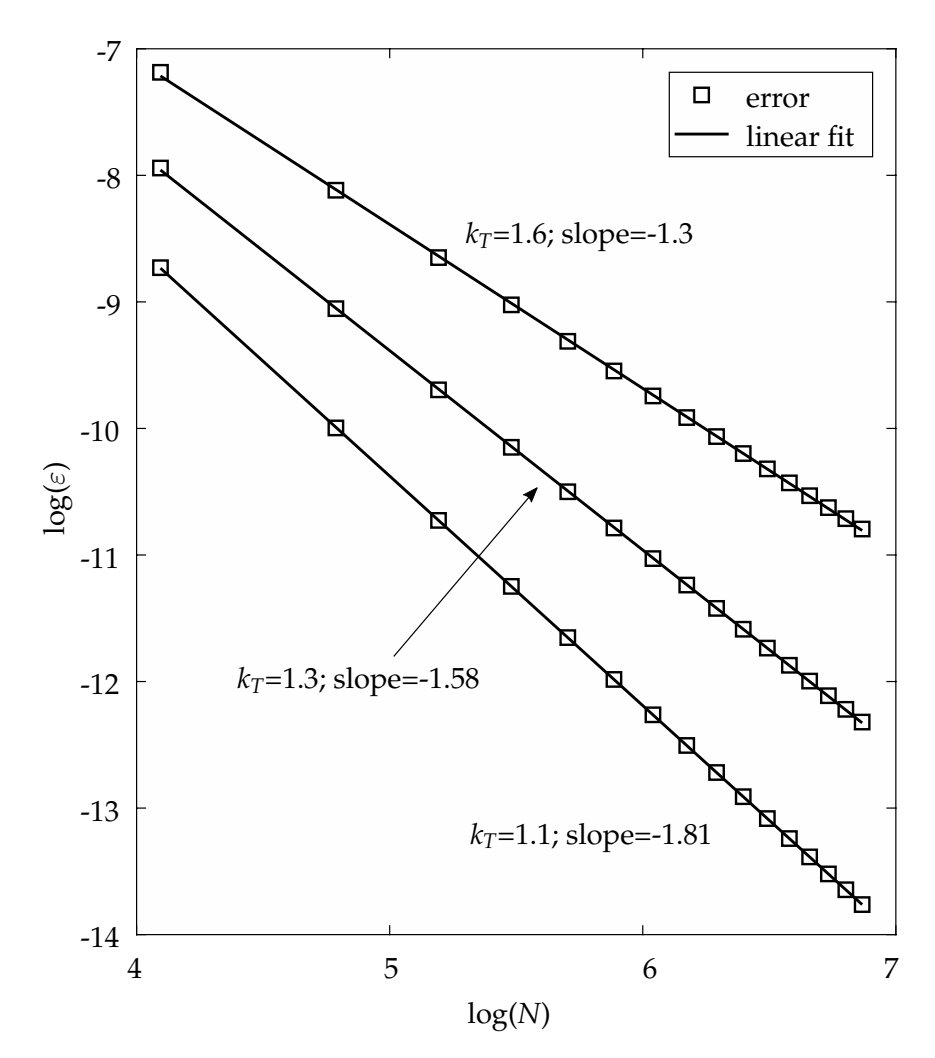


FIGURE 4.17: Numerical error using the Dirichlet formulation for symmetric bodies with sharp corners for  $\alpha=10^{\rm o}$ .

### 4.3.3.2 Asymmetric bodies with sharp corners

For asymmetric bodies the results are similar although, in this case, there is no significant difference between the order of the error for  $\alpha=0^o$  and for  $\alpha\neq0^o$  because symmetric configurations are excluded. Figure 4.18 shows asymmetric bodies obtained from a Karman-Trefft transformation with different values of  $k_T$  and  $(x_0,y_0)=(-0.2,0.3)$ , R=1, while Figure 4.19 shows the numerical error for  $\alpha=0^o$ . Results for  $\alpha=2^o$  are very similar, as illustrated in Figure 4.20.

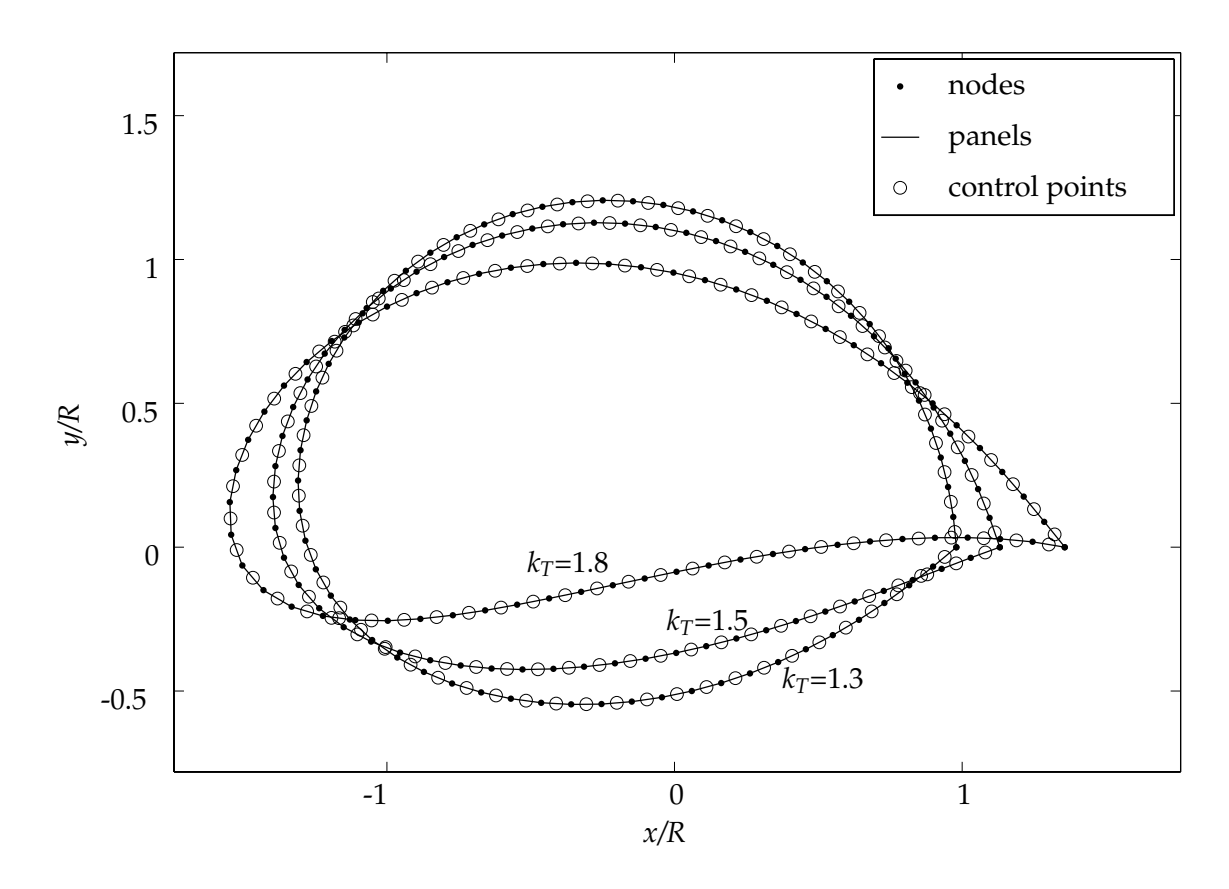


FIGURE 4.18: Asymmetric bodies with sharp corners obtained from a Karman-Trefft transformation with  $k_T=1.3,1.5$  and 1.8.

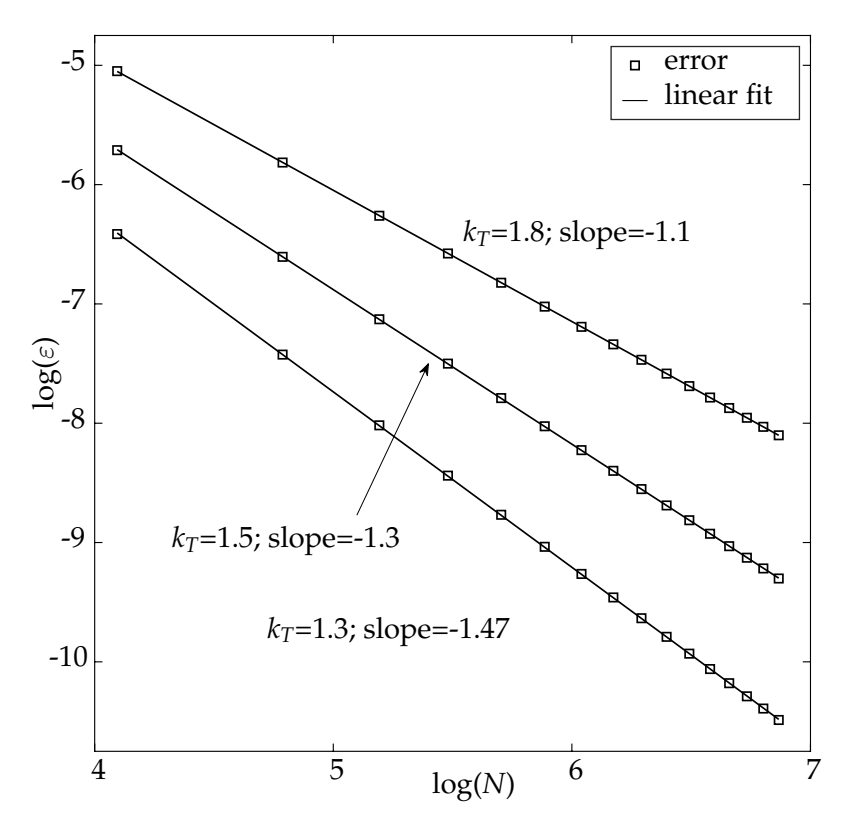


Figure 4.19: Numerical error using the Dirichlet formulation for asymmetric bodies with sharp corners for  $\alpha=0^{\rm o}$ .

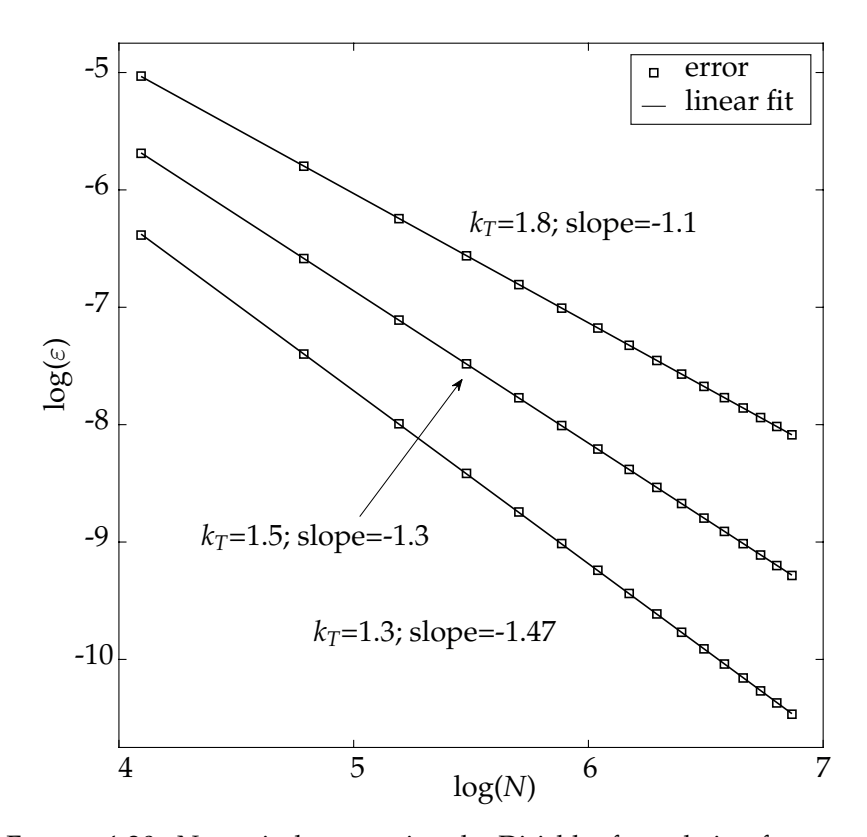


Figure 4.20: Numerical error using the Dirichlet formulation for asymmetric bodies with sharp corners for  $\alpha=2^{\rm o}$ .

Figure 4.21 shows the numerical error for  $\alpha=10^{\circ}$  as a function of the number of panels. Experiments for longer or negative angles of attack have not been included in this text for conciseness as the results are very similar to those already presented in these figures. From an analysis of the results obtained for different angles of attack, it can be stated that the error order behaves as predicted by the analytical developments even for this type of obstacles.

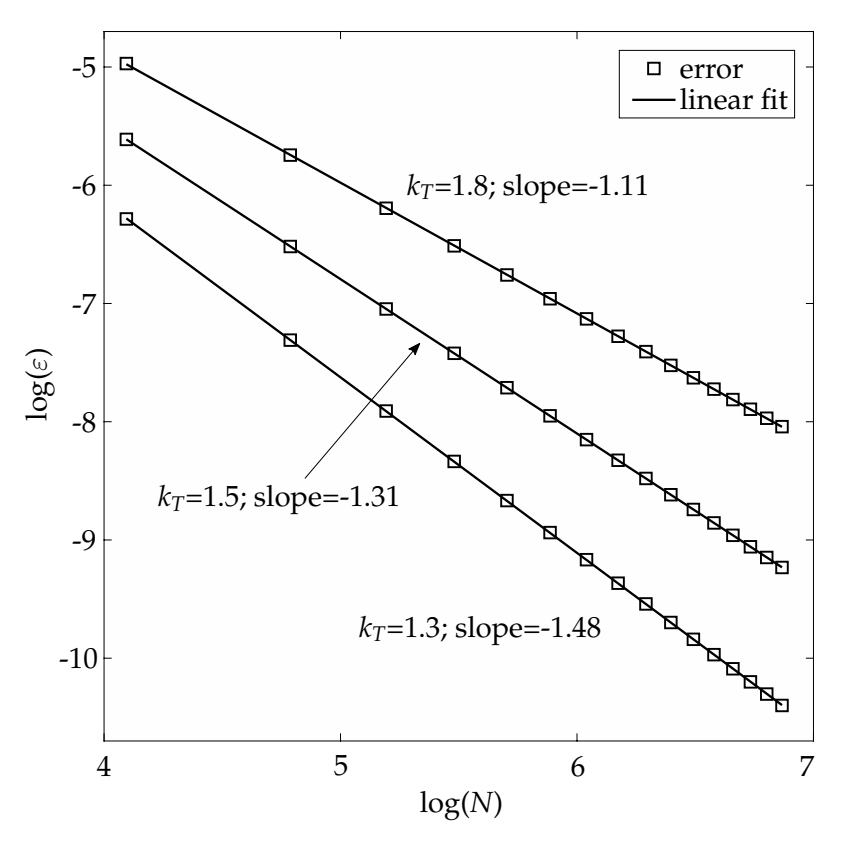


FIGURE 4.21: Numerical error using the Dirichlet formulation for asymmetric bodies with sharp corners for  $\alpha=10^{\rm o}$ .

Thus, the error is  $O(1/N^p)$  with  $p \in [1,2]$  and depends on the angle  $\gamma$  at the sharp corner. Figures 4.22 and 4.23 show the evolution of p with  $\gamma$  and  $k_T$ , respectively, for different values of  $\alpha$  with symmetric bodies. When  $\gamma \to 180^\circ$  the error tends to  $O(1/N^2)$  and when  $\gamma \to 0^\circ$  the error tends to O(1/N). Note that the exponent p can take any value between 1 and 2; it is not required that p=1 or p=2, as several authors suggest (Oskam, 1986; Bellamy-Knights et al., 1989).

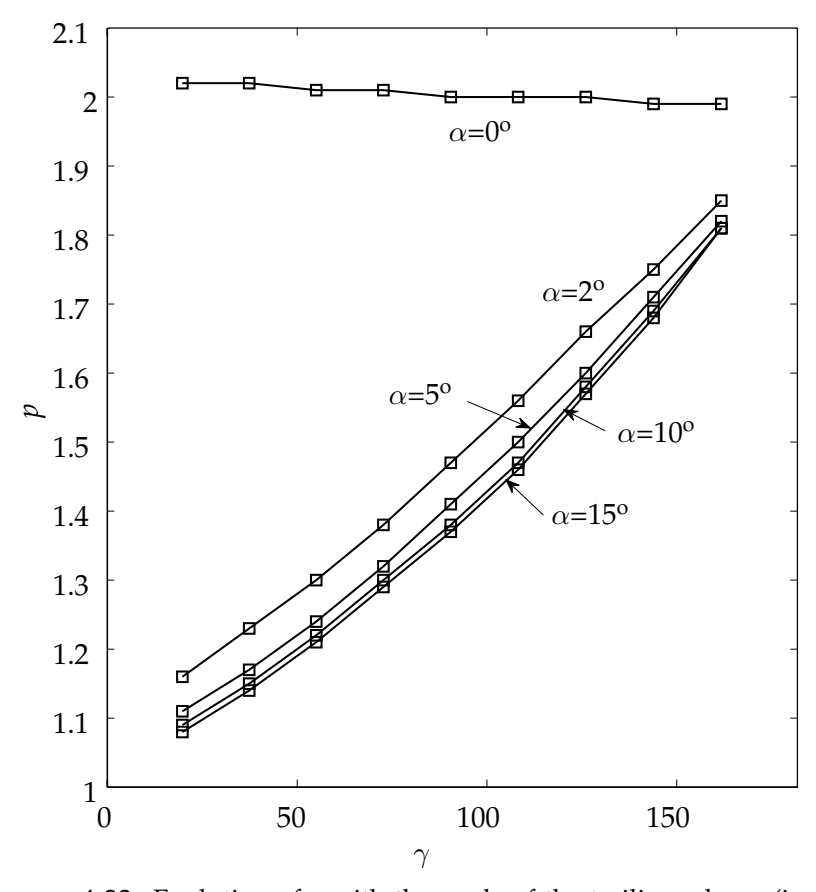


Figure 4.22: Evolution of p with the angle of the trailing edge  $\gamma$  (in degrees) for different  $\alpha.$ 

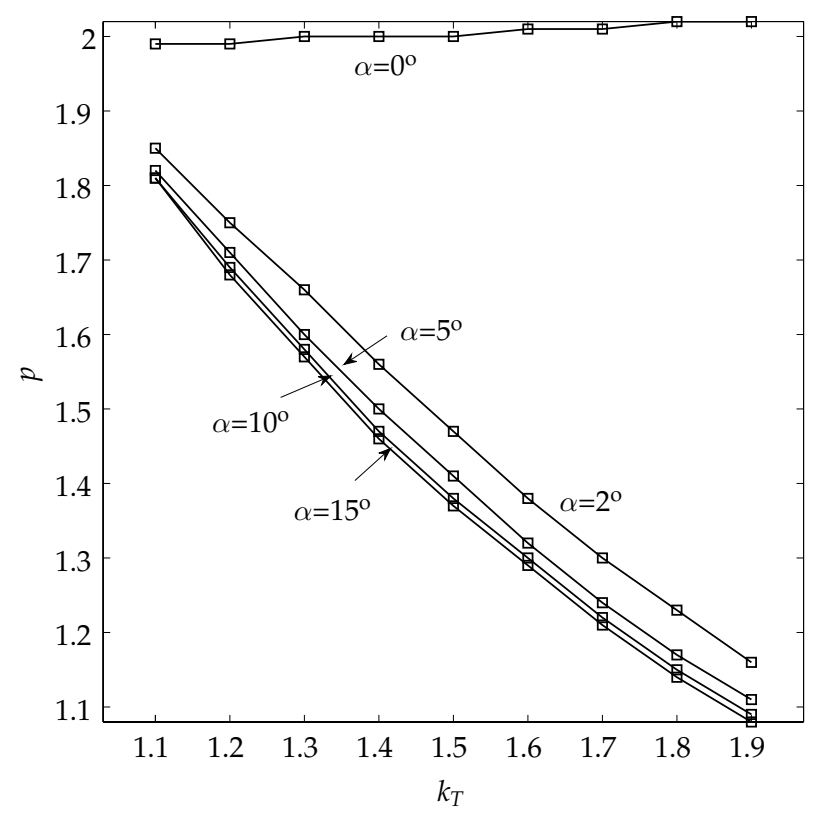


Figure 4.23: Evolution of p with  $k_T$  for different  $\alpha$ .

In the work by Kinnas and Hsin (Kinnas and Hsin, 1994), the error for panels near the trailing edge was also analyzed, and it was found that panels placed on the same side contribute an  $O(l^2)$  amount to the error while panels on the opposite side contribute an O(l) amount. The authors associate this last error with the convergence of the method: O(1/N). However, we have shown here that panels placed on the same side contribute an  $O(l^3)$  amount to the error while those on the opposite side contribute an  $O(l^2)$  amount. Here we calculate the global error, considering the influence of all panels, the shape of the body, and the angle at the trailing edge, and find that the exponent p can take any value between 1 and 2, as stated above.

In the article by Vaz (Vaz, Eça, and Campos, 2003), the authors obtain a numerical estimate of the error and find p=1.4 for a particular Karman-Trefft body; the asymptotic order of the accuracy, however, is higher than the theoretical one they obtain, probably because they perform a local error analysis, not a global error analysis as done here. The convergence of the panel method in problems with non-smooth boundaries is analyzed by Ye and Fei (Ye and Fei, 2009). The authors use polygons and analyze the convergence at the corners, and also find that the error at the corners is the main factor that reduces the overall convergence of the method.

### 4.3.4 Numerical error results for curved panels

Section 4.2 shows that the use of curved panels does not modify the order of  $\beta_i$  or  $\Delta_{1N}$ , so there is no benefit to using curved panels instead of flat panels. To validate this theoretical conclusion, we consider the thin ellipse of Figure 4.11. Figure 4.24 compares the numerical error for this ellipse when approximated by flat panels with that found using two types of curved panels. The curved panels are placed so that the collocation points are 1/3 or 2/3 of the distance between  $x_i$  and  $p_i$ . The figure shows that there is no difference in the order of the error when curved panels are used. This verifies that the curvature of the panels has no influence on the order of magnitude of the error, as suggested in the work by

4.4. Discussions 85

Ehlers (Ehlers et al., 1979) and by other authors, at least for the case analyzed here with a doublet distribution of constant strength along the panel. Generally, for methods using a constant strength singularity distribution, it does not reduce the order of the error to use more complex panel geometries by including, e.g., quadratic or cubic terms.

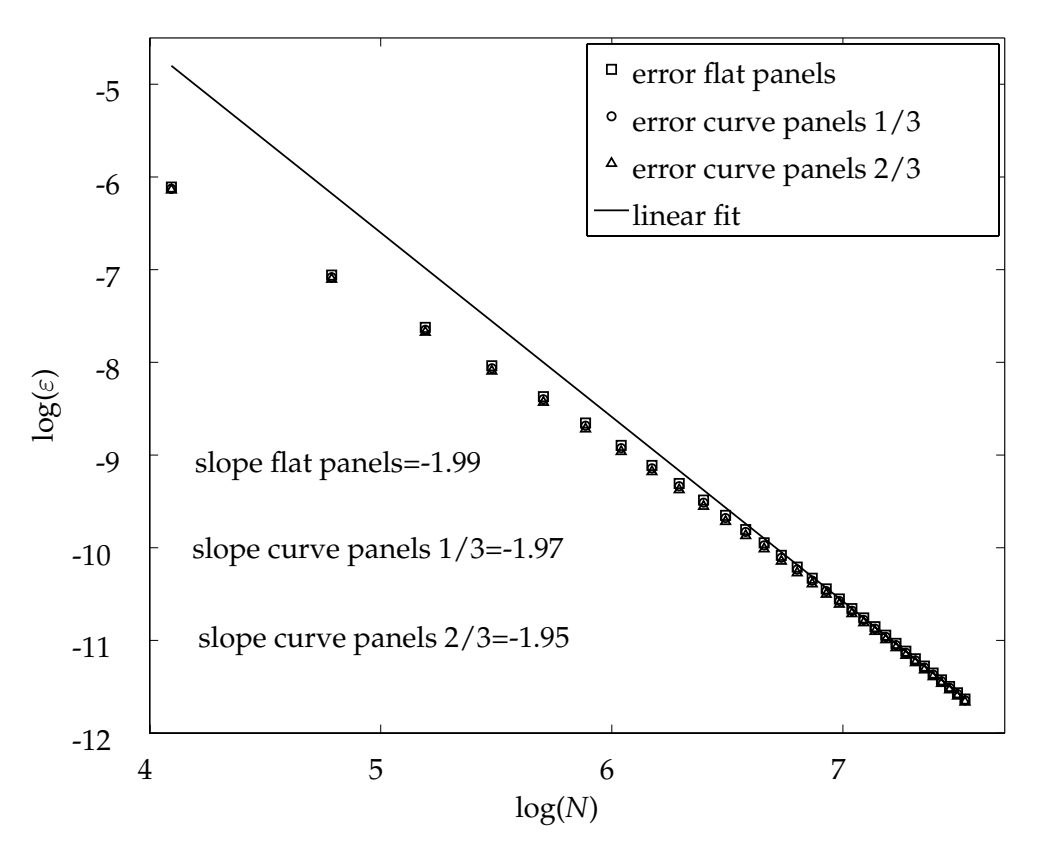


FIGURE 4.24: Comparison of numerical error for flat panels and curved panels. The results are so close that it is hard to distinguish them on the scale of the plot.

### 4.4 Discussions

In this chapter a formal analytical and numerical analysis of the asymptotic global error in panel methods using Dirichlet formulation and using flat panels is presented for thick bodies with the possibility of convex and concave portions. The analysis shows that there are several factors affecting the order of the error.

- (i) Regarding the geometry of the body, the main factor affecting the order of the error is the existence of sharp corners. If there are no sharp corners, the error is  $O(1/N^2)$ , even for flat panels and bodies with strong curvature, provided the length of the panels, which is O(1/N), is sufficiently small compared to the thickness of the body. If there are sharp corners, the error is  $O(1/N^p)$  with  $p \in [1,2]$ , and this factor depends on the angle  $\gamma$  at the sharp corner. When  $\gamma \to \pi$  the leading error tends to  $O(1/N^2)$  and when  $\gamma \to 0$  the leading error tends to O(1/N). The exponent p can take any value between 1 and 2, and not only those two particular values, as several authors suggest.
- (ii) To minimize error, the collocation points  $x_i$  should be located at the center of the panels  $\ell_i$ , and the points of comparison  $p_i$  should be located "directly above" the collocation points  $x_i$  in the convex case and coincident with  $x_i$  in the concave case. If this condition is violated the error is O(l/N).
- (iii) There is no difference in the order of the error for bodies with only convex parts compared to bodies with both convex and concave parts.
- (iv) Concerning the shape of the panels, the analysis shows that the use of curved panels rather than flat ones does not improve the order of the error.

# Chapter 5

# Global Error Analysis of Two-Dimensional Panel Methods for Neumann Formulation

The error order estimation when solving the Green's integral equation for thick bodies with Dirichlet boundary conditions was discussed in Chapter 4. A formal analytical estimation of the global error assumed when employing the Neumann formulation to solve the Green's integral equation for thick bodies is then the logical step forward in this dissertation. The solution of this system of equations allows to obtain the differences of velocity potential values in a discretized domain derived from an obstacle embedded in a fluid domain.

The resolution of the problem introduced in Section 2.1 with the Neumann boundary conditions (see Section 2.2.2) does not provide velocity potentials but differences of velocity potentials; this impose the definition of the error as the gap between the analytical and the numerical differences of velocity potentials. In this chapter the formulation is simplified by introducing some geometric factors coming from the body discretization that result in a system of N-1 equations for the error calculation. Note here that some information is lost due to derivations; it is a N-1 system for a N number of panels obstacle discretization. This formulation is appropriate for developing a formal analytical estimation of the

global error when using Neumann boundary conditions; by estimating the order of each of the system elements the pursued result is obtained. The errors are proved to be of larger order than those obtained using the Dirichlet boundary conditions. The chapter is completed with the introduction of several numerical results that confirm the estimation correctness as long as the conditions required for its convergence are met.

## 5.1 Global error estimate for Neumann formulation

Equation (4.4), which determined the N velocity potentials  $\Phi_i^n$  in the Dirichlet formulation, can be further simplified by writing the geometric factors (the integrals) in terms of equivalent angles,

$$\Phi_{i}^{n} = \frac{1}{2\pi} \sum_{j=1}^{N} \Phi_{j}^{n} \int_{l_{j}} d\theta_{x_{i}\xi_{j}} - \frac{\Gamma^{n}}{2\pi} \theta_{x_{i}x_{N}}^{F} + \Phi_{\infty}(\boldsymbol{x}_{i}) = 
= \frac{1}{2\pi} \sum_{j=1}^{N} \Phi_{j}^{n} (\theta_{x_{i}x_{j}}^{F} - \theta_{x_{i}x_{j}}^{I}) - \frac{\Gamma^{n}}{2\pi} \theta_{x_{i}x_{N}}^{F} + \Phi_{\infty}(\boldsymbol{x}_{i}).$$
(5.1)

Here  $\theta_{x_i\xi_j}$  is the (polar) angle associated with the vector  $\boldsymbol{\xi}_j - \boldsymbol{x}_i$ , a function of the position  $\boldsymbol{\xi}_j$  along panel  $l_j$ . The limits of integration are  $\theta^I_{x_ix_j}$ , corresponding to the node  $\boldsymbol{x}_j^I$ , and  $\theta^F_{x_ix_j}$ , corresponding to the node  $\boldsymbol{x}_j^F$ ; these are illustrated in Figure 5.1.

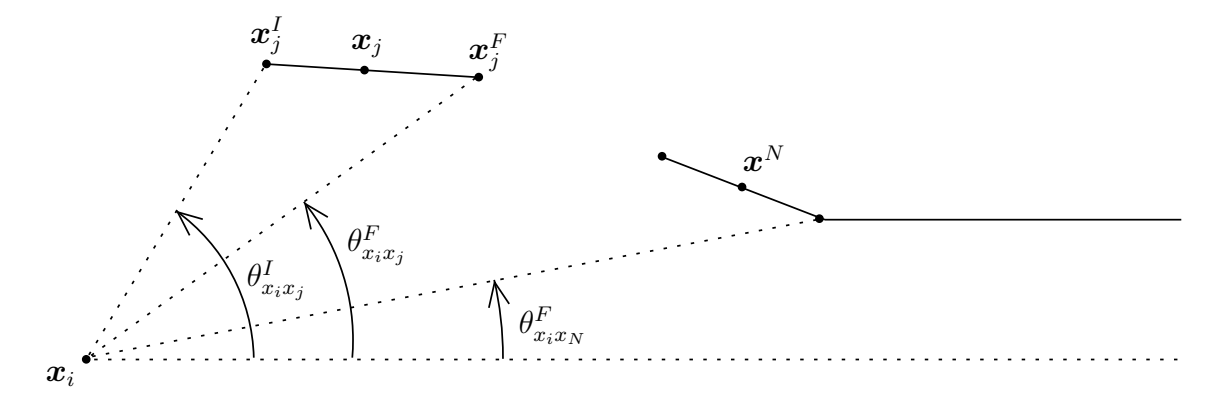


FIGURE 5.1: Definition of  $\theta_{x_i x_j}^I$  and  $\theta_{x_i x_j}^F$ .

Using the fact that  $\Gamma^n=\Phi^n_N-\Phi^n_1$ , along with  $\theta^F_{x_ix_{j-1}}=\theta^I_{x_ix_j}$  and defining

$$\Upsilon_i^n \equiv \Phi_i^n - \Phi_{i-1}^n \qquad \text{for } i = 2..N, \tag{5.2}$$

we can rearrange and simplify terms in Eq. (5.1) to get

$$\Phi_i^n = \frac{1}{2\pi} \sum_{j=2}^N \theta_{x_i x_j}^I (\Phi_{j-1}^n - \Phi_j^n) + \Phi_{\infty}(\boldsymbol{x}_i) = -\frac{1}{2\pi} \sum_{j=2}^N \theta_{x_i x_j}^I \Upsilon_j^n + \Phi_{\infty}(\boldsymbol{x}_i).$$
 (5.3)

The Neumann boundary condition then means that  $n_i \cdot \nabla_i \Phi^n(x_i) = 0$  or

$$\sum_{j=2}^{N} \theta_{x_i x_j}^{\prime I} \Upsilon_j^n = 2\pi V_{x_i \infty}^{\perp}, \tag{5.4}$$

where  $V_{i\infty}^{\perp}$  is the component of  $V_{\infty}$  normal to panel i at  $\boldsymbol{x}_i$ , and  $\theta'^I_{x_ix_j}$  is the normal component of the gradient with respect to  $\boldsymbol{x}_i$  of  $\theta^I_{x_ix_j}$ . In Appendix B it is shown by setting  $\boldsymbol{x} = \boldsymbol{x}_i$  and  $\boldsymbol{y} = \boldsymbol{x}^I_j$  in Eq. (B.3) that

$$\theta_{x_i x_j}^{\prime I} = \frac{(\boldsymbol{x}_i - \boldsymbol{x}_j^I) \cdot \boldsymbol{t}_i}{|\boldsymbol{x}_i - \boldsymbol{x}_j^I|^2},\tag{5.5}$$

where  $t_i$  is a unit vector tangent to panel i (and pointing in the clockwise direction).

Note that Eq. (5.4) represents a reduction of the original system for the N unknowns  $\Phi_i^n$  to a system of equations for the N-1 unknowns  $\Upsilon_i^n$ , which means that, despite the assurance in some publications Katz and Plotkin, 2001 that the Neumann formulation can be resolved in terms of the velocity potentials  $\Phi_i^n$ , this is not correct. The matrix one obtains for the linear system associated with these variables is singular, reflecting the fact that an arbitrary constant can always be added to the potential. In the Dirichlet formulation this constant was fixed by the choice of  $\Phi_\infty$  but, with the Neumann formulation, in which a derivative condition is applied, this constant remains undetermined. The appropriate variables for the Neumann formulation, which lead to a nonsingular matrix, are the potential differences  $\Upsilon_i^n$ .

The numerical expression (5.4) is evaluated at the collocation points  $x_i$  but must be moved to the points  $p_i$  for the purpose of error comparison (see the relationship between  $x_i$  and  $p_i$  in Figure 4.2). To this end we define the differences

$$\lambda_i^n = \begin{cases} \Phi^n(\boldsymbol{p}_i) - \Phi^n(\boldsymbol{p}_{i-1}) & \text{convex case} \\ \Phi_i^n - \Phi_{i-1}^n = \Upsilon_i^n & \text{concave case} \end{cases}, \tag{5.6}$$

and, for reference, the "true" differences

$$\lambda_i = \Phi(\boldsymbol{p}_i) - \Phi(\boldsymbol{p}_{i-1}). \tag{5.7}$$

We then define the error  $\varepsilon_i$  at panel i by

$$l\varepsilon_i = (\lambda_i - \lambda_i^n),\tag{5.8}$$

factoring out the "trivial" l-dependence that reflects the reduction in  $\Upsilon_i$  as the two neighboring collocation points get closer.

The mean value theorem allows us to write (in the convex case)

$$\Phi^{n}(\boldsymbol{p}_{i}) = \Phi^{n}(\boldsymbol{x}_{i}) + \nabla \Phi^{n}(\boldsymbol{z}_{i}) \cdot (\boldsymbol{p}_{i} - \boldsymbol{x}_{i}) = \Phi^{n}_{i} + O(l^{2}),$$
(5.9)

where  $z_i$  is a point between  $p_i$  and  $x_i$  and we have assumed that the points of comparison  $p_i$  are located "directly above"  $x_i$  such that  $t_i \cdot (p_i - x_i) = O(l^2)$  (see Section 4.2). Thus we can write

$$\lambda_i^n = \Upsilon_i^n + O(l^2). \tag{5.10}$$

Equivalently, since the mean value theorem also assures us that  $\Phi^n(\boldsymbol{p}_i) - \Phi^n(\boldsymbol{p}_{i-1}) = O(l)$ , we can write  $\lambda_i^n = O(l)$  and hence

$$\Upsilon_i^n = \lambda_i^n [1 + O(l)]. \tag{5.11}$$

Note that in the concave case the error term vanishes. Using Eq. (5.11), Eq. (5.4) becomes

$$\sum_{j=2}^{N} \theta_{x_i x_j}^{\prime I} \lambda_j^n [1 + O(l)] = 2\pi V_{x_i \infty}^{\perp}.$$
 (5.12)

Expression (4.2) for the true velocity potential at a point p outside, or on the surface, of the body can be written, in terms of angles (see Figure 5.1, with p in place of  $x_i$ ), as

$$\Phi(\boldsymbol{p}) = \frac{1}{2\pi} \sum_{j=1}^{N} \int_{L_{j}} \Phi(\boldsymbol{s}_{j}) d\theta_{ps_{j}} - \frac{\Gamma}{2\pi} \theta_{px_{N}}^{F} + \Phi_{\infty}(\boldsymbol{p}).$$
 (5.13)

The requirement that the normal velocity component vanish for  $p = s_i$  on the surface (of panel i) gives  $n \cdot \nabla \Phi(s_i) = 0$  and it is necessary to relate this expression to the numerical condition (5.12).

The mean value theorem, applied to each component of  $\nabla \Phi$ , allows us to conclude

$$\nabla \Phi(\mathbf{s}_i) = \nabla \Phi(\mathbf{p}_i) + O(l), \tag{5.14}$$

a result that holds for both the convex and concave case. We also need to relate the unit normal vector n at the point  $s_i$  on the surface to  $n_i$ , which is normal to the panel. In Appendix C, it is shown using straightforward geometric arguments that

$$\boldsymbol{n} = \boldsymbol{n}_i + O(l). \tag{5.15}$$

Finally, using Eqs. (5.14) and (5.15) we have

$$\boldsymbol{n} \cdot \nabla \Phi(\boldsymbol{s}_i) = \boldsymbol{n}_i \cdot \nabla \Phi(\boldsymbol{p}_i) + O(l) = 0. \tag{5.16}$$

To calculate the errors  $\varepsilon_i$ , see Eq. (5.8), we first need to manipulate Eq. (5.13)

so as to express the Neumann derivative condition in terms of  $\lambda_i$ . To this end we set  $p = p_i$  and write

$$\Phi(\boldsymbol{p}_{i}) = \frac{1}{2\pi} \sum_{\substack{j=1\\j\neq i}}^{N} \int_{L_{j}} [\Phi(\boldsymbol{p}_{j}) + \Phi(\boldsymbol{s}_{j}) - \Phi(\boldsymbol{p}_{j})] d\theta_{p_{i}s_{j}} + \frac{1}{2\pi} \int_{L_{i}} \Phi(\boldsymbol{s}_{i}) d\theta_{p_{i}s_{i}} - \frac{\Gamma}{2\pi} \theta_{p_{i}x_{N}}^{F} + \Phi_{\infty}(\boldsymbol{p}_{i}).$$
(5.17)

Integrating by parts for the integral over  $L_i$ , and using the fact that  $\Phi(\mathbf{p}_j)$  is a constant for a fixed point of comparison  $\mathbf{p}_j$ , we have

$$\Phi(\boldsymbol{p}_{i}) = \frac{1}{2\pi} \sum_{\substack{j=1\\j\neq i}}^{N} \Phi(\boldsymbol{p}_{j}) \left[ \theta_{p_{i}x_{j}}^{F} - \theta_{p_{i}x_{j}}^{I} \right] + \frac{1}{2\pi} \sum_{\substack{j=1\\j\neq i}}^{N} \int_{L_{j}} \left[ \Phi(\boldsymbol{s}_{j}) - \Phi(\boldsymbol{p}_{j}) \right] d\theta_{p_{i}s_{j}} + \frac{1}{2\pi} \left[ \Phi(\boldsymbol{x}_{i}^{F}) \theta_{p_{i}x_{i}}^{F} - \Phi(\boldsymbol{x}_{i}^{I}) \theta_{p_{i}x_{i}}^{I} \right] - \frac{1}{2\pi} \int_{L_{i}}^{I} \frac{d\Phi}{ds} \theta_{p_{i}s_{i}} ds - \frac{\Gamma}{2\pi} \theta_{p_{i}x_{N}}^{F} + \Phi_{\infty}(\boldsymbol{p}_{i}).$$
(5.18)

Applying the Neumann condition in light of Eq. (5.16) we have  $\mathbf{n}_i \cdot \nabla_{p_i} \Phi(\mathbf{p}_i) = O(l)$ , or

$$O(l) = \frac{1}{2\pi} \sum_{\substack{j=1\\j\neq i}}^{N} \Phi(\mathbf{p}_{j}) [\theta_{p_{i}x_{j}}^{\prime F} - \theta_{p_{i}x_{j}}^{\prime I}] + \frac{1}{2\pi} \sum_{\substack{j=1\\j\neq i}}^{N} \int_{L_{j}} [\Phi(\mathbf{s}_{j}) - \Phi(\mathbf{p}_{j})] d\theta_{p_{i}s_{j}}^{\prime} + \frac{1}{2\pi} [\Phi(\mathbf{x}_{i}^{F}) \theta_{p_{i}x_{i}}^{\prime F} - \Phi(\mathbf{x}_{i}^{I}) \theta_{p_{i}x_{i}}^{\prime I}] - \frac{1}{2\pi} \int_{L_{i}} \frac{d\Phi}{ds} \theta_{p_{i}s_{i}}^{\prime} ds - \frac{\Gamma}{2\pi} \theta_{p_{i}x_{N}}^{\prime F} + V_{p_{i}\infty}^{\perp}.$$

$$(5.19)$$

Using the mean value theorem we can move the point of evaluation of the third term in the RHS of Eq. (5.19) from the endpoints of the panel to the point  $p_i$ . The details of this are given in Section 5.2, where we find in Eq. (5.36) that

$$\Phi(\mathbf{x}_{i}^{F})\theta_{p_{i}x_{i}}^{F} - \Phi(\mathbf{x}_{i}^{I})\theta_{p_{i}x_{i}}^{I} = \Phi(\mathbf{p}_{i})(\theta_{p_{i}x_{i}}^{F} - \theta_{p_{i}x_{i}}^{I}) + O(l).$$
(5.20)

Eq. (5.19) then becomes

$$O(l) = \frac{1}{2\pi} \sum_{j=1}^{N} \Phi(\mathbf{p}_{j}) [\theta_{p_{i}x_{j}}^{\prime F} - \theta_{p_{i}x_{j}}^{\prime I}] + \frac{1}{2\pi} \sum_{\substack{j=1\\j\neq i}}^{N} \int_{L_{j}} [\Phi(\mathbf{s}_{j}) - \Phi(\mathbf{p}_{j})] d\theta_{p_{i}s_{j}}^{\prime} - \frac{1}{2\pi} \int_{L_{s}} \frac{d\Phi}{ds} \theta_{p_{i}s_{i}}^{\prime} ds - \frac{\Gamma}{2\pi} \theta_{p_{i}x_{N}}^{\prime F} + V_{p_{i}\infty}^{\perp}.$$
(5.21)

We can use that  $\theta_{p_ix_{j-1}}^{\prime F}=\theta_{p_ix_j}^{\prime I}$  to regroup the terms in the first sum in the RHS of Eq. (5.21) and introduce the variables  $\lambda_i$ , defined in Eq. (5.7),

$$O(l) = -\frac{1}{2\pi} \sum_{j=2}^{N} \lambda_j \theta_{p_i x_j}^{\prime I} + \frac{1}{2\pi} \left[ \Phi(\boldsymbol{p}_N) \theta_{p_i x_N}^{\prime F} - \Phi(\boldsymbol{p}_1) \theta_{p_i x_1}^{\prime I} \right] +$$

$$+ \frac{1}{2\pi} \sum_{\substack{j=1\\j\neq i}}^{N} \int_{L_j} \left[ \Phi(\boldsymbol{s}_j) - \Phi(\boldsymbol{p}_j) \right] d\theta_{p_i s_j}^{\prime} - \frac{1}{2\pi} \int_{L_i} \frac{d\Phi}{ds} \theta_{p_i s_i}^{\prime} ds - \frac{\Gamma}{2\pi} \theta_{p_i x_N}^{\prime F} + V_{p_i \infty}^{\perp}.$$

$$(5.22)$$

To simplify the above expression, we make use of the fact that  $\theta^I_{p_ix_1}=\theta^F_{p_ix_N}$  and  $\Gamma=\Phi(\boldsymbol{x}^F_N)-\Phi(\boldsymbol{x}^I_1)$  to write

$$\Phi(\boldsymbol{p}_{N})\theta_{p_{i}x_{N}}^{\prime F} - \Phi(\boldsymbol{p}_{1})\theta_{p_{i}x_{1}}^{\prime I} - \Gamma\theta_{p_{i}x_{N}}^{\prime F} = 
= \left[\Phi(\boldsymbol{p}_{N}) - \Phi(\boldsymbol{x}_{N}^{F}) + \Phi(\boldsymbol{x}_{1}^{I}) - \Phi(\boldsymbol{p}_{1})\right]\theta_{p_{i}x_{N}}^{\prime F}.$$
(5.23)

Because this term involves the difference in potential between two points related to the first and on the final panel, it is O(l) provided that panel i is not too close to the wake panel (i.e., so long as  $\theta_{p_ix_N}^{\prime F}$  is O(1)). Panels near the wake require special care, but it can be shown (see Section 5.2) that the term highlighted in Eq. (5.23) remains O(l) in the case that the upper and lower surfaces of the body meet with a finite angle and, in the case of a cusp, when the collocation point is assumed to lie at the midpoint of the panel and the first and final panels are of the same size (differing by at most  $O(l^2)$ ).

Finally, Eq. (5.22) can be written

$$\sum_{j=2}^{N} \lambda_{j} \theta_{p_{i}x_{j}}^{\prime I} = \sum_{\substack{j=1\\j\neq i}}^{N} \int_{L_{j}} [\Phi(\boldsymbol{s}_{j}) - \Phi(\boldsymbol{p}_{j})] d\theta_{p_{i}s_{j}}^{\prime} - \int_{L_{i}} \frac{d\Phi}{ds} \theta_{p_{i}s_{i}}^{\prime} ds + 2\pi V_{p_{i}\infty}^{\perp} + O(l).$$
(5.24)

To compare this with the numerical condition (5.12) we use the fact (see Section 5.2) that, for the convex case,

$$\theta_{p_i x_j}^{II} = \theta_{x_i x_j}^{II} + O(l^2/|\mathbf{x}_i - \mathbf{x}_j^I|^2) = \theta_{x_i x_j}^{II} [1 + O(l)],$$
(5.25)

for panel j near panel i. If not the order of the term inside the brackets would be  $1 + O(l^2)$ . This expression is easily obtained from Eq. (5.45) considering that  $p_i$  is "directly above"  $x_i$ . For the concave case  $p_i = x_i$ , so

$$\theta_{p_i x_j}^{II} = \theta_{x_i x_j}^{II}. {(5.26)}$$

Then, after subtracting Eq. (5.12) from Eqs. (5.24) we can write

$$\sum_{j=2}^{N} (\lambda_j - \lambda_j^n) \theta_{x_i x_j}^{\prime I} [1 + O(l)] =$$

$$= \sum_{\substack{j=1\\j \neq i}}^{N} \int_{L_j} [\Phi(\boldsymbol{s}_j) - \Phi(\boldsymbol{p}_j)] d\theta_{p_i s_j}^{\prime} - \int_{L_i} \frac{d\Phi}{ds} \theta_{p_i s_i}^{\prime} ds + O(l), \qquad (5.27)$$

where we have used Eq. (5.16),

$$V_{p_i\infty}^{\perp} = V_{x_i\infty}^{\perp} + O(l). \tag{5.28}$$

Equation (5.27) constitutes a linear system of equations for the N-1 error terms  $\varepsilon_i$  (Eq. (4.19)),

$$\sum_{j=2}^{N} l\theta_{x_i x_j}^{\prime I} \varepsilon_j [1 + O(l)] = \sum_{\substack{j=1\\j \neq i}}^{N} \int_{L_j} [\Phi(\boldsymbol{s}_j) - \Phi(\boldsymbol{p}_j)] d\theta_{p_i s_j}^{\prime} - \int_{L_i} \frac{d\Phi}{ds} \theta_{p_i s_i}^{\prime} ds + O(l).$$
(5.29)

The matrix  $l\theta_{x_ix_j}^{\prime I}$  is expected to be well-behaved because only matrix elements near the diagonal are O(1), when  $\theta_{x_ix_j}^{\prime I} = O(l^{-1})$ , while elements become O(l) when |i-j| is large. The order of the errors  $\varepsilon_i$  should thus be the same as the RHS of Eq. (5.29), which must now be estimated. The details of this are included in Section 5.2 where it is proved that the RHS is shown to be  $O(l \ln l)$ , but only if the collocation points are the midpoints of each panel and point  $p_i$  is "directly above"  $x_i$  (or coincident with, in the concave case). If these two conditions are met, then it can be stated from Eq. (5.29) that

$$\varepsilon_i = O(l \ln(l)). \tag{5.30}$$

#### 5.2 Details of the Neumann error estimate

We provide here the details of the results used in the Neumann error estimate. Using the developments done in Appendix B it is now straightforward to derive Eqs. (5.20). First, setting in Eq. (B.3),  $x = p_i$  and  $y = s_i$  and if we observe that, since in local  $(\xi_i, \eta_i)$  coordinates, see Appendix C,  $p_i = (\xi_i(p_i), O(l^2))$  for the convex case and  $p_i = (\xi_i(p_i), 0)$  for the concave and  $s_i = (\xi_i, O(l^2))$ , we have

$$\theta'_{p_i s_i} = \frac{(\boldsymbol{p}_i - \boldsymbol{s}_i) \cdot \boldsymbol{t}_i}{|\boldsymbol{p}_i - \boldsymbol{s}_i|^2} = \frac{\xi_i(\boldsymbol{p}_i) - \xi_i}{(\xi_i(\boldsymbol{p}_i) - \xi_i)^2 + O(l^4)} = \frac{1 + O(l^2)}{\xi_i(\boldsymbol{p}_i) - \xi_i}.$$
 (5.31)

So, for  $s_i = x_i^I = (-l_i/2, 0)$ , we have

$$\theta_{p_i x_i}^{\prime I} = \frac{(\boldsymbol{p}_i - \boldsymbol{x}_i^I) \cdot \boldsymbol{t}_i}{|\boldsymbol{p}_i - \boldsymbol{x}_i^I|^2} = \frac{\xi_i(\boldsymbol{p}_i) + l_i/2}{(\xi_i(\boldsymbol{p}_i) + l_i/2)^2 + O(l^4)}, = \frac{1 + O(l^2)}{\xi_i(\boldsymbol{p}_i) + l_i/2}$$
(5.32)

and, similarly, for  $s_i = \boldsymbol{x}_i^F = (l_i/2, 0)$ ,

$$\theta_{p_i x_i}^{\prime F} = \frac{(\boldsymbol{p}_i - \boldsymbol{x}_i^F) \cdot \boldsymbol{t}_i}{|\boldsymbol{p}_i - \boldsymbol{x}_i^F|^2} = \frac{\xi_i(\boldsymbol{p}_i) - l_i/2}{(\xi_i(\boldsymbol{p}_i) - l_i/2)^2 + O(l^4)} \cdot = \frac{1 + O(l^2)}{\xi_i(\boldsymbol{p}_i) - l_i/2}$$
(5.33)

Then, the mean value theorem allows us to write

$$\Phi(\boldsymbol{x}_{i}^{I}) = \Phi(\boldsymbol{p}_{i}) + \frac{d\Phi}{ds}(\boldsymbol{p}_{i})[s(\boldsymbol{x}_{i}^{I}) - s(\boldsymbol{p}_{i})] + O(l^{2}) = 
= \Phi(\boldsymbol{p}_{i}) + \frac{d\Phi}{ds}(\boldsymbol{p}_{i})[\xi(\boldsymbol{x}_{i}^{I}) - \xi_{i}(\boldsymbol{p}_{i}) + O(l^{2})] + O(l^{2}) = 
= \Phi(\boldsymbol{p}_{i}) + \frac{d\Phi}{ds}(\boldsymbol{p}_{i})[-l_{i}/2 - \xi_{i}(\boldsymbol{p}_{i})] + O(l^{2}),$$
(5.34)

where we have also made use of Eq. (C.3). Similarly, we have

$$\Phi(\boldsymbol{x}_i^F) = \Phi(\boldsymbol{p}_i) + \frac{d\Phi}{ds}(\boldsymbol{p}_i)[l_i/2 - \xi_i(\boldsymbol{p}_i)] + O(l^2).$$
(5.35)

Together, Eqs (5.32)-(5.35) imply that the leading order terms involving  $\partial \Phi / \partial s_i(\mathbf{p}_i)$  cancel in the expression of interest, leaving us with

$$\Phi(\boldsymbol{x}_{i}^{F})\theta_{p_{i}x_{i}}^{F} - \Phi(\boldsymbol{x}_{i}^{I})\theta_{p_{i}x_{i}}^{F} = 
= \Phi(\boldsymbol{p}_{i})(\theta_{p_{i}x_{i}}^{F} - \theta_{p_{i}x_{i}}^{F}) + \frac{d\Phi}{ds}(\boldsymbol{p}_{i})\left[1 - 1 + O(l^{2})\right] + O(l^{2}\theta_{p_{i}x_{i}}^{F}, l^{2}\theta_{p_{i}x_{i}}^{F}) = 
= \Phi(\boldsymbol{p}_{i})(\theta_{p_{i}x_{i}}^{F} - \theta_{p_{i}x_{i}}^{F}) + O(l),$$
(5.36)

where we have used the fact that  $\theta_{p_ix_i}^{\prime I}$  and  $\theta_{p_ix_i}^{\prime F}$  are O(1/l).

We now consider Eq. (5.23) when panel i is close to the wake panel and  $\theta_{p_ix_N}^{\prime F} = O(1/l)$ . We can apply Eqs. (5.34) and (5.35) to the first and final panels, respectively, to obtain

$$\left[\Phi(\boldsymbol{p}_{N}) - \Phi(\boldsymbol{x}_{N}^{F}) + \Phi(\boldsymbol{x}_{1}^{I}) - \Phi(\boldsymbol{p}_{1})\right] \theta_{p_{i}x_{N}}^{\prime F} = 
= \left\{ \frac{d\Phi}{ds}(\boldsymbol{p}_{N}) \left[\xi_{N}(\boldsymbol{p}_{N}) - l_{N}/2\right] - \frac{d\Phi}{ds}(\boldsymbol{p}_{1}) \left[\xi_{1}(\boldsymbol{p}_{1}) + l_{1}/2\right] + O(l^{2}) \right\} \theta_{p_{i}x_{N}}^{\prime F}.$$
(5.37)

If the upper and lower surfaces meet with a finite angle at the trailing edge, then

we can assume  $d\Phi/ds = O(l)$  at  $\mathbf{p}_1$  and  $\mathbf{p}_N$ . Hence, the term within curly brackets in Eq. (5.37) is  $O(l^2)$  while the entire term is O(l). If the trailing edge instead resembles a cusp, then we can write  $d\Phi/ds_1(\mathbf{p}_1) = -d\Phi/ds_N(\mathbf{p}_N) + O(l)$ , which ensures that the velocities are (nearly) equal on the first and final panels (while the sense of ds is opposite). We may then simplify Eq. (5.37) to

$$\left[\Phi(\boldsymbol{p}_{N}) - \Phi(\boldsymbol{x}_{N}^{F}) + \Phi(\boldsymbol{x}_{1}^{I}) - \Phi(\boldsymbol{p}_{1})\right] \theta_{p_{i}x_{N}}^{\prime F} = 
= \left\{ \frac{d\Phi}{ds}(\boldsymbol{p}_{N}) \left[\xi_{1}(\boldsymbol{p}_{1}) + \xi_{N}(\boldsymbol{p}_{N}) + (l_{1} - l_{N})/2\right] + O(l^{2}) \right\} \theta_{p_{i}x_{N}}^{\prime F}.$$
(5.38)

The term within square brackets is apparently O(l), but becomes  $O(l^2)$  in the special case of interest, when the points of comparison are in the middle of the panels,  $\xi_1(\boldsymbol{p}_1) = \xi_N(\boldsymbol{p}_N) = 0$ , and the panels themselves are of (nearly) equal length,  $l_1 - l_N = O(l^2)$ . In that case, the entire term in Eq. (5.38) is O(l).

We now consider the second term on the RHS of Eq. (5.29). Using Eq. (C.3) and Eq. (5.31) and integrating by parts, we have

$$\int_{L_{i}} \frac{d\Phi}{ds} \theta'_{p_{i}s_{i}} ds = \int_{L_{i}} \frac{d\Phi}{ds} \theta'_{p_{i}s_{i}} \left(1 + O(l^{2})\right) d\xi_{i} = \left(1 + O(l^{2})\right) \int_{L_{i}} \frac{d\Phi}{ds} \frac{(1 + O(l^{2}))}{\xi_{i}(\mathbf{p}_{i}) - \xi_{i}} d\xi_{i} = \\
= \left(1 + O(l^{2})\right) \left[ -\frac{d\Phi}{ds} (\mathbf{x}_{i}^{F}) \ln |\xi_{i}(\mathbf{p}_{i}) - \xi_{i}(\mathbf{x}_{i}^{F})| + \frac{d\Phi}{ds} (\mathbf{x}_{i}^{I}) \ln |\xi_{i}(\mathbf{p}_{i}) - \xi_{i}(\mathbf{x}_{i}^{I})| \right] + \\
+ \left(1 + O(l^{2})\right) \left[ \int_{L_{i}} \frac{d^{2}\Phi}{ds^{2}} \ln |\xi_{i}(\mathbf{p}_{i}) - \xi_{i}| d\xi_{i} \right] = \\
= \left(1 + O(l^{2})\right) \left[ \left(\frac{d\Phi}{ds} (\mathbf{p}_{i}) + \frac{d^{2}\Phi}{ds^{2}} (\mathbf{z}_{s})(s(\mathbf{p}_{i}) - s(\mathbf{x}_{i}^{F}))\right) \ln |\xi_{i}(\mathbf{p}_{i}) - \xi_{i}(\mathbf{x}_{i}^{F})| \right] + \\
+ \left(1 + O(l^{2})\right) \left[ \int_{L_{i}} \frac{d^{2}\Phi}{ds^{2}} \ln |\xi_{i}(\mathbf{p}_{i}) - \xi_{i}| d\xi_{i} \right] = \\
= \left(1 + O(l^{2})\right) \left[ \int_{L_{i}} \frac{d^{2}\Phi}{ds^{2}} \ln |\xi_{i}(\mathbf{p}_{i}) - \xi_{i}| d\xi_{i} \right] + \\
+ \left(1 + O(l^{2})\right) \left[ \int_{L_{i}} \frac{d^{2}\Phi}{ds^{2}} \ln |\xi_{i}(\mathbf{p}_{i}) - \xi_{i}| d\xi_{i} \right], \tag{5.39}$$

where the mean value theorem for the convex case has been applied and provided two conditions hold:

- (i) the collocation points  $x_i$  are located at the center of the panels  $l_i$ ,
- (ii) the points of comparison  $p_i$  are located "directly above" (or coincident with, in the concave case) the  $x_i$  such that  $t_i \cdot (p_i x_i) = O(l^2)$  where  $t_i$  is a unit vector tangent to panel i.

With the previous considerations the dominant terms in Eq. (5.39) are of order  $O(l \ln l)$ . For brevity, the development for concave case is not included, because it is very similar to the convex case.

We now consider the first term on the RHS of Eq. (5.29) for the convex case. By applying the mean value theorem we have:

$$\sum_{\substack{j=1\\j\neq i}}^{N} \int_{L_{j}} [\Phi(\boldsymbol{s}_{j}) - \Phi(\boldsymbol{p}_{j})] d\theta'_{p_{i}s_{j}} = \sum_{\substack{j=1\\j\neq i}}^{N} \int_{L_{j}} \left( \frac{d\Phi}{ds}(\boldsymbol{p}_{j}) s_{j} + O(l^{2}) \right) d\theta'_{p_{i}s_{j}} =$$

$$= \sum_{\substack{j=1\\j\neq i}}^{N} \frac{d\Phi}{ds}(\boldsymbol{p}_{j}) \int_{L_{j}} s_{j} d\theta'_{p_{i}s_{j}} + \sum_{\substack{j=1\\j\neq i}}^{N} \int_{L_{j}} O(l^{2}) d\theta'_{p_{i}s_{j}}, \quad (5.40)$$

where

$$s_j = s(\boldsymbol{s}_j) - s(\boldsymbol{p}_j). \tag{5.41}$$

First, we are going to estimate the order of the dominant term in the RHS of Eq. (5.40) for panels far from panel i: Then, by applying the mean theorem for integrals, we have:

$$\int_{L_j} s_j d\theta'_{p_i s_j} = O(l) (\theta'^F_{p_i x_j} - \theta'^I_{p_i x_j}).$$
(5.42)

From Eq. (B.3) we have

$$\theta'_{p_i s_j} = \frac{(\boldsymbol{p}_i - \boldsymbol{s}_j) \cdot \boldsymbol{t}_i}{|\boldsymbol{p}_i - \boldsymbol{s}_j|^2} = \frac{\boldsymbol{p}_i \cdot \boldsymbol{t}_i - \xi_j \boldsymbol{t}_j \cdot \boldsymbol{t}_i}{(\xi_{i p_i} - \xi_j)^2 + \eta_{i p_i}^2} + O(l^2), \tag{5.43}$$

where we have used

$$s_j = \xi_j t_j + \eta_j n_j, \tag{5.44}$$

and  $\xi_j = O(l)$ ,  $\eta_j = O(l^2)$ ,  $\xi_{jp_i} = O(1)$ ,  $\eta_{jp_i} = O(1)$ . Then,

$$\theta_{p_{i}x_{j}}^{\prime F} - \theta_{p_{i}x_{j}}^{\prime I} = \boldsymbol{t}_{j} \cdot \boldsymbol{t}_{i} \left[ \frac{\xi_{jp_{i}} - l_{j}/2}{(\xi_{jp_{i}} - l_{j}/2)^{2} + \eta_{jp_{i}}^{2}} - \frac{\xi_{jp_{i}} + l_{j}/2}{(\xi_{jp_{i}} + l_{j}/2)^{2} + \eta_{jp_{i}}^{2}} \right] + O(l^{2}) =$$

$$= O(l). \tag{5.45}$$

and the integral of Eq. (5.42) is of order  $O(l^2)$ . So, the contribution of all the panels far from panel i will be of order O(l) or less.

Now, we are going to estimate the order of the dominant term in the RHS of Eq. (5.29) for panels near panel i. Then, from Eq. (B.3) we have

$$\theta'_{p_i s_j} = \mathbf{t}_j \cdot \mathbf{t}_i \frac{1}{\xi_{j p_i} - \xi_j} + O(l), \tag{5.46}$$

where it has been supposed that  $\xi_{jp_i} = O(l)$ ,  $\eta_{jp_i} = O(l^2)$ . Differentiating with respect to  $\xi_j$  in Eq. (5.46) and maintaining only the dominant term,

$$d\theta'_{p_i s_j} \simeq \boldsymbol{t}_j \cdot \boldsymbol{t}_i \frac{d\xi_j}{(\xi_{j p_i} - \xi_j)^2},\tag{5.47}$$

and by substituting Eq. (5.47) in the dominant term in the RHS of Eq. (5.40) and maintaining only the dominant term, we have

$$\int_{L_{j}} s_{j} d\theta'_{p_{i}s_{j}} \simeq \boldsymbol{t}_{j} \cdot \boldsymbol{t}_{i} \int_{-l_{j}/2}^{l_{j}/2} \frac{\xi_{j} d\xi_{j}}{(\xi_{jp_{i}} - \xi_{j})^{2}} = \boldsymbol{t}_{j} \cdot \boldsymbol{t}_{i} \left[ \ln |\xi_{j} - \xi_{jp_{i}}| - \frac{\xi_{jp_{i}}}{\xi_{j} - \xi_{jp_{i}}} \right]_{-l_{j}/2}^{l_{j}/2} = 
= \boldsymbol{t}_{j} \cdot \boldsymbol{t}_{i} \left[ \ln |\xi_{j} - \xi_{jp_{i}}| - \frac{\xi_{jp_{i}}}{\xi_{j} - \xi_{jp_{i}}} \right]_{-l_{j}/2}^{l_{j}/2} = 
= \boldsymbol{t}_{j} \cdot \boldsymbol{t}_{i} \left[ \ln \left| \frac{l_{j}/2 - \xi_{jp_{i}}}{l_{j}/2 + \xi_{jp_{i}}} \right| - \frac{\xi_{jp_{i}}}{l_{j}/2 - \xi_{jp_{i}}} - \frac{\xi_{jp_{i}}}{l_{j}/2 + \xi_{jp_{i}}} \right],$$
(5.48)

which tends to infinite. However, grouping the terms in the sum in j by taking the panels near panel i in pairs as  $j_1 = i - 1$  with  $j'_1 = i + 1$ ,  $j_2 = i - 2$  with

 $j_2'=i+2, ..., j_k=i-k$  with  $j_k'=i+k$  and assuming that  $\xi_{j_kp_i}=-\xi_{j_k'p_i}+O(l^2)$ ,  $l_j=l_i+O(l^2)$ ,  $l_{j_k'}=l_i+O(l^2)$ ,  $\boldsymbol{t}_{j_k}=\boldsymbol{t}_i+O(l^2)$  and  $\boldsymbol{t}_{j_k'}=\boldsymbol{t}_i+O(l^2)$ , the sum of the RHS of Eq. (5.48) for  $j_k=i-k$  and  $j_k'=i+k$  would be of order O(l), but, as the integral is multiply by the factor  $\frac{d\Phi}{ds}(\boldsymbol{p}_j)$  (see Eq. (5.40)), we have to sum next expression:

$$\frac{d\Phi}{ds}(\mathbf{p}_{j_{k}}) \int_{L_{j_{k}}} s_{j_{k}} d\theta'_{p_{i}s_{j_{k}}} + \frac{d\Phi}{ds}(\mathbf{p}_{j'_{k}}) \int_{L_{j'_{k}}} s_{j'_{k}} d\theta'_{p_{i}s_{j'_{k}}} = 
= \frac{d\Phi}{ds}(\mathbf{p}_{j_{k}}) \int_{L_{j_{k}}} s_{j_{k}} d\theta'_{p_{i}s_{j_{k}}} + \left(\frac{d\Phi}{ds}(\mathbf{p}_{j_{k}}) + O(l)\right) \int_{L_{j'_{k}}} s_{j'_{k}} d\theta'_{p_{i}s_{j'_{k}}},$$
(5.49)

where the mean value theorem has been applied. So, the order of this sum is O(l) multiply by the dominant order of Eq. (5.48), that is,  $O(l \ln l)$ , the same order of the second term of the RHS of Eq. (5.29), so we can conclude that

$$\varepsilon_i = O(l \ln l). \tag{5.50}$$

## 5.3 Results and Discussions

In this Section the errors  $\varepsilon$  as defined in Eq. (5.8) are slightly reformulated so that the error order magnitude representation for different experiments is convenient. In order to validate the theoretical results several numerical experiments for bodies with and without sharp corners and with concave or convex parts are performed. A comparison of the numerical and analytical solutions determines the true numerical error and we check whether this result agrees with the theoretical prediction or not.

The resolution of the problem with Neumann boundary conditions, as presented in Eq. (5.4), provides  $\Upsilon_i^n$  potential differences with i=2:N, as defined in Eq. (5.2). While the resolution of the analytical problem for Joukowski or Karman-Treftz bodies (see Eq. (4.51) or Eq. (4.60)) provides either velocity potentials  $\Phi_i$  or

velocities  $V_i$  in the desired fluid domain evaluation points. In order to compare the numerical results with the analytical results and considering the definition of the error given in Eq. (5.8) and the relation provided in Eq. (5.10), we can write

$$\varepsilon_i = \frac{\lambda_i - \lambda_i^n}{l}; \quad \varepsilon_i = \frac{\lambda_i - \Upsilon_i^n + O(l^2)}{l}; \quad \varepsilon_i = \frac{\lambda_i - \Upsilon_i^n}{l} + O(l).$$
 (5.51)

Thus we need to calculate the analytical potential differences  $\lambda_i$ , defined in Eq. (5.7), for panels i=2:N (see Figure 5.2). The analytical values of  $\Phi_i$  are easily obtained in the points on the body surface located "directly above" the panel collocation points in order to calculate the analytical potential differences needed.

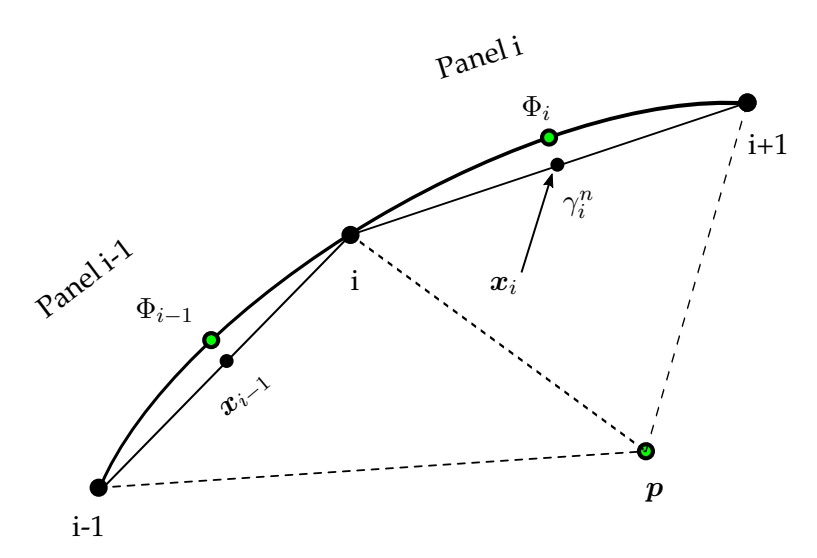


FIGURE 5.2: Illustration of the evaluation points for  $\lambda_i = \Phi_i - \Phi_{i-1}$  and  $\Upsilon_i^n$  calculation.

We then define the error  $\tilde{\varepsilon}_i$ , which is evaluated in the collocation point of the panels i=2:N, by

$$\tilde{\varepsilon}_i = \lambda_i - \Upsilon_i^n. \tag{5.52}$$

Introducing this definition in Eq. (5.51), it is obtained that

$$\varepsilon_i = \frac{\tilde{\varepsilon}_i}{l} + O(l); \quad \tilde{\varepsilon}_i = l\varepsilon_i + O(l^2).$$
 (5.53)

Applying the theoretical error order,  $\varepsilon_i = O(l \ln(l))$  (estimated in Section 5.1), to this expression, we obtain

$$\tilde{\varepsilon}_i = O(l^2 \ln(l)) + o(l^2). \tag{5.54}$$

Using the previously defined l = O(1/N), we can derive from Eq. (5.54) the error order  $\tilde{\varepsilon}_i$  as a function of the number of pannels N used in the obstacle discretization:

$$\tilde{\varepsilon}_i = O\left(\frac{1}{N^2} \ln\left(\frac{1}{N}\right)\right) = O\left(\frac{-1}{N^2} \ln(N)\right) = \frac{-k}{N^2} \ln(N) + o\left(\frac{\ln(N)}{N^2}\right). \tag{5.55}$$

For the error order magnitude representation, it is convenient to take logarithms in both sides of Eq. (5.55), so we can write down the following equation:

$$\ln(|\tilde{\varepsilon}_i|) = \ln\left(\frac{k}{N^2}\ln(N)\right) = \ln\left(\frac{\ln(N)}{N^2}\right) + \ln(k). \tag{5.56}$$

In the following sections the numerical experiment results are presented for different obstacle configurations. The representation of  $\ln(|\tilde{\varepsilon}_i|)$  in the y axis and  $\ln\left(\frac{\ln(N)}{N^2}\right)$  in the x axis of a plot, should result in a unity slope straight line, as long as the analytical Neumann global error if well estimated.

### 5.3.1 Numerical error results for thick bodies without sharp corners

To confirm these results the numerical error using Neumann boundary conditions is obtained for the same thick body without sharp corners (see Figure 4.7) that was used to validate the Dirichlet error results in Section 4.3.1. Figure 5.3 shows the numerical error obtained by comparing the numerical with the analytical solution under the same conditions used to obtain Figure 4.8. The use of different evaluation points of the body discretization and/or angles of attack (in this experiment the angle of attack is  $\alpha=2^{\circ}$ ) provides similar results. The problem is evaluated with the collocation points placed at the exact center of the

panels and, as advised previously during the theoretical developments, the magnitude of the error order is confirmed to match with the estimations. It is shown that the numerical local error  $\tilde{\varepsilon}_i$  tends to  $O\left(\frac{1}{N^2}\ln(N)\right)$  when the number of panels increases. This figure also shows the numerical error for this body when the collocation points are placed, instead, at the position  $l_i/3$ ; the order of the error in this case is higher as predicted by the theory, being the slope of the straigth line different than the unity. However, with the Neumann formulation, the order of the error for the none centered collocation points is not easily extracted from the theoretical analysis as happened in the Dirichlet formulation case.

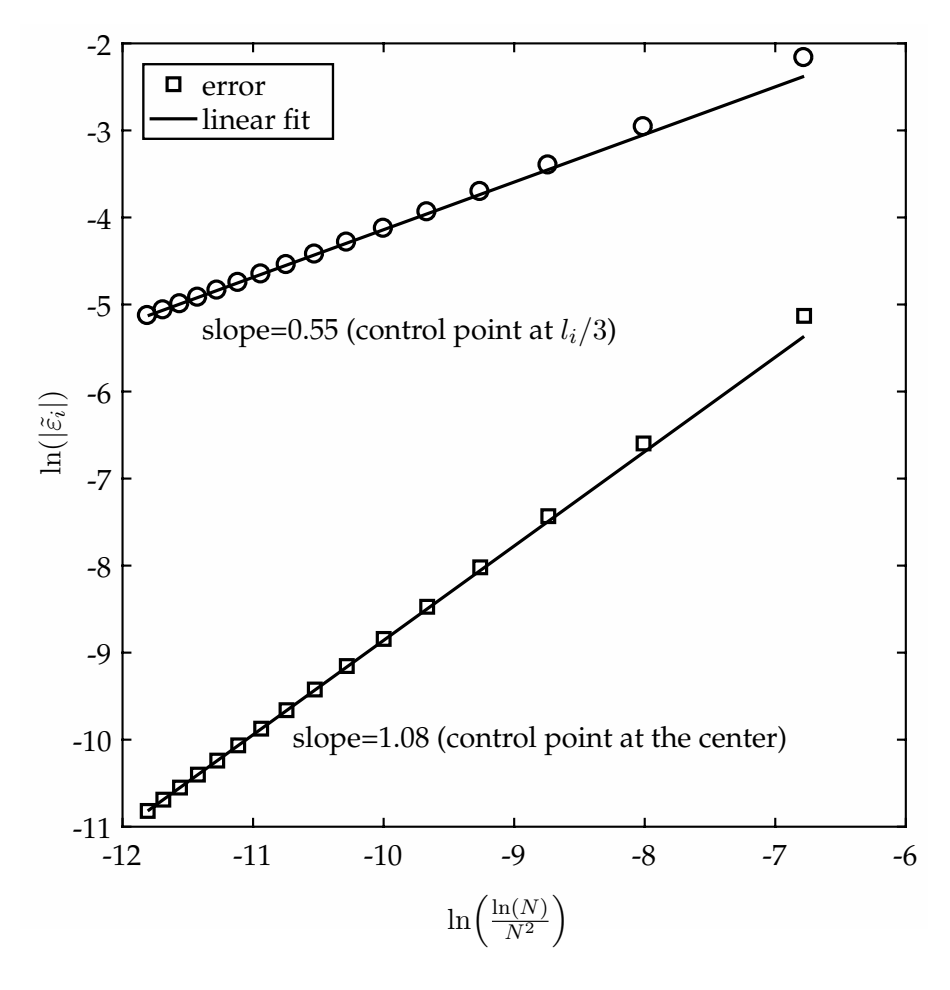


FIGURE 5.3: Comparison of the numerical error using the Neumann formulation for a thick ellipse with the collocation points placed at the center of the panels (lower curve) and at the position  $l_i/3$  (upper curve) for  $\alpha = 2^{\circ}$ .

To validate the theoretical results for bodies with both convex and concave parts, we calculate the numerical error for the same body used (see Figure 4.9) in the Dirichlet evaluation. Figure 5.4 shows the numerical error at two points placed at (x,y)=(-0.358,2.643) (on the convex part of the profile) and (x,y)=(-0.727,-0.0653) (the concave part of the profile) for  $\alpha=2^{\rm o}$  as a function of the number of panels. This figure shows that the numerical error is  $O\left(\frac{1}{N^2}\ln(N)\right)$  for both points, which is as the theoretical analysis predicts. Similar results are found at other points of the body and with different angles of attack.

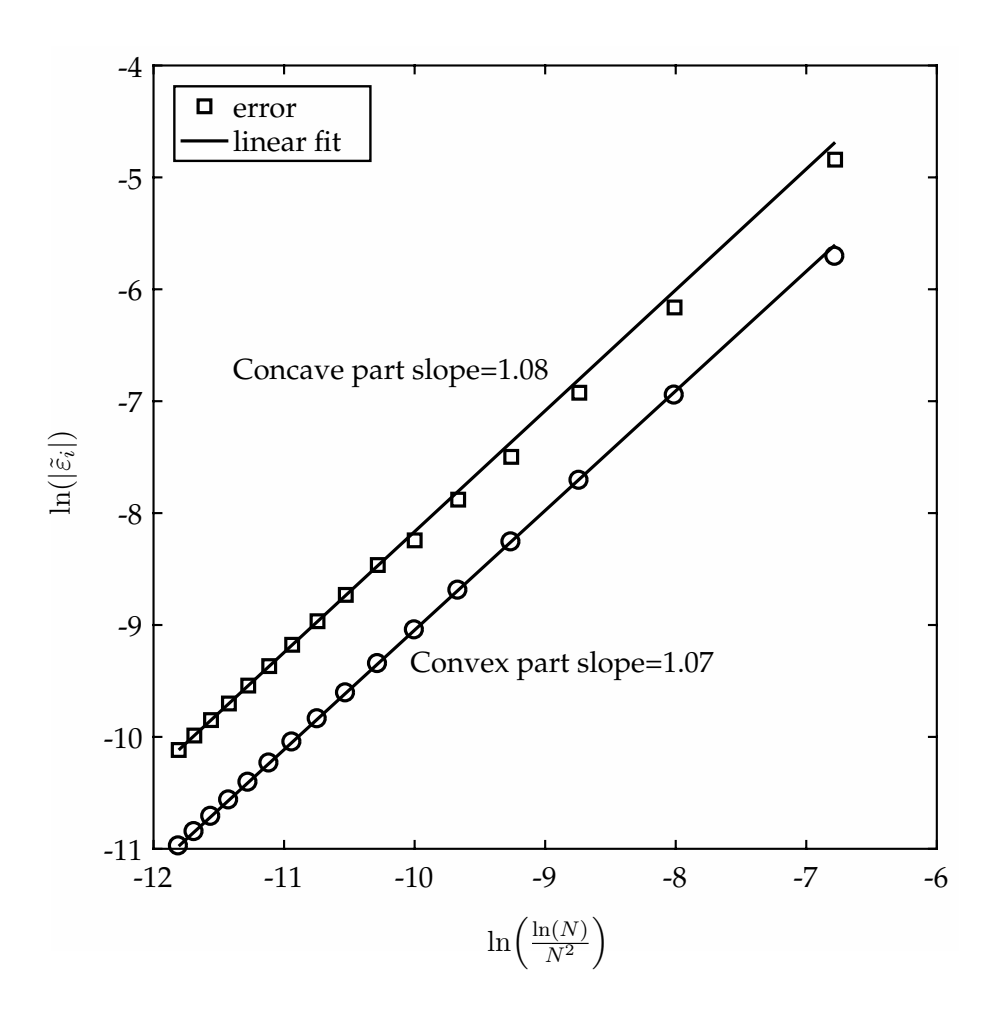


FIGURE 5.4: Numerical error using the Neumann formulation for a non-symmetric body with concave and convex parts for  $\alpha=2^{\rm o}$ .

#### 5.3.2 Numerical error results for thin bodies without sharp corners

To validate the analytical results we calculate the numerical error for the ellipse in Figure 5.5, with major axis of length 6.88 and minor axis of length 1.1. The ellipse and the analytical solution for the velocity potential around it have been obtained from a Joukowski transformation with a = 1.7 of a circle centered at  $(x_0, y_0) = (0, 0)$  with radius R = 2.

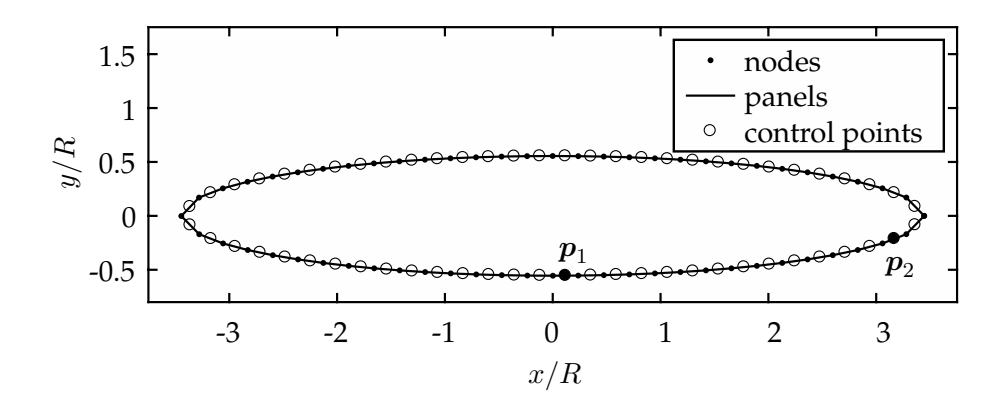


FIGURE 5.5: Thin ellipse obtained from a Youkovsky transformation with a=1.7.

Figure 5.6 shows the numerical error for  $\alpha=2^{\circ}$  at two points:  $p_1$  at (x,y)=(0.119,-0.554) and  $p_2$  at (x,y)=(3.169,-0.212) (near the trailing edge), as a function of the number of panels. This figure shows how the order of the numerical error decreases when the length of the panel decreases. It is  $O\left(\frac{1}{N^2}\ln(N)\right)$  when the length of the panel is sufficiently small compared to the length of the vertical axis of the ellipse, h. For points very close to the trailing edge the error is higher as expected but it slowly tends to the estimations at the expense of using a high number of panels. For thinner ellipses than the one presented in Figure 5.5, the numerical error order does not follow the analytical estimations as good as predicted; the main reason for this apparent limit in body thickness is a point for future works.

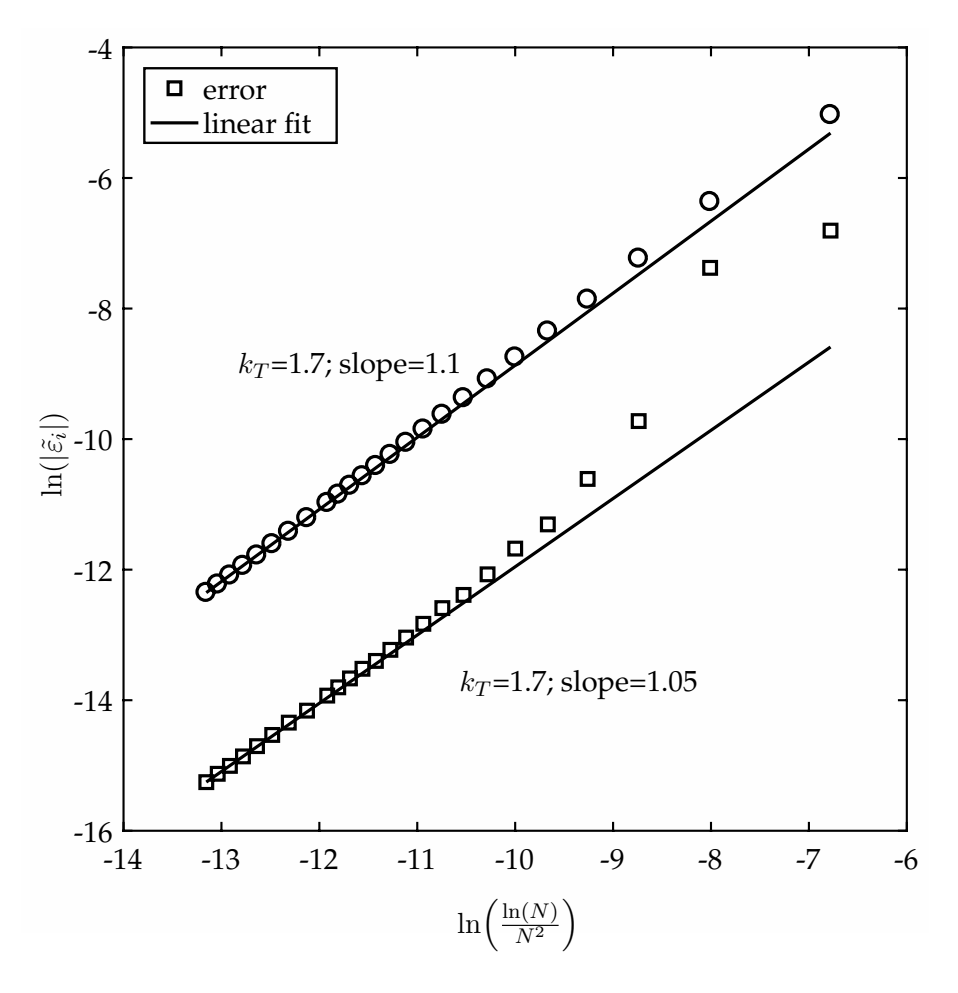


FIGURE 5.6: Numerical error using the Neumann formulation for a thin ellipse in two points, one of them very close to the trailing edge for  $\alpha=2^{\rm o}$ .

#### 5.3.3 Numerical error results for bodies with sharp corners

A similar approach than the one presented in Section 4.3.3 for the Dirichlet boundary conditions is followed in this Section, in order to prove that the estimations are correct also for bodies that show up sharp corners.

#### 5.3.3.1 Symmetric bodies with sharp corners

For the same symmetric bodies with sharp corners presented in Figure 4.15, which were obtained for different  $k_T$  and with  $(x_0, y_0) = (-0.2, 0)$  and R = 1, the order of the numerical error fits with the theoretical estimations as shown in Figure 5.7. This figure shows how the order of the numerical error decreases when the length of the panels decreases. This is true while the trailing edge angle

is not extremely sharp, i.e. while the firsts and lasts panels meet with a finite angle not tending to 0, so that it can be stated that the length of the panels, which is O(1/N), is sufficiently small compared to the thickness of the body. Later in this section, results for a body with an extreme trailing edge angle are discussed. It can be mention here that when using the Neumann formulation the error order is not affected due to the existence of sharp corners in the body, as did happened when using the Dirichlet formulation, see section 4.3.3.1, Figure 4.15.

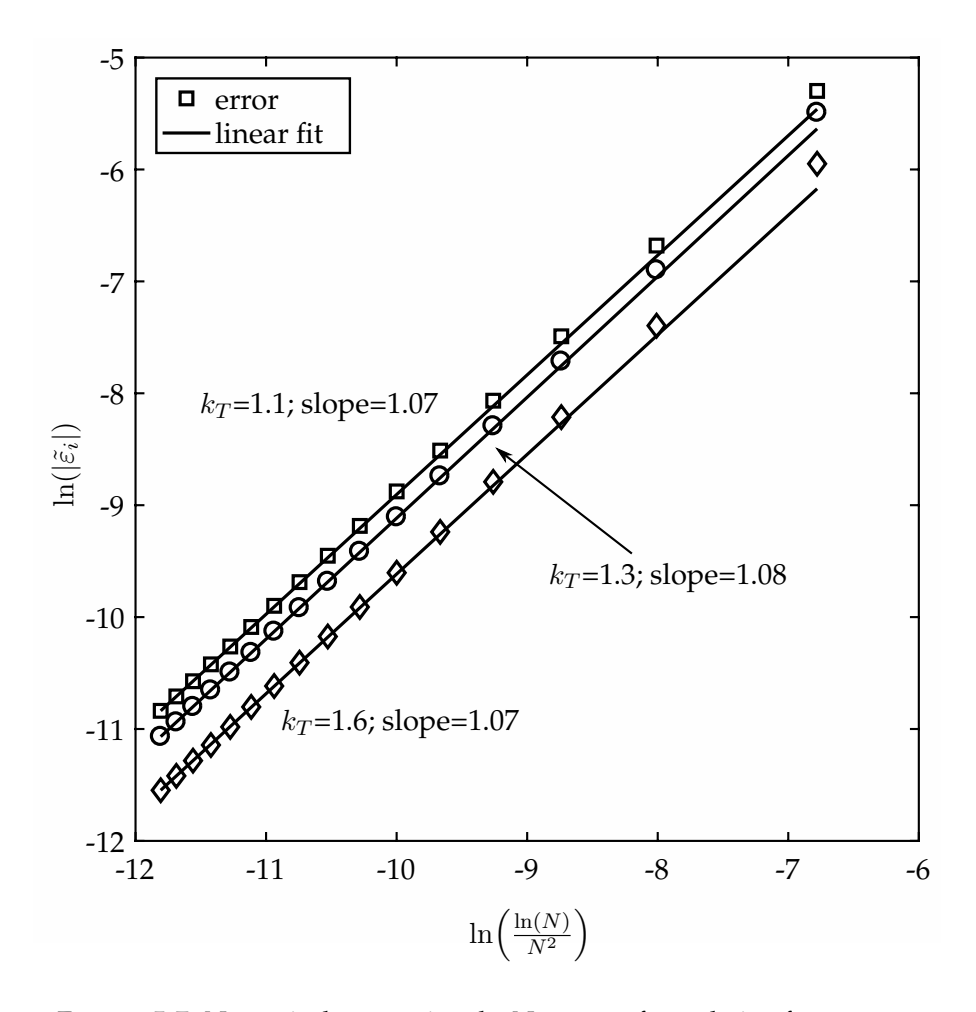


FIGURE 5.7: Numerical error using the Neumann formulation for symmetric bodies with sharp corners for  $\alpha=2^{\rm o}$ .

The convergence of the error order to the theoretical estimations when using the Neumann formulation is much slower than when using the Dirichlet formulation for the same bodies under the same fluid configuration, i.e. the number of panels required for a good convergence is higher. The experiment with  $k_T=1.6$ 

in Figure 5.7 is executed again but with higher numbers of panels and the results are plotted in Figure 5.8. It is shown that the numerical error tends to the unity slope straight line with an increasing number of panels or decreasing panel longitude. The rest of figures in this chapter does not include this high number of panels for clarity, although the behaviour is similar than the one shown in Figure 5.8.

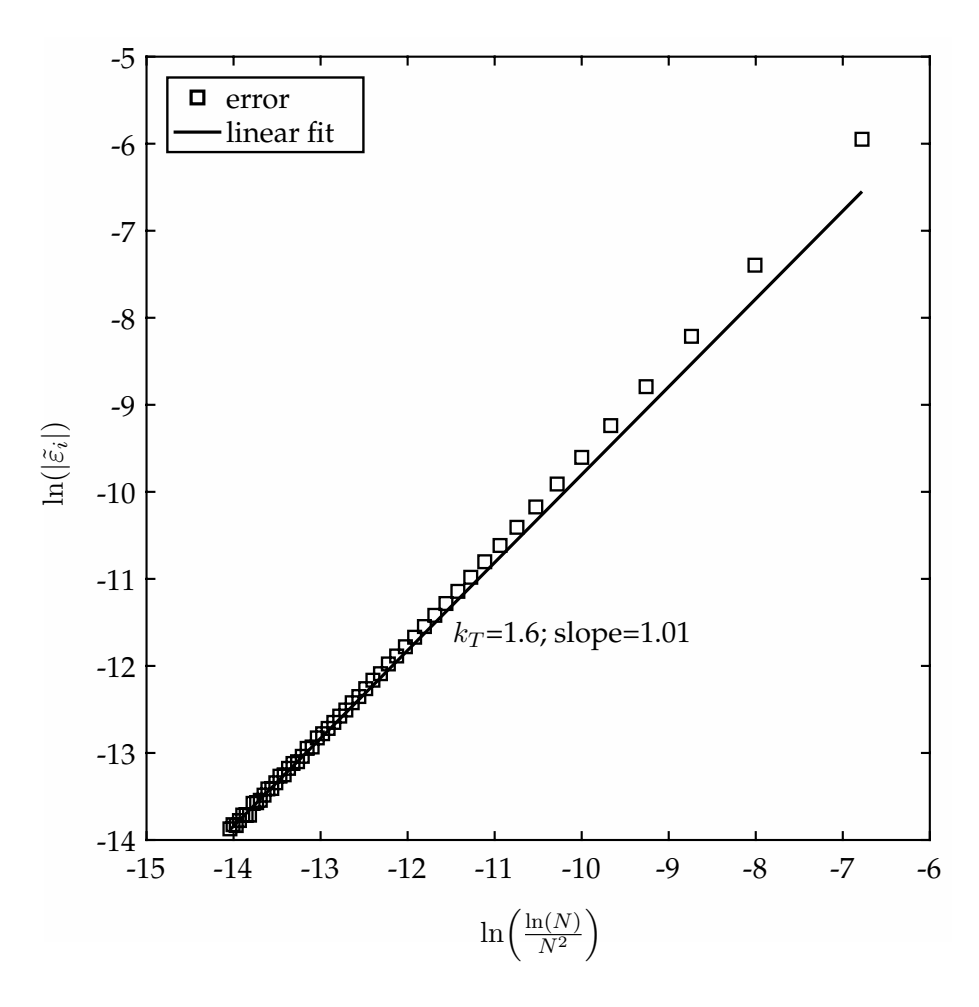


FIGURE 5.8: Numerical error using the Neumann formulation for symmetric body with sharp corners for  $\alpha = 2^{\circ}$  and a high number of panels.

For bodies of this type and as a difference with respect to Dirichlet formulation results, the order of the error does not show an important dependency on the angle of attack  $\alpha$ , as can be seen in the experiments presented in Figure 5.9 for  $\alpha=0^{\circ}$  and Figure 5.10  $\alpha=10^{\circ}$ . Green's equation is differentiated in order to apply the Neumann boundary conditions, which provides a system of N-1

equations in  $\varepsilon_i$  as shown in Eq. (5.29), that does not present a symmetry in  $\alpha$  that could benefit the cases when the angle of attack is null, as in the Dirichlet case. The matrix  $l\theta_{x_ix_j}^{\prime I}$  is not perfectly symmetric and the terms in the RHS of the system does not show up a symmetry with respect to  $\alpha$ .

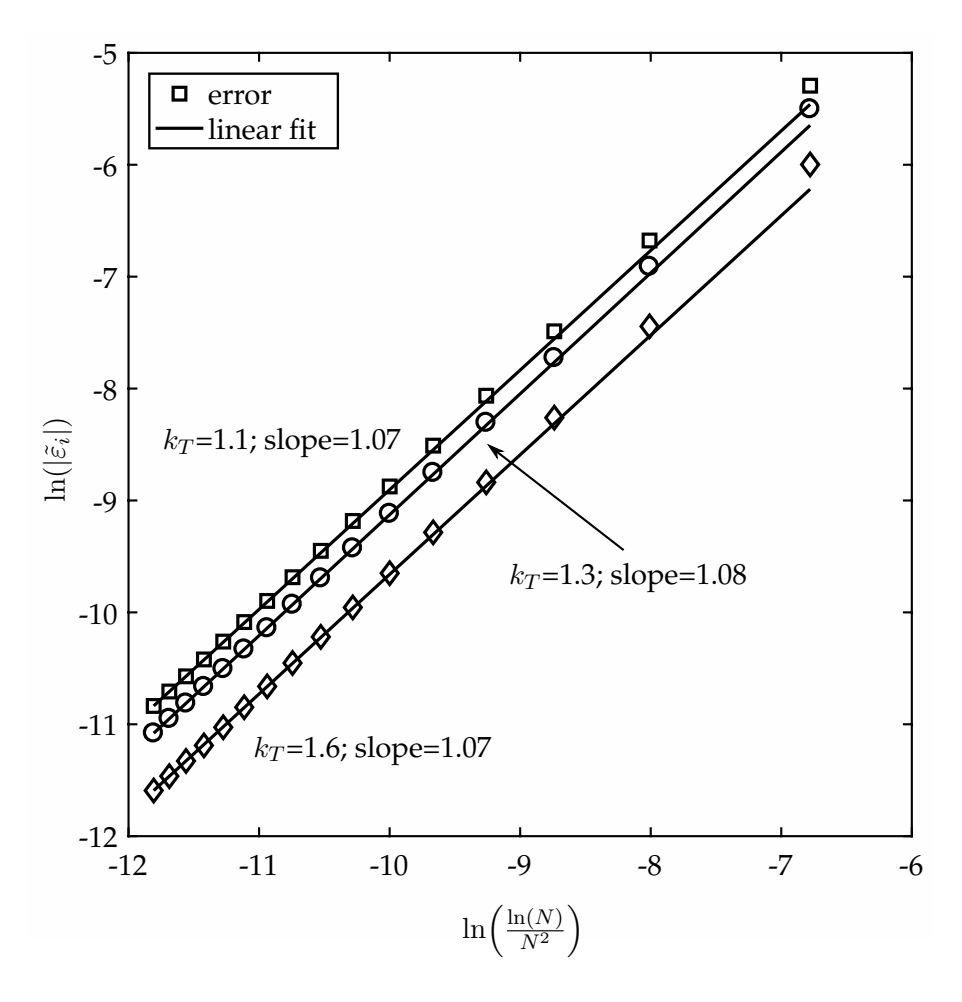


Figure 5.9: Numerical error using the Neumann formulation for symmetric bodies with sharp corners for  $\alpha=0^{\rm o}$ .

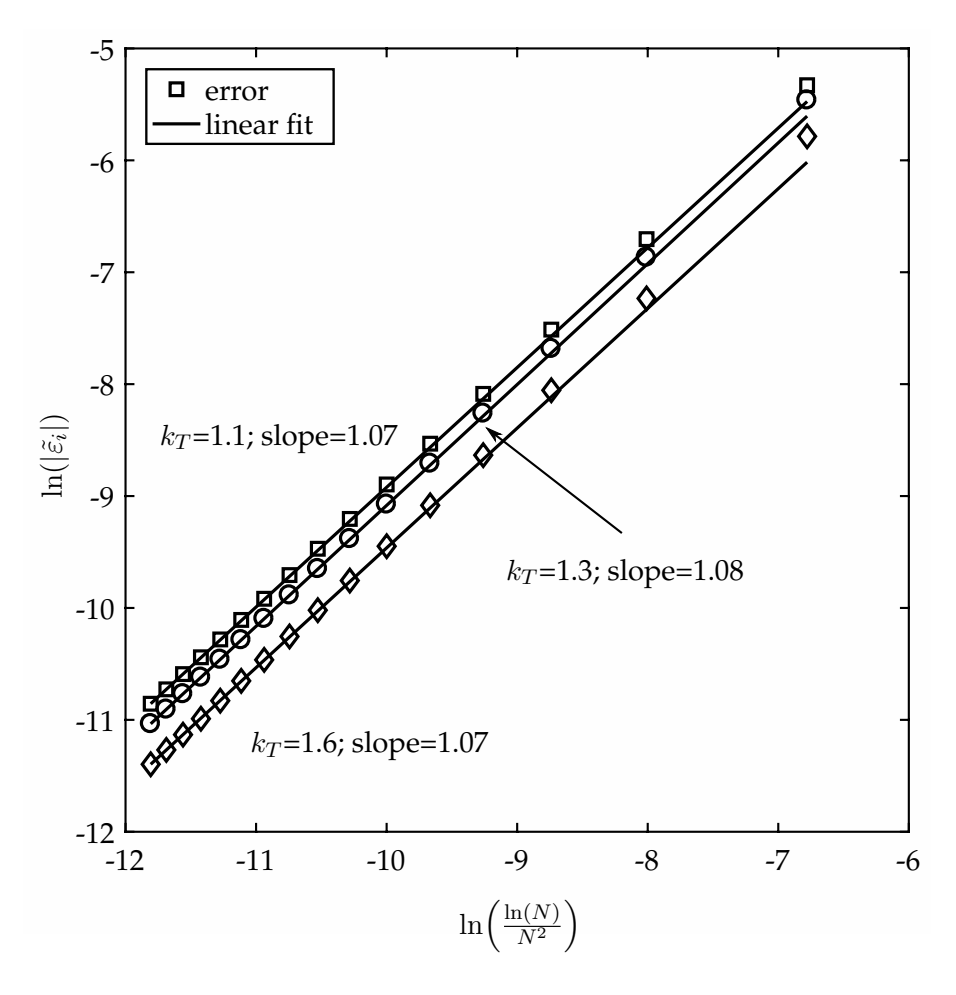


FIGURE 5.10: Numerical error using the Neumann formulation for symmetric bodies with sharp corners for  $\alpha=10^{\rm o}$ .

In case of bodies with a trailing edge that resembles a very sharp cusp, as in the body in Figure 5.11, the error order is different than  $O\left(\frac{1}{N^2}\ln(N)\right)$ . The obstacle in Figure 5.11 has been obtained from a Karman-Trefft transformation (see Eq. (4.60)) with  $k_T=1.9$  and with  $(x_0,y_0)=(-0.2,0)$  and R=1. Figure 5.12 shows for  $\alpha=2^{\rm o}$  a slope far away from the unity and for different  $\alpha$ , including  $\alpha=0^{\rm o}$ , the results are similar, which confirms the no dependence of the numerical error order with  $\alpha$ .

These very sharp trailing edges introduces terms that are of order O(1) far from the diagonal in the matrix  $l\theta_{x_ix_j}^{\prime I}$  of the system in Eq. (5.29). In particular the terms (i,j)=(2,N), (i,j)=(N,2) and the surrounding terms are of O(1) so the error order estimations provided in previous sections stops to be valid.

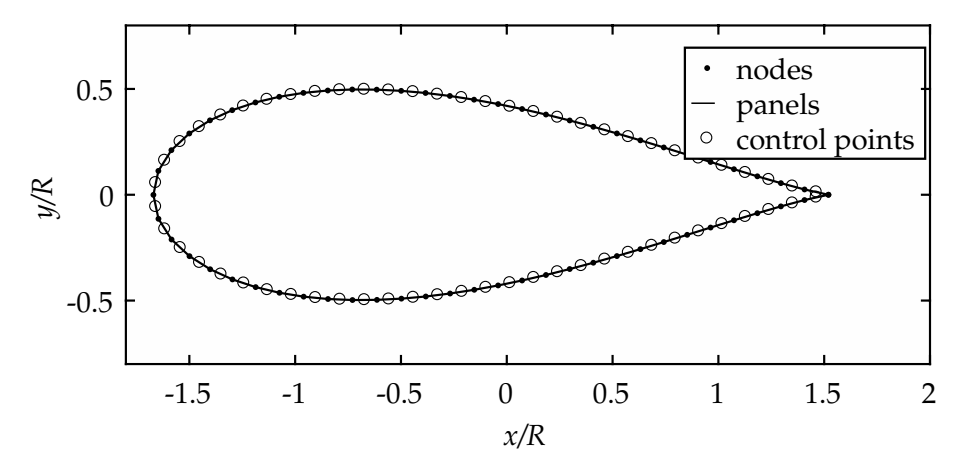


FIGURE 5.11: Symmetric body with a sharp corner obtained from a Karman-Trefft transformation with  $k_T=1.9$ .

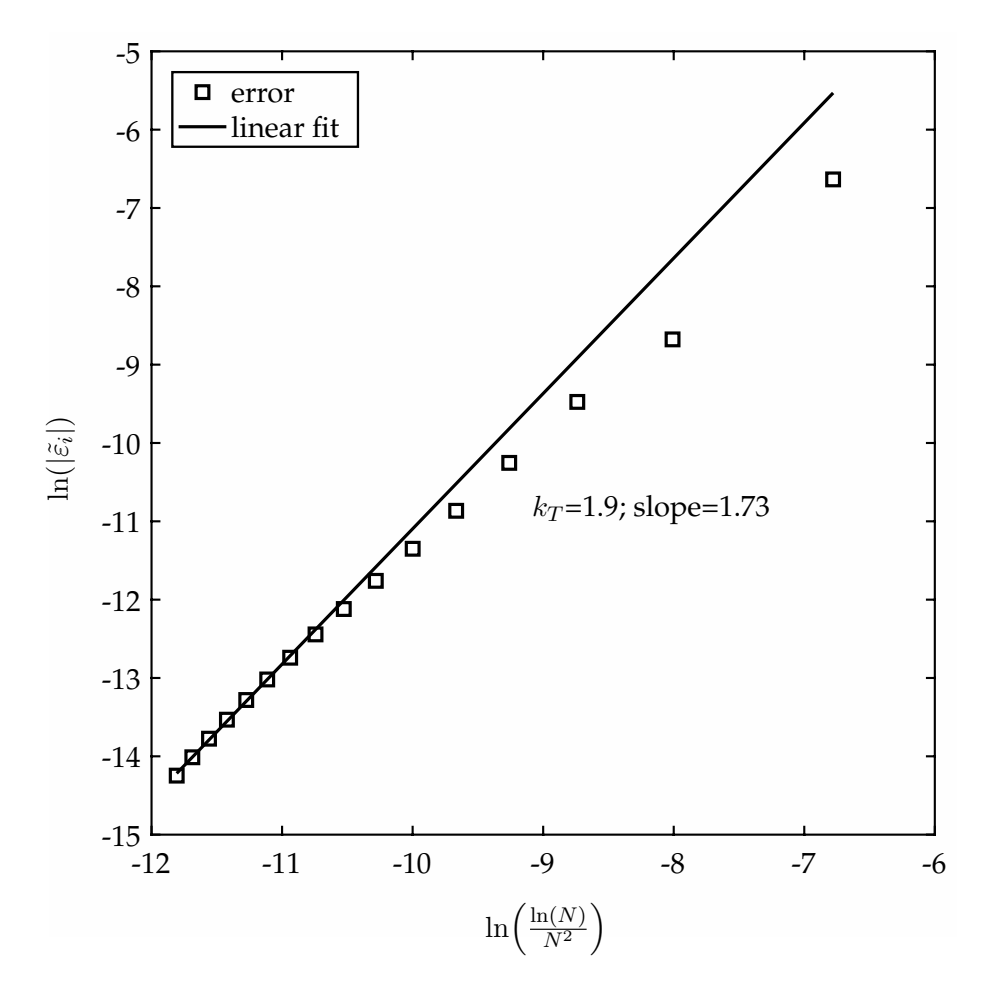


Figure 5.12: Numerical error using the Neumann formulation for symmetric bodies with very sharp corners for  $\alpha=2^{\rm o}$ .

### 5.3.3.2 Asymmetric bodies with sharp corners

For asymmetric bodies with sharp corners the results are similar to those obtained for symmetric bodies. Figure 5.13 shows asymmetric bodies obtained from a Karman-Trefft transformation with different values of  $k_T$ ,  $(x_0, y_0) = (-0.2, 0.3)$  and R = 1, while Figure 5.14 shows the numerical error for  $\alpha = 2^{\circ}$ .

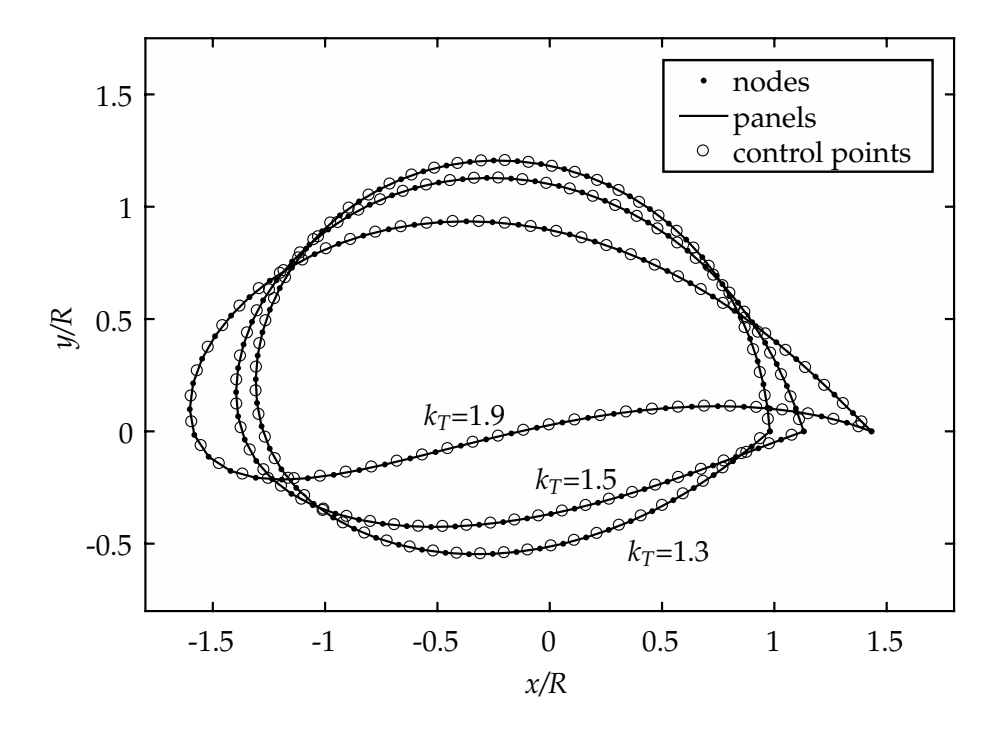


FIGURE 5.13: Asymmetric bodies with sharp corners obtained from a Karman-Trefft transformation with  $k_T = 1.3, 1.5$  and 1.9.

It can be derived from the figure, observing the results for  $k_T = 1.3$  and  $k_T = 1.5$ , that it is possible to solve the problem using the Neumann boundary conditions with the estimated order error even for asymmetric bodies. The results when using a different panel for the error calculation are of the same magnitude.

An exception to this last statement exists for asymmetric bodies, as well as for symmetric ones; when the trailing edge starts to be very sharp the error order does not follow a unity slope straight line. It can be observed for the body generated with  $k_T=1.9$  that the error order differs from the unity slope straight line, which is an expected result and in line with those reflected in Figure 5.12. It is

worth to mention here that the order error results when using a different panel for the error calculation are of the same magnitude, even though the results are not as uniform as with bodies without extremely sharp trailing edges; panels close to the trailing and leading edge behaves worst.

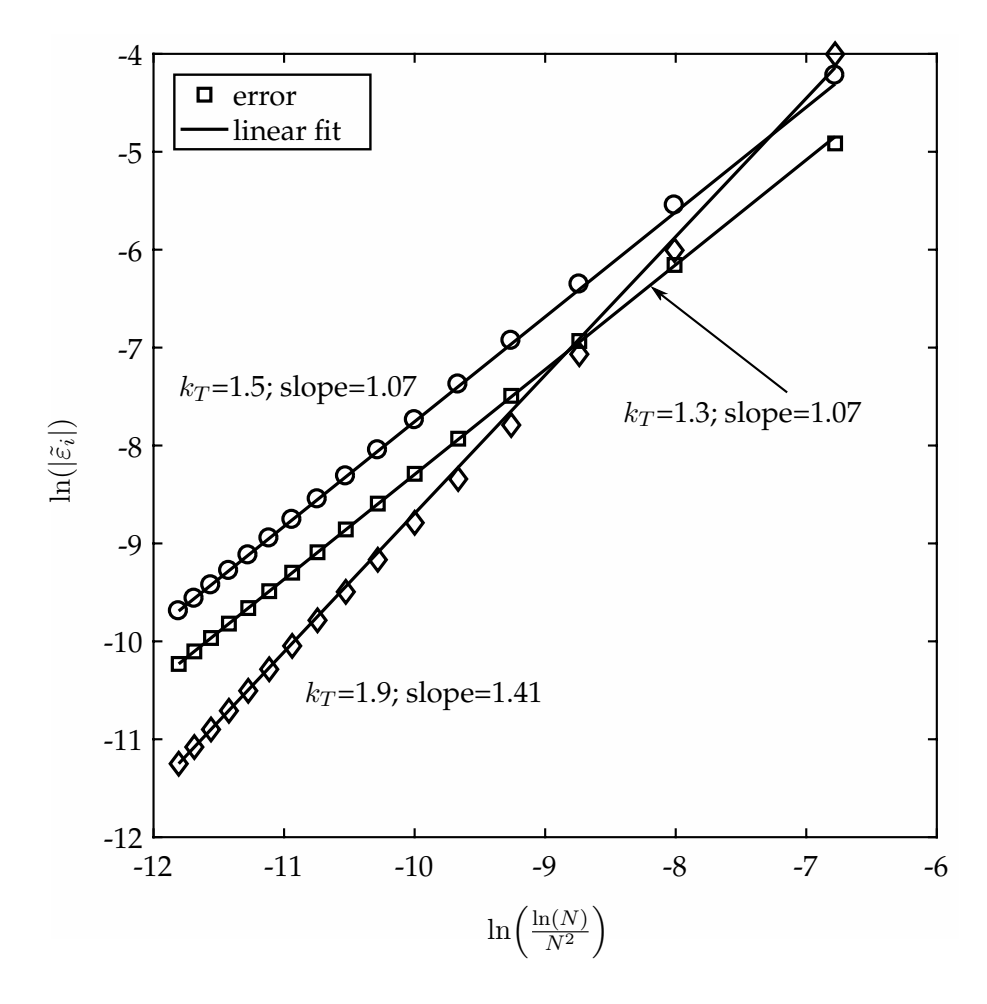


FIGURE 5.14: Numerical error using the Neumann formulation for asymmetric bodies with sharp corners for  $\alpha = 2^{\circ}$ .

The results obtained for  $\alpha=0^{\circ}$  and  $\alpha=10^{\circ}$  are presented in Figure 5.15 and Figure 5.16. Similar behaviour is obtained here by comparison with the symmetric bodies in the previous section; the error order results to be as estimated analytically for bodies generated with  $k_T$  not very close to 2.

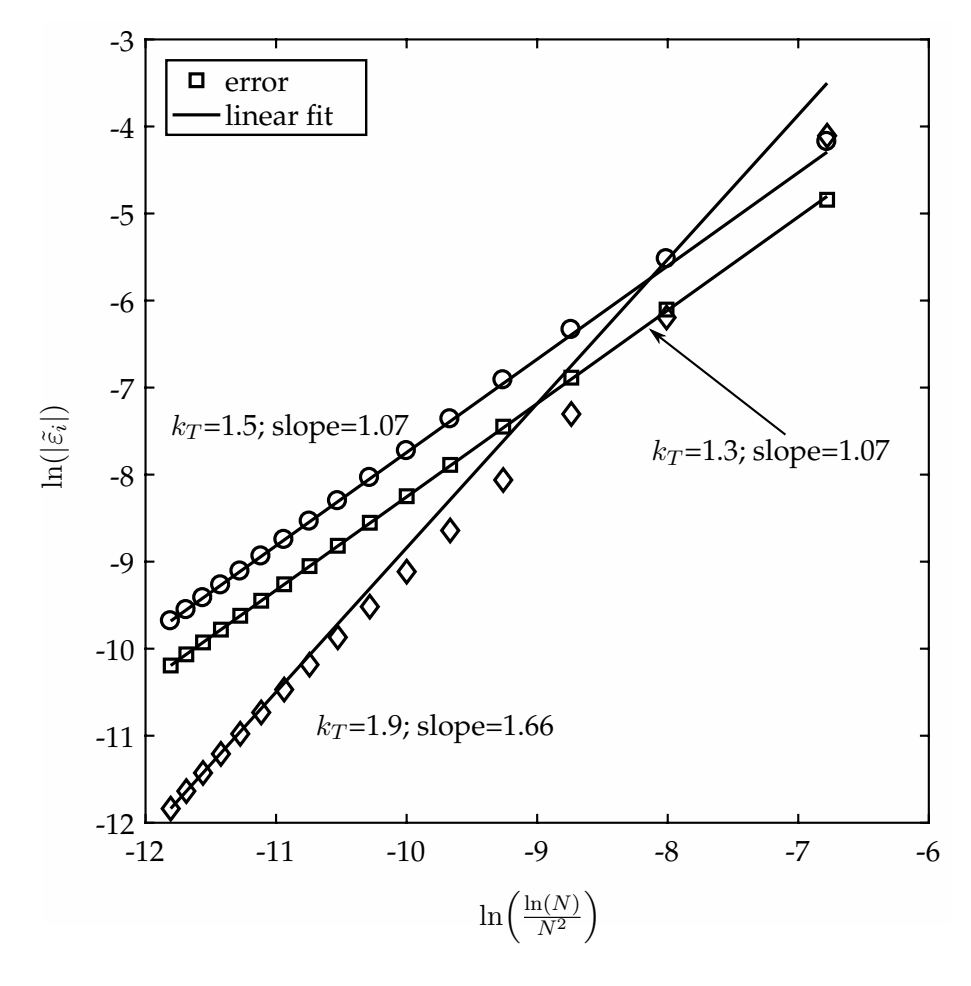


Figure 5.15: Numerical error using the Neumann formulation for asymmetric bodies with sharp corners for  $\alpha=0^{\rm o}$ .

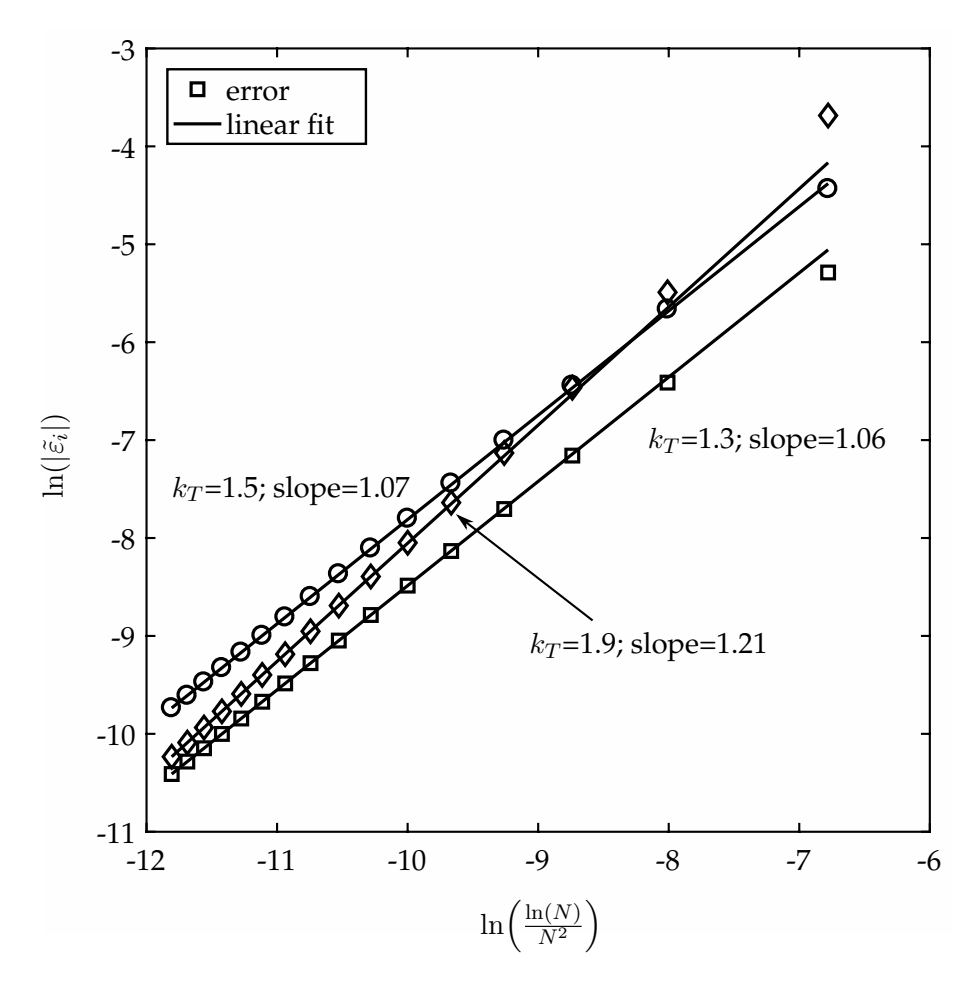


FIGURE 5.16: Numerical error using the Neumann formulation for asymmetric bodies with sharp corners for  $\alpha=10^{\rm o}$ .

A possible dependency with the angle of attack  $\alpha$  could be inferred for those body shapes with very sharp trailing edges. It can be observed by comparing the previous figures for an increasing  $\alpha$  (Figure 5.14, Figure 5.15 and Figure 5.16), that the error order slope decreases with an increasing alpha and tends towards the unity slope straight line. Figure 5.17 is included here to show the numerical results of an experiment with an extreme angle of attack  $\alpha=30^\circ$ ; they support the former statement. A deep study of these results is devoted for future works.

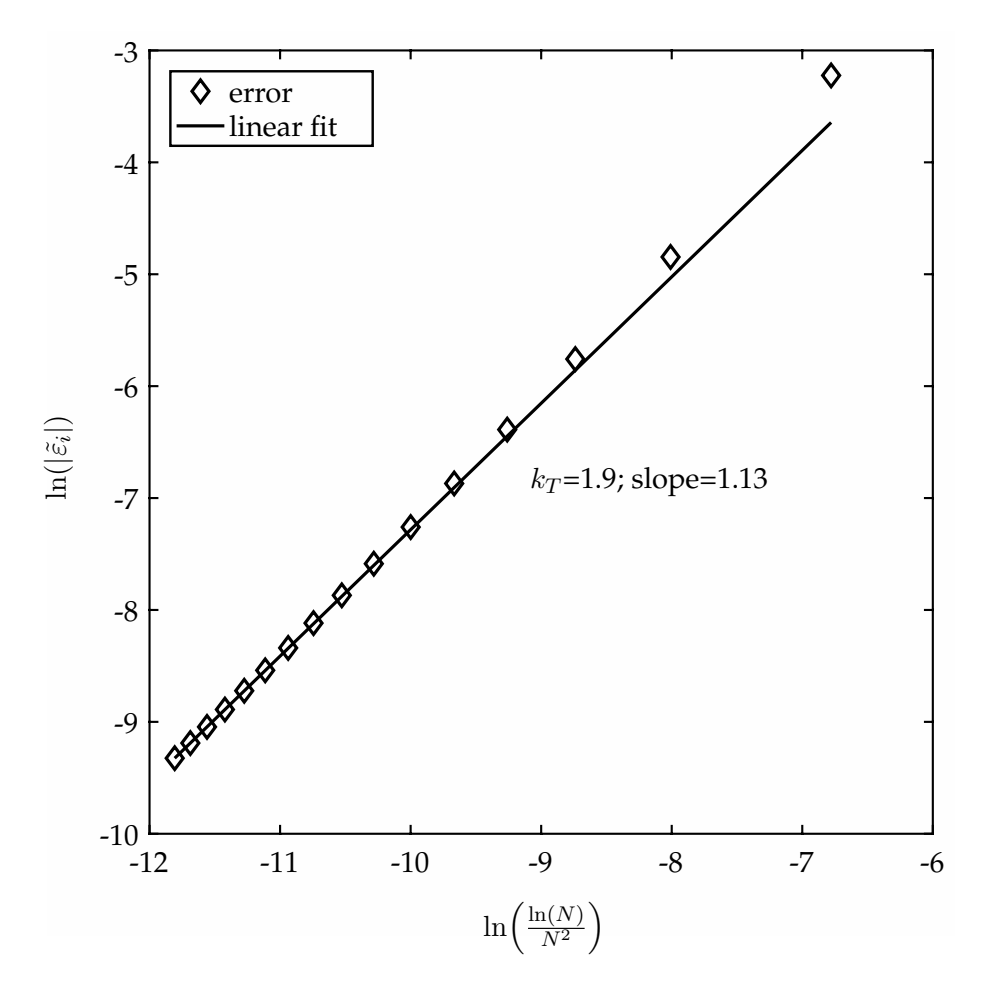


FIGURE 5.17: Numerical error using the Neumann formulation for an asymmetric bodies with a very sharp corner ( $k_T = 1.9$ ) and with a high angle of attack  $\alpha = 30^{\circ}$ .

## 5.4 Discussions

In this chapter a formal analytical and numerical analysis of the asymptotic global error in panel methods using Neumann formulation and using flat panels is presented for thick bodies with the possibility of convex and concave portions. The analysis shows that there are several factors affecting the order of the error.

(i) Regarding the geometry of the body, the main factor affecting the order of the error is the existence of extremely sharp corners. Unlike what happens when using the Dirichlet formulation, with the Neumann formulation, if there are sharp corners, the error is  $\varepsilon_i = O(l \ln(l))$  as predicted by the theory, even for flat panels and bodies with strong curvature, provided the length of

5.4. Discussions

the panels, which is O(1/N), is sufficiently small compared to the thickness of the body. Only when the body under study presents a very sharp trailing edge, then the order of the error is different to  $\varepsilon_i = O(l \ln(l))$ , and a possible dependency with the angle of attack could appear, although this study is left for future works.

- (ii) The order of the error does not show an important dependency on the angle of attack.
- (iii) To minimize error, the collocation points  $x_i$  should be located at the center of the panels  $\ell_i$ , and the points of comparison  $p_i$  should be located "directly above" the collocation points  $x_i$  in the convex case and coincident with  $x_i$  in the concave case. If this condition is violated the error is O(l/N).
- (iv There is no difference in the order of the error for bodies with only convex parts compared to bodies with both convex and concave parts.
- (v) Concerning the shape of the panels, the analysis shows that the use of curved panels rather than flat ones does not improve the order of the error.

## Chapter 6

## **Conclusions and Future Works**

The panel method or boundary element method (BEM) applied to solve the Laplace equation has been of great interest in the aerodynamics field for many years. The lack of a panel method to solve an obstacle configuration that exhibits both finite and zero thickness parts was the seed to begin working on this subject. We aim to participate with a small contribution to the completeness of the BEM subject.

The new formulation has been tested by comparison with analytical solutions for several configuration, each of them covering particular geometric aspects that are of interest for aerodynamics bodies. The results clearly show that this new method fits very well with the analytical solution and much better than the discrete vortex method, even for very thin airfoils and airfoils with cusped trailing edge. As the intuition already points out, there are three zones that may create some disturbances in the solution; the leading edge, the junction between the finite and zero thickness part of the body and the trailing edge. The pressure coefficients obtained for those points remark what the intuition anticipates, but with much better results than those obtained with the vortex method. Even with a very reduced number of panels the solution is very accurate. The convergence of this new formulation has also been tested, performing experiments with increasing number of panels. It is not even required to go to a high number of panels to obtain results that are one order of magnitude better than those obtained with

the discrete vortex method.

The method can be very useful for preliminary design in all kinds of problems that combine both finite-thickness and zero-thickness bodies; these include sailing boats, Gurney flap configurations, and the study of realistic aircraft aerodynamics. Preliminary studies for these type of obstacles may benefit from the fact that a discretization with a low number of panels and by using the current computer calculus capabilities, results can be obtained in a few seconds using this panel method.

The new panel method is making use of both Dirichlet and Neumann boundary conditions so in order to provide a closed and fully characterized BEM we have carried out a formal study to estimate the global error that each of these boundary condition have associated. The literature does not cover these estimations in a consistent or global way; this encouraged us to work on this topic. The analysis used in this thesis provides the order of the error for the velocity potential in Dirichlet conditions and velocity potentials differences for the Neumann one. The verification of this formal estimations have been done through the implementation of a numerical code in Matlab that enabled the comparison between numerical and analytical results. Even though this is not a newly implementation, a big effort has been applied to obtain a code that generates an extremely precise panelization; is not enough to have panels of comparable longitudes for several different bodies but to have panels of the same longitude or at least better than  $O(1/N^2)$ . Several body configurations experiment have been performed and demonstrates that the outputs fits very well with the error order estimations. The airfoils with very cusped trailing edges introduce modifications of the error order but this matches also with the theoretical analysis.

The new panel method for mixed configurations with finite thickness and zero thickness presented in this works and the comparison of the numerical results with the common discrete vortex method and with the analytical solution for several bodies configuration has been published in Ezquerro et al., 2014. The global error analysis of two-dimensional panel methods for Dirichlet formulation

6.1. Future Works

and the experiments carried out for its validity verification has been published in Ezquerro et al., 2017.

#### 6.1 Future Works

The formulation to solve mixed configurations with both finite-thickness and zero-thickness bodies is completed within this work. A big effort has been done in implementing a computer software that provides a discretization of such bodies, taking into account all the factors required for a good convergence and that solves the problem numerically as posed in Section 3.2. While the software discretization part actually accepts bodies obtained via analytical generation (Section 3.3), NACA airfoils plus a configurable tail and some handmade bodies, it still does not accept any kind of generic bodies. The numerical resolution part of the software already accepts any kind of discretization body as long as it is provided as defined in Fig. 3.1, even if the discretization does not follow all of the factor that affect the convergence, with a detriment in the precision. A possible future work could be to improve this software implementation and make it usable for any user and not only by this author.

The work presented here suggests several promising directions for future research, including application of this type of analysis to the study of error for panel methods using doublet distributions of variable strength along the panels, extension of the analysis to three-dimensional problems, and extension to other applications of BEM such as, for example, adaptive BEM computational schemes (see Zhang et al., 2006).

The global error analysis of two-dimensional panel methods for Neumann formulation and the experiments carried out for its validity verification are to be published as done for the Dirichlet case in Ezquerro et al., 2017.

The results obtained for the global error estimation for both Dirichlet and Neumann formulation indicate that the convergence of the error for bodies with sharp corners is highly influenced by the body shape itself. It might be possible by using this type of analysis to estimate a relationship between the shape of the sharp corner and the order of the error. In the Dirichlet case the studies were deep enough to estimate a  $O(1/N^p)$  with  $p \in [1,2]$ , and it might be possible to expand the work in order to link the value of p with the shape of the trailing edge. In the Neumann case a similar approach could be followed to try to locate such a kind of relationship.

Several lesson learnt have been collected during this thesis development on the importance of the quality of the discretization method. Contrary to what one might think it, the quality of the panel is as important as the number of them, if not more. This topic is not subjected to this thesis and has only been mentioned when extrictly required but could be one interesting field of study.

## Appendix A

## Dirichlet method integrals definition

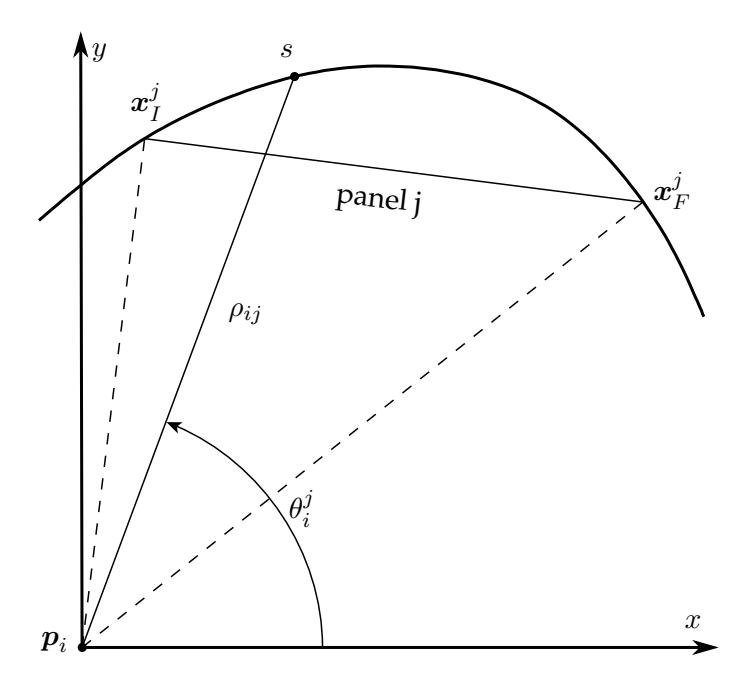
The integrals in Eq. (2.10) can be derived into a very simple equation. Writing the integral for a generic curve S, for a point p, with s as the variable of integration, using the axes definition in Fig. A.1 and the definition in Cartesian and in polar coordinates of  $s - p = (x, y) = \rho_{ij}(s)(cos(\theta_i^j(s)), sin(\theta_i^j(s)))$ , the following development can be done:

$$\int_{S} \frac{\boldsymbol{s} - \boldsymbol{p}}{|\boldsymbol{s} - \boldsymbol{p}|^{2}} \cdot \boldsymbol{n} ds = \int_{S} \frac{(x, y) \cdot (-dy, dx)}{x^{2} + y^{2}} = \int_{S} \frac{(-xdy + ydx)}{x^{2} + y^{2}} =$$

$$= \int_{S} \frac{\rho_{ij}^{2}(s)\theta_{i}^{\prime j}(s)cos^{2}(\theta_{i}^{j}(s)) + \rho_{ij}^{2}(s)\theta_{i}^{\prime j}(s)sin^{2}(\theta_{i}^{j}(s))}{\rho_{ij}^{2}(s)} ds =$$

$$= \int_{S} d\theta_{i}^{j}(s) = \theta_{iF}^{j} - \theta_{iI}^{j} \tag{A.1}$$

where the x axis has been selected to be parallel to the wake panel.  $\theta_i^j$  is the polar angle asociated to vector  $s - p_i$ . It is proved that the integral value does not depend on the shape of the curve s and instead, it only depends on the point p and on the initial and final points on the curve that serves as limits of integration.



 $\label{eq:Figure A.1: Discretization of geometry for the Laplace's equation integrals simplification.}$ 

## Appendix B

# Neumann method polar angle derivative definition

The polar angle  $\theta$  of the vector  ${\pmb y}-{\pmb x}$  for arbitrary points  ${\pmb x}=(x_1,x_2)$  and  ${\pmb y}=(y_1,y_2)$  is

$$\sin\theta = \frac{y_2 - y_1}{|\mathbf{x} - \mathbf{y}|}; \quad \cos\theta = \frac{x_2 - x_1}{|\mathbf{x} - \mathbf{y}|}.$$
 (B.1)

The configuration of these points, which should be imagined to be on the body surface or on the panels, is shown in Figure B.1.

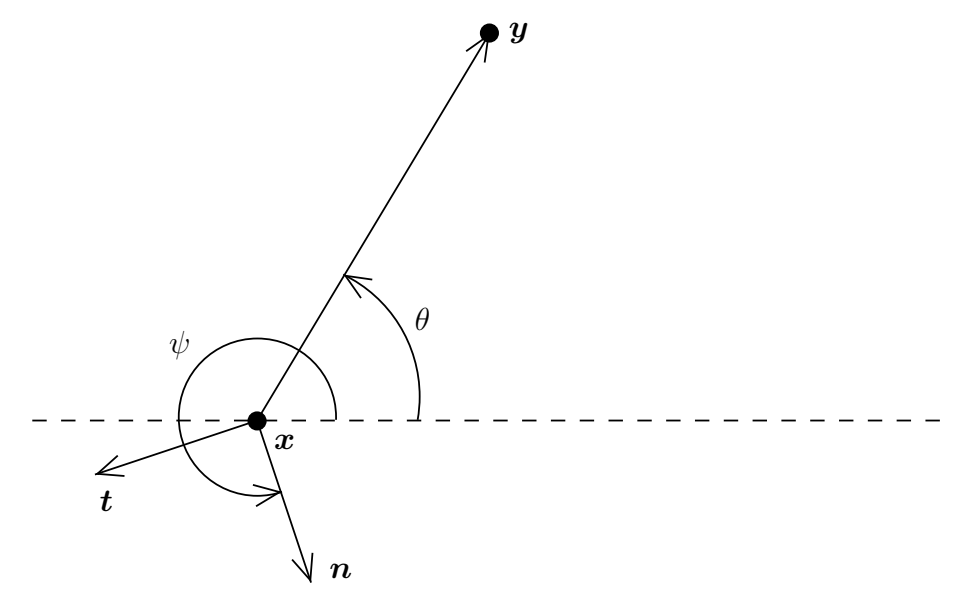


FIGURE B.1: Polar angle of the difference vector for two points x and y.

The gradient of this angle, with respect to the x coordinates, can be written as

$$\nabla_{x}\theta = \frac{1}{|x - y|^{2}}(y_{2} - x_{2}, x_{1} - y_{1}). \tag{B.2}$$

If we define the normal vector at x by  $n_x = (\cos \psi, \sin \psi)$  and the tangent vector by  $t_x = (\sin \psi, -\cos \psi)$  then we find that

$$\theta_x^{'y} = \theta_{xy}^{'} = \boldsymbol{n}_x \cdot \nabla_{\boldsymbol{x}} \theta = \frac{1}{|\boldsymbol{x} - \boldsymbol{y}|^2} [(y_2 - x_2) \cos \psi - (y_1 - x_1) \sin \psi] = \frac{(\boldsymbol{x} - \boldsymbol{y}) \cdot \boldsymbol{t}_x}{|\boldsymbol{x} - \boldsymbol{y}|^2},$$
(B.3)

where we have defined two different notations  $\theta_x^{'y}$  or  $\theta_{xy}^{'}$  for the same expression, so further developments are as readable as possible using one or the other notation.

## Appendix C

# Local geometric considerations for panels

Here we give the details behind some of the previous results.

It is useful to consider a system of local coordinates centered on a particular panel, as shown in Figure C.1. The origin is taken to be at the center of the panel  $\ell_i$  and the  $\xi_i$  and  $\eta_i$  axes are oriented parallel and perpendicular, respectively, to this panel. The

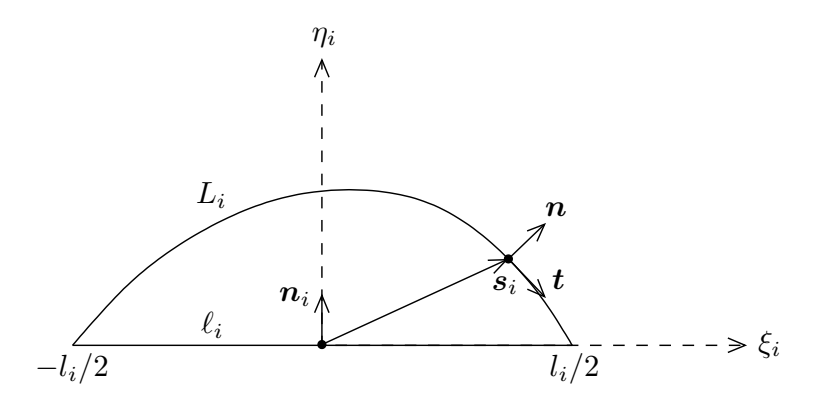


FIGURE C.1: Definition of local coordinate system.

body surface may be described in terms of these local coordinates by a function  $\eta_i = h(\xi_i), \xi_i \in [-l_i/2, l_i/2]$ . An arbitrary point  $s_i = (\xi_i, h(\xi_i))$  on this surface is associated with a unit vector  $\boldsymbol{n}$ , normal to the body surface at that point, and a tangential unit vector  $\boldsymbol{t}$ . Explicitly, these vectors are

$$n = \frac{(-h'(\xi_i), 1)}{\sqrt{1 + h'(\xi_i)^2}} = n_i + O(h'(\xi_i)),$$
(C.1)

$$t = \frac{(1, h'(\xi_i))}{\sqrt{1 + h'(\xi_i)^2}} = t_i + O(h'(\xi_i)), \tag{C.2}$$

where  $n_i = (0, 1)$  and  $t_i = (1, 0)$ 

The intermediate value theorem assures us that there exists a point  $x_0 = (\xi_0, \eta_0)$  on the surface  $L_i$  such that the tangent at  $x_0$  is parallel to the panel  $\ell_i$ , as shown in Figure C.2. Thus, we may express the curve as  $h(\xi_i) = h(\xi_0) - k(\xi_i - \xi_0)^2 + O(l^3)$ , with k a constant. Evaluating this expression at the endpoints  $h(\pm l_i/2) = 0$  immediately yields  $h(\xi_0) = O(l^2)$  while differentiation implies that  $h'(\xi_i) = -2k(\xi_i - \xi_0) = O(l)$ . Furthermore, one

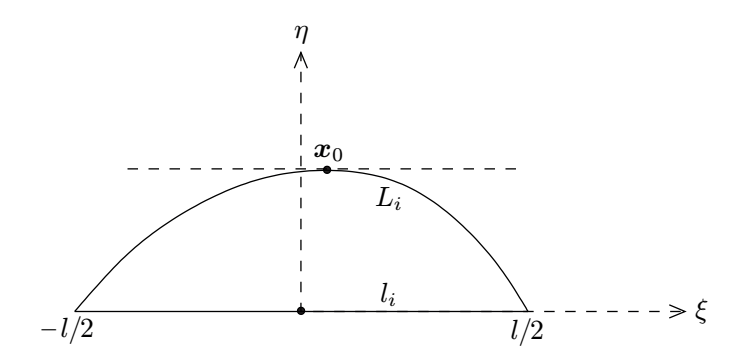


FIGURE C.2: Illustration of intermediate value theorem

can see that to differentiate with respect to  $\xi_i$  or with respect to  $s_i$  is equivalent up to  $O(l^2)$ ,

$$ds_i = \sqrt{1 + h'^2} d\xi_i = d\xi_i \left( 1 + O(h'^2) \right) = d\xi_i \left( 1 + O(l^2) \right), \tag{C.3}$$

The result used in Eq. (C.4) follows immediately from Eq. (C.1),

$$n = n_i + O(l). (C.4)$$

Another result, used first in the context of Eq. (4.19), follows immediately from the fact that  $h(\xi_i) = O(l^2)$  while the panel itself is O(l). As seen in Figure C.3, the angle

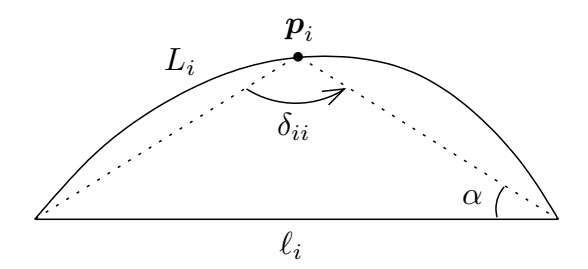


FIGURE C.3: Angle  $\delta_{ii}$  subtended at  $p_i$  by panel i itself, in the convex case.

subtended at the point  $p_i$  by panel i itself is  $\pi - \alpha - \beta$  in the convex case and  $\pi$  in the concave case (when  $p_i$  tends to the panel from outside). So, we can write

$$\delta_{ii} \simeq \pi - h(\mathbf{p}_i) \left( \frac{1}{l_{i\alpha}} + \frac{1}{l_{i\beta}} \right) = \pi + O(l).$$
 (C.5)

## **Bibliography**

- Bellamy-Knights, P.G. et al. (1989). "Convergence properties of panel methods". In: Computer Methods in Applied Mechanics and Engineering 76.2, pp. 171–178. ISSN: 00457825. DOI: 10.1016/0045-7825 (89) 90094-7. URL: http://linkinghub.elsevier.com/retrieve/pii/0045782589900947.
- Brebbia, C A and J Dominguez (1977). "Boundary element methods for potential problems". In: *Applied Mathematical Modelling* 1.7, pp. 372–378. ISSN: 0307-904X. DOI: 10. 1016/0307-904X(77)90046-4. URL: http://www.sciencedirect.com/science/article/pii/0307904X77900464.
- Brebbia, C. A., J. C. F. Telles, and L. C. Wrobel (1984). Boundary Element Techniques: Theory and Applications in Engineering. Berlin, Heidelberg: Springer Berlin Heidelberg. ISBN: 978-3-642-48862-7. DOI: 10.1007/978-3-642-48860-3. URL: http://link.springer.com/10.1007/978-3-642-48860-3.
- Ehlers, F. E. and P. E. Rubbert (1979). "A Mach Line Panel Method for Computing the Linearized Supersonic Flow". In: *NASA-CR-152126*.
- Ehlers, F Edward et al. (1979). "A Higher Order Panel Method for Linearized Supersonic Flow". In: CR 3062, NASA.
- Erickson, L (1990). "Panel Methods-An Introduction". In: TP 2995, NASA.
- Ezquerro, José M et al. (2014). "Panel method for mixed configurations with finite thickness and zero thickness". In: *Engineering Analysis with Boundary Elements* 44, pp. 28–35. ISSN: 09557997. DOI: 10.1016/j.enganabound.2014.04.011. URL: http://linkinghub.elsevier.com/retrieve/pii/S0955799714000885.
- Ezquerro, José M. et al. (2017). "Global error analysis of two-dimensional panel methods for dirichlet formulation". In: *Engineering Analysis with Boundary Elements* 74. June 2016, pp. 88–99. ISSN: 09557997. DOI: 10.1016/j.enganabound.2016.11.003. URL: http://linkinghub.elsevier.com/retrieve/pii/S0955799716304167.
- Falcão de Campos, J. A C, P. J A Ferreira de Sousa, and J. Bosschers (2006). "A verification study on low-order three-dimensional potential-based panel codes". In: *Computers and Fluids* 35.1, pp. 61–73. ISSN: 00457930. DOI: 10.1016/j.compfluid.2004.08.002.
- Hess, J. (1972). "Calculation of potential flow about arbitrary three-dimensional lifting bodies". In: *Douglas Aircraft Company* Douglas Report MDC-J5679-01.
- Hess, J L (1990). "Panel Methods in Computational Fluid Dynamics". In: Annual Review of Fluid Mechanics 22.1, pp. 255–274. ISSN: 0066-4189. DOI: 10.1146/annurev.fl. 22.010190.001351. URL: http://www.annualreviews.org/doi/10.1146/annurev.fl.22.010190.001351.
- Hess, J. L. and A. M. O. Smith (1962). "Calculation of Nonlifting Potential Flow About Arbitrary Three-Dimensional Bodies". In: *Douglas Aircraft Company* Douglas Report ES40622. ISSN: 03760421. DOI: 10.1016/0376-0421 (67) 90003-6.
- Hess, John L. (1973). "Higher order numerical solution of the integral equation for the two-dimensional neumann problem". In: Computer Methods in Applied Mechanics and

130 BIBLIOGRAPHY

- Engineering 2.1, pp. 1–15. ISSN: 00457825. DOI: 10.1016/0045-7825(73)90018-2. URL: http://linkinghub.elsevier.com/retrieve/pii/0045782573900182.
- Hess, John L. (1975). "Improved solution for potential flow about arbitrary axisymmetric bodies by the use of a higher-order surface source method". In: *Computer Methods in Applied Mechanics and Engineering* 5.3, pp. 297–308. ISSN: 00457825. DOI: 10.1016/0045-7825(75)90003-1.
- Hwang, W.S. (2000). "A boundary node method for airfoils based on the Dirichlet condition". In: *Computer Methods in Applied Mechanics and Engineering* 190.13, pp. 1679–1688. ISSN: 00457825. DOI: 10.1016/S0045-7825 (00) 00182-1.
- Johnson, F. T. and P. E. Rubbert (1975). *Advanced Panel-Type Influence Coefficient Methods Applied to Subsonic Flow*. Reston, Virigina: American Institute of Aeronautics and Astronautics. DOI: 10.2514/6.1975-50. URL: http://arc.aiaa.org/doi/10.2514/6.1975-50.
- Katz, Joseph and Allen Plotkin (2001). Low-Speed Aerodynamics, Second Edition. ISBN: 978-0-521-66552-0. DOI: 10.1115/1.1669432. URL: http://fluidsengineering.asmedigitalcollection.asme.org/article.aspx?articleid=1429947.
- Kinnas, Spyros A. and Ching Yeh Hsin (1994). "The local error of a low-order boundary element method at the trailing edge of a hydrofoil and its effect on the global solution". In: *Computers and Fluids* 23.1, pp. 63–75. ISSN: 00457930. DOI: 10.1016/0045–7930 (94) 90027–2.
- Mercer, J, J Weber, and E Ledferd (1974). "Aerodynamic influence coefficient method using singularity splines". In: *CR* 2423, *NASA* May 1974. ISSN: 05657059. DOI: doi: 10.2514/6.1973-123. URL: http://dx.doi.org/10.2514/6.1973-123.
- Morino, L, L T Chen, and E O Suciu (1975). "Steady and Oscillatory Subsonic and Supersonic Aerodynamics Around Complex Configurations". In: *Aiaa J.* 13.3, pp. 368–374. ISSN: 00011452. DOI: 10.2514/3.49706. URL: http://arc.aiaa.org/doi/abs/10.2514/3.49706.
- Morino, L and C Kuo (1974). "Subsonic potential aerodynamics for complex configurations: a general theory". In: *AIAA Journal* 12.2, pp. 191–197. ISSN: 0001-1452. DOI: 10.2514/3.49191. URL: http://arc.aiaa.org/doi/abs/10.2514/3.49191.
- Morishita, Etsuo (2004). "Schwartz-Christoffel Panel Method". In: *Transactions of the Japan Society for Aeronautical and Space Sciences* 47.156, pp. 153–157.
- Oskam, B. (1986). "Asymptotic convergence of higher-order accurate panel methods". In: Journal of Aircraft 23.2, pp. 126–130. ISSN: 0021-8669. DOI: 10.2514/3.45278. URL: http://arc.aiaa.org/doi/10.2514/3.45278http://doi.aiaa.org/10.2514/3.45278.
- Romate, J E (1988). "Local error analysis in 3-D panel methods". In: *Journal of Engineering Mathematics* 22.2, pp. 123–142. ISSN: 1573-2703. DOI: 10.1007/BF02383597. URL: http://dx.doi.org/10.1007/BF02383597.
- Rubbert, P E and G R Saaris (1968). "A General Three-Dimensional Potential-Flow Method Applied to V/STOL Aerodynamics". In: *SAE Technical Paper*. SAE International. DOI: 10.4271/680304. URL: http://dx.doi.org/10.4271/680304.
- Sanz-Andrés, A. et al. (2004). "Vehicle induced loads on pedestrian barriers". In: *Journal of Wind Engineering and Industrial Aerodynamics* 92.5, pp. 413–426. ISSN: 01676105. DOI: 10.1016/j.jweia.2003.12.004.
- Vaz, G B, L Eça, and J A C Falcâo de Campos (2003). "A numerical study on low and higher-order potential based BEM for 2D inviscid flows". In: Computational Mechanics 32.4-6, pp. 327–335. ISSN: 0178-7675. DOI: 10.1007/s00466-003-0490-8. URL: http://www.springerlink.com/openurl.asp?genre=article{\&}id=doi:10.1007/s00466-003-0490-8.

BIBLIOGRAPHY 131

Wilkinson, Stuart (1988). "Simple Multilayer Panel Method for Partially Separated Flows Around Two-Dimensional Masts and Sails". In: AIAA Journal 26.4, pp. 394–395. ISSN: 0001-1452. DOI: 10.2514/3.48766. URL: http://arc.aiaa.org/doi/10.2514/3.48766?journalCode=aiaaj.

- Ye, Wenjing and Yan Fei (2009). "On the convergence of the panel method for potential problems with non-smooth domains". In: *Engineering Analysis with Boundary Elements* 33.6, pp. 837–844. ISSN: 09557997. DOI: 10.1016/j.enganabound.2008.11.004.
- Yu, Wenjian, Zeyi Wang, and Xianlong Hong (2004). "Preconditioned multi-zone boundary element analysis for fast 3D electric simulation". In: *Engineering Analysis with Boundary Elements* 28.9, pp. 1035–1044. ISSN: 09557997. DOI: 10.1016/j.enganabound. 2004.02.006.
- Zhang, Wangyang et al. (2006). "Hierarchical H-Adaptive Computation of VLSI Interconnect Capacitance with QMM Acceleration". In: 8th International Conference on Solid-State and Integrated Circuit Technology Proceedings. IEEE, pp. 1438–1440. ISBN: 1-4244-0160-7. DOI: 10.1109/ICSICT.2006.306229. URL: http://ieeexplore.ieee.org/document/4098433/.